

Information scrambling and butterfly velocity in quantum spin glass chains

Venkata Lokesh K. Y¹, Surajit Bera² and Sumilan Banerjee²

¹*Centre of High Energy Physics, Indian Institute of Science, Bangalore 560012, India*

²*Centre for Condensed Matter Theory, Department of Physics, Indian Institute of Science, Bangalore 560012, India**

(Dated: October 8, 2024)

We make lattice generalization of two well-known zero-dimensional models of quantum spin glass, Sachdev-Ye (SY) and spherical quantum p -spin glass model, to one dimension for studying crossovers in non-local scrambling dynamics due to glass transition, complex dynamics, and quantum and thermal fluctuations in paramagnetic (PM) and spin glass (SG) phases. In the SY chain of quantum dots, each described by infinite-range random Heisenberg model of N spin- S $SU(M)$ spins, we obtain the quantum Lyapunov exponent λ_L and butterfly velocity v_B as a function of temperature T and the quantum parameter S across the PM-SG phase boundary using a bosonic spinon representation in the large N, M limit. In particular, we extract asymptotic T and S dependence, e.g., power laws, for λ_L and v_B in different regions deep inside the phases and near the replica symmetry breaking SG transition. We find the chaos to be non-maximal almost over the entire phase diagram. Very similar results for chaos indicators are found for the p -spin glass chain as a function of temperature and a suitable quantum parameter Γ , with some important qualitative differences. In particular, λ_L and v_B exhibit a maximum, coinciding with onset of complex glassy relaxation, above the glass transition as a function of T and Γ in the PM phase of the p -spin glass model. In contrast, the maximum is only observed as a function of S , but not with temperature, in the PM phase of SY model. The maximum originates from enhanced chaos due to maximal complexity in the glassy landscape. Thus, the results in the SY model indicate very different evolution of glassy complexity with quantum and thermal fluctuations.

1. INTRODUCTION

In a generic quantum many-body system, quantum information encoded in local degrees of freedom in the initial state *scrambles* to spread globally over the entire system due to its time evolution. The dynamics of quantum information, e.g., how rapidly local information scrambles, characterized by a rate or the quantum *Lyapunov exponent* λ_L , and how fast the information propagates from one spatial region to other, quantified by a speed or the *butterfly velocity* v_B , can provide crucial insights into the non-trivial dynamics of plethora of quantum many-body systems¹⁻⁴. These insights are complementary to that from transport and usual dynamical correlations. As a result, information scrambling has become an important theme of research for understanding holographic duality⁵, black hole information scrambling^{1,2}, non-Fermi liquids^{3,6-9} and quantum thermalization^{4,10,11}. For systems close to a semiclassical limit, information scrambling can often be connected to chaos¹²⁻¹⁶, namely extreme sensitivity of the classical trajectories to initial conditions.

For systems with many metastable configurations, information scrambling via quantum dynamics may become enhanced when the dynamics samples this multitude of configurations, leading to extreme sensitivity to initial conditions in the classical limit. Glasses¹⁷⁻¹⁹, which possess extensive number of metastable states¹⁸⁻²², are among the most prominent examples of such systems. At low temperature, the system remains trapped near one of the metastable configurations for a long time and explores the phase space extremely slowly. As a result, glasses exhibit many fas-

inating dynamical properties ranging from complex relaxation with anomalously large time scales^{17,23}, aging and memory effects²⁴, unusual transport properties such as the violation of Stokes-Einstein relations²⁵, dynamical heterogeneity^{19,26} etc. In particular, spin glasses^{23,27,28} with quenched randomness undergo ergodicity breaking thermodynamic phase transition at low temperature, e.g., for mean-field or infinite-range models, to replica symmetry broken^{29,30} spin glass phase. Recent work³¹ on a well-known solvable zero-dimensional or infinite-range model of quantum spin glass, namely the quantum p -spin glass model³²⁻³⁴, have shown that chaos, as characterized by the Lyapunov exponent λ_L , becomes stronger over a region above the glass transition where the dynamics exhibits typical signatures¹⁷ of complex glassy relaxation. In this region of enhanced chaos, the dynamics samples exponentially large number of saddle points of the classical potential energy landscape and becomes *maximally complex*^{35,36}, before eventually getting trapped within the basin of attraction of one of the glassy minima below the glass transition. In this work, we study scrambling dynamics in two solvable, albeit *spatially extended models*, of quantum spin glasses and show how the measures of information scrambling, v_B and λ_L , are influenced by glass transition, complex dynamics, and quantum and thermal fluctuations in various paramagnetic and spin glass phases.

In line with the growing interests^{31,35,37} in understanding the relation between scrambling and the complex dynamics of spin glass (SG) systems, we consider two well-known large N zero-dimensional ($0+1$ D) quantum spin glass models, namely (a) Sachdev-Ye (SY) model, a random Heisenberg spin glass³⁸⁻⁴⁰, and (b) quantum spherical p -spin glass model³²⁻³⁴, and make lattice gen-

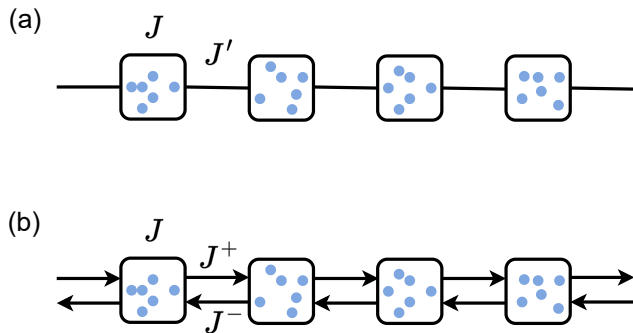


FIG. 1.1. An one-dimensional (1D) generalization of (a) SY model, (b) p -spin model for $p = 3$. Each lattice site contains a quantum dot described by zero-dimensional SY model in (a) and quantum spherical p -spin glass model in (b) with $N \gg 1$ spins (blue circles). In (a), the coupling between nearest neighbor sites are random two-spin interaction with one from each lattice site for the SY model. In the case of p -spin model in (b), the random nearest neighbor interaction is between two spins from one site and one from the other and vice versa.

eralizations of these models to one dimension (1 + 1 D), as shown schematically in Fig. 1.1. These generalizations allow us to meaningfully define a butterfly velocity v_B , along with λ_L , from an out-of-time-order correlation (OTOC) function^{3,41}. The SY model is parent to the celebrated fermionic Sachdev-Ye-Kitaev (SYK) model^{3,6,42}, which has emerged as a paradigm to study quantum many-body chaos, information scrambling^{8,9,41}, as well as strongly correlated metals⁴³. The SYK model is maximally chaotic, namely it saturates the remarkable upper bound^{2,3,6} $2\pi k_B T / \hbar$ for λ_L . There have been numerous lattice and higher dimensional generalizations^{41,43–50} of the zero-dimensional SYK model, with a view of studying transport and information propagation in extended interacting systems. Our lattice generalizations of the spin glass models pave the way to access non-local dynamical correlations and spatio-temporal information scrambling in spatially extended strongly disordered systems that undergo ergodicity-breaking glass transitions.

Earlier works on quantum chaos in spin glass systems^{31,35,37} have only looked at the Lyapunov exponent, e.g., its dependence on temperature T and quantum fluctuation parameter in the paramagnetic and spin glass phases, in the zero-dimensional quantum p -spin glass model, i.e., for a single p -spin glass quantum dot (see Fig. 1.1). On the other hand, studies on spatially extended large N systems, such as lattice generalizations of the SYK model^{41,43–50}, have been limited to non (replica) symmetry broken phases, such as Fermi and non-Fermi liquids metals. Our lattice generalizations of the spin glass models retain the same large N saddle points as the zero-dimensional models, and capture replica symmetry broken spin glass (SG) and unbroken paramagnetic (PM) phases, such as a spin liquid for SY quantum dot. Thus, the spatial locality in these extended models permits us to explore information scrambling across

replica-symmetry breaking spin glass phase transition. In particular, we obtain the variations of the Lyapunov exponent and butterfly velocity with thermal and quantum fluctuations across the PM-SG phase transition and various crossovers between dynamically different paramagnetic states, e.g., spin liquid and local moment states in the SY model. We also find the asymptotic dependence of λ_L and v_B on temperature T and quantum/classical parameter in different regions deep inside the phases as well as near the replica symmetry breaking SG transitions.

Temperature dependence of chaos indicators, especially that of the butterfly velocity, has been studied in several earlier works in various contexts, for example, for solvable large N models^{41,51–53}, perturbatively in interaction for weakly interacting systems⁵⁴ and in $1/N$ expansion in strongly interacting systems⁷, via numerical methods⁵³ as well as in the semiclassical limit of spin models^{55–57}. For a maximally chaotic [$\lambda_L = 2\pi T$ ($\hbar, k_B = 1$)] interacting diffusive metal built from SYK dots⁴¹, v_B has been found to follow a \sqrt{T} dependence. Also, in this case, the quantity, v_B^2/λ_L , which has the dimension of the diffusion constant, turns out to be exactly equal to energy diffusion constant, as expected from holographic theories⁵⁸. Similar relation, $D = v_B^2/4\lambda_L$ has been found to be satisfied for electron diffusion constant D in weakly interacting diffusive metal^{54,59}, where $\lambda_L \sim T^{d/2}$, $v_B \sim T^{d/4}$ in d dimension, and a temperature independent D is determined by elastic scattering. A power-law T dependence of v_B is similar to that at a critical point^{56,60}, i.e., $v_B \sim T^{1-1/z}$ for a dynamical exponent $z > 1$. In a strongly interacting system with critical Fermi surface of N -species fermions coupled with $U(1)$ gauge field, power-law behaviors, $\lambda_L \sim T$, $v_B \sim T^{1/3}$, with energy diffusion constant $\sim v_B^2/\lambda_L$, have been obtained⁷ at leading order in $1/N$ -expansion. The Lyapunov exponent and butterfly velocity also have been computed in (2+1 D) $O(N)$ non-linear sigma model, where, in the quantum critical region⁵², $\lambda_L \sim T/N$, and $v_B \sim c$, a constant close to the speed of light in the theory. Similar T independent v_B is found in the $O(N)$ -symmetry broken ordered phase⁵² with $\lambda_L \sim T^3$, whereas $\lambda_L \sim e^{-E_g/T}$, due to the gap E_g in the disordered phase for $T \ll E_g$, and v_B obeys a \sqrt{T} behavior^{52,53}. The latter is consistent with numerical calculations in 1D quantum Ising model⁵³. Power-law temperature dependence of λ_L and v_B is also observed^{55,56} in the ordered and disordered phases of spin models with semiclassical dynamics.

Our results for the dependence of λ_L and v_B on temperature T and the quantum/classical parameter S in the chain of SY quantum dots are summarized on the schematic phase diagram of Fig. 1.2. In this model, the dots are described by infinite-range random Heisenberg model of spin- S $SU(M)$ spins on N sites, where $N, M \rightarrow \infty$. Like in the lattice generalization⁴¹ of the SYK model, the SY chain model, in a bosonic spinon representation, is described by the same saddle point of the zero-dimensional quantum dots with the strength of

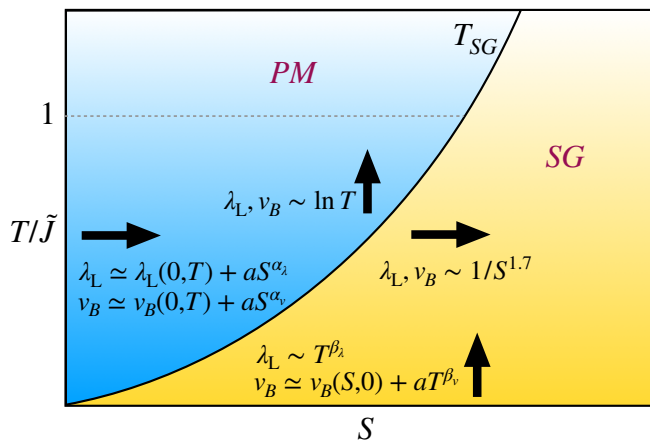


FIG. 1.2. **Schematic phase diagram for chaos in SY model.** Dependence of Lyapunov exponent λ_L and butterfly velocity v_B on temperature T and quantum parameter S are shown in the paramagnetic (PM) and spin glass (SG) phases. λ_L and v_B increase as a power law for small S in the PM phase, and as a power law in T for low temperature in the SG phase. Both the chaos indicators increase slowly, as $\sim \ln T$, above the glass transition T_{SG} , before saturating to a constant at high temperature. In the SG phase, both λ_L and v_B decrease as $\sim 1/S^2$. There is also maximum (not shown) in both λ_L and v_B as a function of S in the PM phase, at intermediate S , but there are no maxima as a function of T (see main text). The region bounded by $T_{SG}(S)$ and $T/\tilde{J} = 1$ (\tilde{J} coupling constant) line (dotted line) demarcates the quantum critical region within the PM phase. Arrows indicate the direction of the increase of the parameter.

the coupling J renormalized by the inter-dot interaction. As a result, λ_L , which is extracted from a local OTOC, has the same S and T dependence of a single dot, or the original SY model³⁸. On the contrary, the butterfly velocity can only be defined in a lattice model like the SY chain of Fig. 1.1(a). To compare with the chaotic properties of the SY chain, we also calculate the butterfly velocity from the non-local OTOC as a function of T and quantum parameter Γ (defined later) in a similar lattice model [Fig. 1.1(b)] of quantum spherical p -spin spin glass model³²⁻³⁴, as summarized in Fig. 1.3 (schematic). Again, $\lambda_L(\Gamma, T)$ of the p -spin glass chain is identical to that of the corresponding zero-dimensional model, and was studied in Ref. 31.

Our results are summarized below.

(1) As shown in Fig. 1.2, we find a power-law increase with S in the SY model, i.e., $\lambda_L(S, T) \simeq \lambda_L(0, T) + aS^{\alpha_\lambda}$ and $v_B(S, T) \simeq v_B(0, T) + aS^{\alpha_v}$ for small S in the PM phase with $\alpha_{\lambda(v)} \approx 0.5$ at a fixed temperature, e.g., in the quantum critical region for $T < \tilde{J}$. In this region, two types of PM behaviors, spin liquid and local moment, compete. In contrast to the power-law or gap-like temperature dependence seen in the disordered phase of many other models^{52,53,55,56}, a $\ln T$ variation of both λ_L and v_B are seen in the PM phase of the SY model close to the transition temperature T_{SG} . Similar $\ln T$ depen-

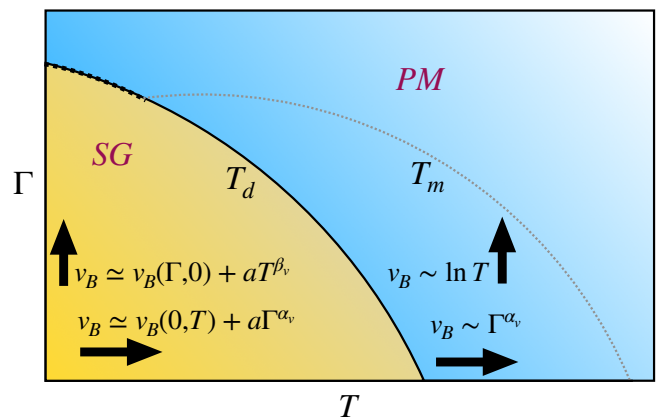


FIG. 1.3. **Schematic phase diagram for chaos in p -spin glass model.** Dependence of v_B on temperature T and quantum parameter Γ are shown in the PM and SG phases. Similar dependence has been seen for λ_L in Ref. 31. The continuous PM-SG phase transition $T_d(\Gamma)$ [or $T_{SG}(\Gamma)$] (solid line) terminates at a tricritical point and thereafter the transition is first order (hatched line). There is a maximum in v_B at $T_m(\Gamma)$ (dotted line), both as a function of T and Γ . v_B increases as power law with T and Γ at low temperature and small Γ , respectively, in the SG phase. The butterfly velocity increases as $\sim \ln T$ and as a power law in Γ above the glass transition in the PM phase, before the maximum. Arrows indicate the direction of the increase of the parameter.

dence is seen for the PM phase of the p -spin glass model, where $v_B \sim \Gamma^{\alpha_v}$ with $\alpha_v \approx 1.5$ [Fig. 1.3].

(2) On the contrary, in the SG phase of SY model, power-law temperature dependence, $\lambda_L(S, T) \sim T^{\beta_\lambda}$, and a power-law increment, $v_B(S, T) \simeq v_B(S, 0) + aT^{\beta_v}$, with $\beta_\lambda \approx 1 - 1.5$ and $\beta_v \approx 1.7$, are observed. $\lambda_L(\Gamma, T)$ and $v_B(\Gamma, T)$ behave very similarly with temperature, in the SG phase of p -spin glass. In the SG phase of SY model at a fixed T , both the Lyapunov exponent and butterfly velocity exhibit similar trends with increasing S or decreasing quantum fluctuations; λ_S, v_B decrease as $\sim 1/S^2$. These behaviors are similar to the p -spin glass model where both λ_L ³¹ and v_B decrease with decreasing quantum fluctuation, e.g., $v_B(\Gamma, T) \simeq v_B(0, T) + a\Gamma^{\alpha_v}$ with $\alpha_v \approx 0.7$.

(3) We show that the Lyapunov exponent for the spin liquid solution for small S and low temperature extrapolates to a value much smaller than maximal $2\pi T$ for $S \rightarrow 0$, unlike in the SYK-type models⁸. This indicates large T and S dependent corrections to the expected asymptotic $S \rightarrow 0, T \rightarrow 0$ spin liquid solution.

(4) The Lyapunov exponent and butterfly velocity have smooth crossovers across the PM-SG transitions in both SY and p -spin glass models.

(5) As mentioned earlier, $\lambda_L(\Gamma, T)$ exhibits a maximum³¹ [$T_m(\Gamma)$ in Fig. 1.3] in the PM phase of the p -spin glass model as function of both Γ and T . The maximum corresponds to enhanced chaos due to the sampling of maximum complexity of the glassy landscape at T_m ^{35,36}.

The same maximum is found in v_B for p -spin glass. However, the maximum in λ_L and v_B is seen in the PM phase of the SY model only as a function of S , but not as a function of T . This implies a very different evolution of complexity with quantum and thermal fluctuations in the SY model, unlike that in the p -spin glass model.

(6) For computing the butterfly velocity, we implement a numerical approach alternative to the more standard semi-analytical *single-mode ansatz*^{51,61}. The results from the numerical method agree very well with those from the single-mode ansatz over the entire phase diagrams of SY and p -spin glass chains, thus, independently verifying the applicability of the single-mode ansatz even for the replica symmetry broken spin glass phase. Using the single-mode ansatz, we find that chaos is non-maximal almost over the entire phase diagram for SY and p -spin glass models.

We also connect our results for the chaos parameters with spectral characteristics of various regions of the phase diagram of the two models, like spin liquid, local moment, classical and quantum paramagnets, and spin glass. The dependence of λ_L and v_B on temperature and quantum parameters, like S and Γ in our case, can be used to characterize and classify phases of many-body systems as different chaotic fixed points⁸, in addition to usual characterizations of phases in terms of thermodynamic quantities and transport and other dynamical properties. The temperature dependence of these quantities deep inside a phase as well as close to a phase transition can diagnose the physical process that contributes to the relevant excitations of the system and relaxation mechanisms. In the same vein, the powerlaw temperature dependence of λ_L and v_B on temperature and quantum parameters can detect the processes contributing to chaos and, hence, thermalization. As a result, a large number of recent works^{3,6-8,37,41,50,52-57,62}, have studied temperature dependence of λ_L and v_B in various symmetry broken and unbroken phases and across phase transitions, as we have summarized earlier. The underlying mechanisms giving rise to the power-law temperature dependence in some of the cases, but not for all, are understood. For example, in a Fermi liquid $\lambda_L \sim T^2$ can be understood from the quasiparticle life time^{8,63}, whereas the maximal chaos in the SYK model leading to $\lambda_L = 2\pi T$ can be connected to the low-energy Schwarzian or *scramblon* mode^{3,6,9}. In our case, the power-law temperature dependence of λ_L and v_B in the spin glass phase at low temperature is due to the gapless nature of the marginal spin glass phase⁶². However, we do not have any clear understanding yet about the power-law dependence of λ_L and v_B on the quantum parameter S (Γ). Moreover, as discussed earlier, the exponents for the T dependence of λ_L and v_B in some cases can be interrelated via their relation with the diffusion constant $D \sim v_B^2/\lambda_L$, that connects chaos with transport. However, in this work, we have not computed the diffusion constant. Thus, we keep the study of the relations between various exponents for future works.

The rest of the paper is organized as follows. In Sec.

2, we discuss the one dimensional lattice generalizations of the zero-dimensional SY and quantum p -spin glass model. The large N saddle-point equations for the PM and SG phases for both the models are described in Sec. 3, followed by review of the phase diagrams known from earlier works. Sec. 4 describes the formalism for calculating local OTOC and the Lyapunov exponent using ladder approximation for the PM and SG phases for the SY model. This section reports the results for $\lambda_L(S, T)$ in the SY model and compares them with those in the p -spin glass model. The formalism for computing the butterfly velocity from non-local OTOC using two different methods, a numerical method and the semi-analytical single-mode ansatz⁶¹, is discussed in Sec. 5 for both SY and p -spin glass models. The results for v_B as a function of T and quantum parameter for the two models are described in this section. The appendices (Appendix A, Appendix B) give additional details of the derivations of the saddle-point equations and methods for their numerical self-consistent solutions. Appendix A 2 discusses the results for the spectral properties of the SY model. Appendix C provides details of the numerical computation of v_B .

2. LATTICE GENERALIZATIONS OF SOLVABLE QUANTUM SPIN GLASS MODELS

As mentioned earlier, we consider one-dimensional (1D) chains of zero-dimensional random quantum Heisenberg and spherical p -spin glass quantum dots, as shown in Fig. 1.1 and discussed below.

A. 1D chain of Sachdev-Ye (SY) spin-glass quantum dots

We make a lattice generalization of the well-known zero-dimensional SY model of random quantum Heisenberg model by arranging $x = 1, \dots, L$ quantum dots of SY model, where each dot contains $i = 1, \dots, N$ sites. The model is described by the Hamiltonian

$$\mathcal{H} = \frac{1}{2\sqrt{MN}} \sum_{x,i \neq j} J_{ij,x} S_{i\alpha\beta,x} S_{j\beta\alpha,x} + \frac{1}{\sqrt{MN}} \sum_{x,i,j} J'_{ij,x} S_{i\alpha\beta,x} S_{j\beta\alpha,x+1}. \quad (2.1)$$

Here the first term represents all-to-all infinite-range interactions within a dot, and the second term the nearest-neighbour inter-dot coupling. The couplings $J_{ij,x}$ and $J'_{ij,x}$ are drawn from Gaussian distribution, independently at each site with zero mean and variances,

$$\overline{J_{ij,x}^2} = J^2, \quad \overline{J'_{ij,x}{}^2} = J'^2. \quad (2.2)$$

$S_{i\alpha\beta,x}$ denote the spin degrees of freedom, the generators of the $SU(M)$ group for spin S , at each i and dot

x , where $\alpha, \beta = 1, \dots, M$. The model is exactly solvable in the large N limit ($N \rightarrow \infty$) followed by the large M limit ($M \rightarrow \infty$), i.e., thermodynamics, as well as equilibrium and non-equilibrium properties can be exactly obtained in this limit through large N saddle-point equations, as known from previous works^{38–40,64} on the zero-dimensional model. The effect of quantum fluctuations in the model can be tuned by varying the spin S and the classical and semiclassical regimes can be probed by taking the large S ($S \rightarrow \infty$) limit while appropriately scaling the energy/temperature scales⁴⁰. The $M = 2$ limit of the model is the usual $SU(2)$ Heisenberg model, which has been studied via quantum Monte Carlo (QMC)⁶⁵ after taking the $N \rightarrow \infty$ limit. The large M limit was found to capture the properties of the $SU(2)$ model quite well.

In Sec. 3A, we discuss the equilibrium phase diagram obtained from the large N saddle-point equations as a function of temperature T and spin S . The large N saddle point is obtained via the standard bosonic representation of the $SU(M)$ spin³⁸. Subsequently, our main results on the dynamical phase diagram for chaos, characterized via the Lyapunov exponent λ_L and butterfly velocity v_B , are discussed in Secs. 4 and 5.

B. 1D chain of spherical p -spin glass quantum dots

To compare and contrast the results for λ_L and v_B in the SY chain, we consider the lattice generalization of another paradigmatic model of quantum glasses, the quantum spherical p -spin glass model^{32–34,66}. The 1D chain of the p -spin glass quantum dots ($x = 1, \dots, L$) is described by the Hamiltonian

$$\begin{aligned} \mathcal{H} = & \sum_{x,i} \frac{\pi_{i,x}^2}{2\mathcal{M}} + \frac{1}{3!} \sum_{x,ijk} J_{ijk,x} s_{i,x} s_{j,x} s_{k,x} \\ & + \frac{1}{2!} \sum_{x,ijk} s_{i,x} (J_{ijk,x}^+ s_{j,x+1} s_{k,x+1} + J_{ijk,x}^- s_{j,x-1} s_{k,x-1}), \end{aligned} \quad (2.3)$$

for $p = 3$. The intra- and inter-dot all-to-all couplings among sites $i = 1, \dots, N$ in the dots, $J_{ijk,x}$ and $J_{ijk,x}^\pm$ are Gaussian random numbers with zero mean and variances,

$$\overline{J_{ijk,x}^2} = 3J^2/(2N^2), \quad \overline{J_{ijk,x}^{\pm 2}} = 3J'^2/(2N^2). \quad (2.4)$$

The commutation relation of the spin $s_{i,x}$ with the momentum $\pi_{j,x}$, $[s_{i,x}, \pi_{j,x'}] = i\hbar\delta_{ij}\delta_{xx'}$ induces the quantum dynamics. The spherical constraint $\sum_i s_{i,x}^2 = N$ makes the model nontrivial. Essentially, when the quantum dots are uncoupled ($J' = 0$), the Hamiltonian describes quantum particles with mass \mathcal{M} moving on the surface of an N -dimensional hypersphere. The inter-dot interaction couples particles in neighboring dots. The advantage of this model lies in the fact that one can take a classical limit of the model by continuously tuning a quantum fluctuation parameter $\Gamma = \hbar^2/\mathcal{M}J$ to zero^{31,37}.

The classical model for $\hbar \rightarrow 0$ limit (fixed \mathcal{M}) for a single dot gives rise to dynamics identical to the mode coupling theory (MCT) dynamics in the super-cooled liquid regime of structural glasses^{17,19,31,67,68}. The limit $\mathcal{M} \rightarrow \infty$ while keeping \hbar fixed leads to a different classical limit of infinitely heavy mass^{31,37}. In this work, we vary the dimensionless quantum parameter Γ .

In Sec. 3B, we discuss the equilibrium phase diagram of the model as a function of T and Γ . The results for λ_L and v_B are discussed in Secs. 4 and 5 and compared with those from the lattice SY model.

3. EQUILIBRIUM PHASE DIAGRAMS OF THE SPIN GLASS CHAINS

We first discuss the equilibrium phase diagram of the quantum spin glass chains [Eq.(2.1) and Eq.(2.3)] as a function of T and quantum fluctuation parameters, S or Γ [Figs. 3.1, 3.2]. The equilibrium phase diagrams are obtained by solving large N saddle-point equations. As we discuss below, due to the particular choice of inter-dot couplings in Eqs.(2.1),(2.3), the large N saddle-point equations of the lattice models are identical to the zero-dimensional saddle-point equations^{38,66} of the single dot with renormalized intra-dot coupling.

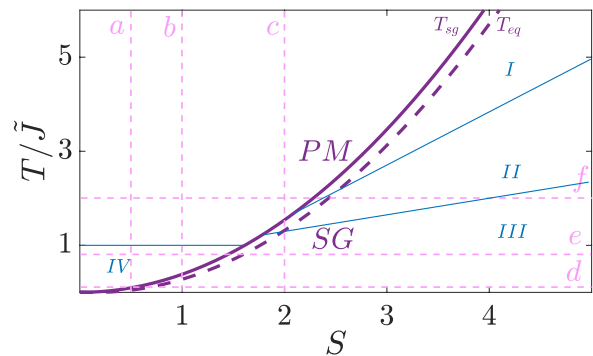


FIG. 3.1. Mean-field phase diagram of the bosonic spinon model⁴⁰ showing the paramagnetic and spin glass phases. Spin glass phase below T_{SG} (solid line) is determined by the *marginality* criterion (see main text). T_{eq} (thick dashed line) is determined by the equilibrium criterion. The regimes within spin glass phase separated by blue lines are identified via a large S expansion of saddle point equations⁴⁰ I, II and III are classical, semi-classical and quantum spin glass regimes respectively. IV is the quantum critical regime in PM phase. We perform the calculations of Lyapunov exponent and butterfly velocity across the SG-PM transition for several S as a function of T (along vertical dashed lines a , b , and c) and for several T as a function of S (along horizontal dashed lines d , e and f).

A. Sachdev-Ye chain

To capture both (replica) symmetry broken ordered SG and disordered paramagnetic (PM) phases we use bosonic spinons to represent spin- S $SU(M)$ generators as $S_{i\alpha\beta,x} = b_{i\alpha,x}^\dagger b_{i\beta,x} - S\delta_{\alpha\beta}$, where $b_{i\alpha,x}$, $b_{i\alpha,x}^\dagger$ ($\alpha = 1, \dots, M$) are bosonic annihilation and creation operators with the constraint $\sum_\alpha b_{i\alpha,x}^\dagger b_{i\alpha,x} = SM$ ($S > 0$) on the number of bosons at each i, x to fix the spin of the representation to S . The saddle-point equations, their solutions and resulting phase diagram for the bosonic representation have been discussed in detail for the zero-dimensional model in the pioneering works^{38–40}. We briefly discuss the derivation of saddle point equations for the SY chain model [Eq.(2.1)] in [Appendix A](#).

The disorder averaged Green's function $G_x^{ab}(\tau, \tau') = G^{ab}(\tau, \tau') = -\frac{1}{M} \sum_\alpha \langle \mathcal{T}_\tau b_{i\alpha,x}^a(\tau) \bar{b}_{i\alpha,x}^b(\tau') \rangle$ is independent of i, x and determines the equilibrium dynamics of the model. The Green's function is obtained from the saddle point equations in the limit $N \rightarrow \infty$ followed by $M \rightarrow \infty$ as

$$(G^{-1})^{ab}(i\omega_k) = (i\omega_k + \lambda) \delta_{ab} - \Sigma^{ab}(i\omega_k) \quad (3.1a)$$

$$\Sigma^{ab}(\tau) = \tilde{J}^2 [G^{ab}(\tau)]^2 G^{ba}(-\tau) \quad (3.1b)$$

where $\omega_k = 2\pi kT$ is bosonic Matsubara frequency with k an integer ($k_B = 1$), T the temperature in units of \tilde{J} . We have introduced the replicas $a = 1, \dots, n$ to carry out the disorder average. $G(i\omega_k) = \int_0^\beta d\tau e^{i\omega_k \tau} G(\tau)$ and β is the inverse temperature. Lagrange multiplier, λ is introduced to impose the constraint, $G^{aa}(\tau = 0^-) = -S$. The above saddle-point equations are same as the zero-dimensional ones^{38,39} with renormalized coupling,

$$\tilde{J}^2 = J^2 + 2J'^2 \quad (3.2)$$

due to the nearest-neighbor inter-dot coupling in Eq.(2.1). In the limit $n \rightarrow 0$, the replica structure of Green's function determines the PM and SG phases as we discuss below.

1. Paramagnetic phase

In the PM phase one employs a replica diagonal and symmetric ansatz, $G^{ab}(\tau) = G(\tau)\delta_{ab}$. Thus, the saddle-point equations reduce to,

$$[G(i\omega_k)]^{-1} = (i\omega_k + \lambda) - \Sigma(i\omega_k) \quad (3.3a)$$

$$\Sigma(\tau) = \tilde{J}^2 [G(\tau)]^2 G(-\tau) \quad (3.3b)$$

Analytic continuation from Matsubara to real frequency $i\omega_k \rightarrow \omega + i0^+$ gives the saddle point equation for retarded Green's function

$$[G_R(\omega)]^{-1} = \omega + \lambda - \Sigma_R(\omega) \quad (3.4)$$

where $\Sigma_R(\omega) = \Sigma(i\omega_k \rightarrow \omega + i0^+)$ and $\Sigma(i\omega_k) = \int_0^\beta d\tau e^{i\omega_k \tau} \Sigma(\tau)$. λ is determined by the constraint on

$G(\tau = 0^-)$. The procedure to numerically solve for the retarded Green's function is discussed in [Appendix A](#).

2. Spin glass phase

Following earlier works⁴⁰, we describe the spin glass phase via the following one-step replica symmetry breaking (1RSB) ansatz for the bosonic Green's function that appears in Eq.(3.1).

$$G^{ab}(\tau) = \tilde{G}(\tau)\delta_{ab} - g\epsilon_{ab} \quad (3.5)$$

or, $G^{ab}(i\omega_k) = \tilde{G}(i\omega_k)\delta_{ab} - \beta g\epsilon_{ab}\delta_{\omega_k,0}$, and

$$\Sigma^{ab}(\tau) = \tilde{\Sigma}(\tau)\delta_{ab} - \tilde{J}^2 g^3 \epsilon_{ab}, \quad (3.6)$$

where $\epsilon_{ab} = 1$ in the diagonal block of size $m \times m$, and 0 otherwise, for the $n \times n$ matrices. Here $\tilde{G}(\tau)$ is the regular part of the Green's function such that $\tilde{G}(\tau \rightarrow \infty) \rightarrow 0$ at $T = 0$. Working in the $n \rightarrow 0$ limit, the Edward-Anderson (EA) spin-glass order parameter is obtained from $q_{EA} = \lim_{\tau \rightarrow \infty} (1/M^2) \sum_{\alpha\beta} \langle S_{i\alpha\beta,x}(\tau) S_{i\beta\alpha,x}(0) \rangle = \lim_{\tau \rightarrow \infty} G^{aa}(\tau)G^{aa}(-\tau) = g^2$ at zero temperature. Using $[G^{-1}]^{ab}(i\omega_k) = A(i\omega_k)\delta_{ab} + B(i\omega_k)\epsilon_{ab}$ and the standard replica matrix inversion in $n \rightarrow 0$ limit, we get

$$A(i\omega_k) = \frac{1}{\tilde{G}(i\omega_k)}, \quad (3.7a)$$

$$B(i\omega_k) = \frac{\beta g}{[\tilde{G}(i\omega_k) - m\beta g]\tilde{G}(i\omega_k)}. \quad (3.7b)$$

The saddle point equation for \tilde{G} is therefore,

$$[\tilde{G}(i\omega_k)]^{-1} = i\omega_k - \frac{\tilde{J}g}{\Theta} - [\tilde{\Sigma}(i\omega_k) - \tilde{\Sigma}(i\omega_k = 0)] \quad (3.8a)$$

where

$$\begin{aligned} \tilde{\Sigma}(\tau) = \tilde{J}^2 & \left[\tilde{G}^2(\tau)\tilde{G}(-\tau) - 2g\tilde{G}(\tau)\tilde{G}(-\tau) - g\tilde{G}^2(\tau) \right. \\ & \left. + 2g^2\tilde{G}(\tau) + g^2\tilde{G}(-\tau) \right] \end{aligned} \quad (3.8b)$$

In the above, we have eliminated λ using the equation for $i\omega_k = 0$ and the parameterization $\tilde{G}(i\omega_k = 0) = -\Theta/\tilde{J}g$. The saddle point equation for g is obtained from Eq.(3.7b) as,

$$m\beta = \frac{1}{\tilde{J}g^2} \left(\frac{1}{\Theta} - \Theta \right) \quad (3.9)$$

The equations Eq. 3.8a, Eq. 3.8b and Eq. 3.9 along with the constraint, $\tilde{G}(\tau = 0^-) = g - S$ provide a closed set of self-consistent saddle-point equations for the SG phase. The characteristic of 1RSB solution is that the saddle point equations form a one-parameter family, parameterized here by Θ or equivalently by the breaking point m where $m \in (0, 1]$ in the $n \rightarrow 0$ limit. To

obtain this parameter we impose the usual marginality criterion⁴⁰, where we study the fluctuations of the free energy.

$$\mathbb{F}[G^{ab}, \lambda] = \frac{1}{\lambda} \sum_k \text{Tr} \ln [i\omega_k + \lambda - \Sigma^{ab}(i\omega_k)] \quad (3.10)$$

$$+ \frac{3\tilde{J}^2}{4} \sum_{ab} \int_0^\beta d\tau [G^{ab}(\tau)G^{ab}(-\tau)]^2 - \lambda S$$

in the replica space around the one-step solution and impose the condition that lowest eigenvalue of the fluctuation matrix in the replica space must vanish. The variations in free energy due to small variation g^{ab} in the saddle point Green's function G^{ab} for $a \neq b$, at second order, takes a generic form,

$$\delta\mathbb{F} = \sum_{a>b, c>d} M_{ab,cd} \delta g^{ab} \delta g^{cd} \quad (3.11)$$

Although, in principle one has to consider the variation in diagonal component, $\tilde{G}(\tau)$ and allow for the fluctuations due to the coupling between $\tilde{G}(\tau)$ and g^{ab} in the spin glass phase, it can be shown that these variations leave the eigenvalue e_1 intact⁴⁰. The diagonalization of the $n(n-1)/2 \times n(n-1)/2$ matrix M leads to the following three eigenvalues in the $n \rightarrow 0$ limit,

$$e_1 = 3\beta\tilde{J}^2 g^2 (1 - 3\Theta^2) \quad (3.12a)$$

$$e_2 = \frac{3\beta\tilde{J}^2 g^2}{\Theta^2} [\Theta^2 - 3 + 3\beta\tilde{J} g^2 \Theta (1 + \Theta)] \quad (3.12b)$$

$$e_3 = 6\beta\tilde{J}^2 g^2 (3\beta\tilde{J} g^2 \Theta - 1) \quad (3.12c)$$

Setting $e_1 = 0$ gives,

$$\Theta = \Theta_R = \frac{1}{\sqrt{3}} \quad (3.13)$$

Coincidentally, the marginality criterion leads to a gapless $\chi''(\omega) = (1/\pi)\text{Im} \chi(\omega) \propto \omega$ with a delta function peak at $\omega = 0$, where $\chi^{aa}(\tau) = G^{aa}(\tau)G^{aa}(-\tau) = (1/M^2) \sum_{\alpha\beta} \langle S_{i\alpha\beta, x}(\tau) S_{i\beta\alpha, x}(0) \rangle$ is the local spin susceptibility⁴⁰. This is unlike the equilibrium criterion, which minimizes free energy with respect to the breaking point m that leads to a gapped spectrum⁴⁰. In [Appendix A 2](#) we calculate $\chi''(\omega)$ and compare with the results from Ref. 69. Analytic continuation of Eq. (3.8a) gives the equation for retarded Green's function $G_R^{ab}(\omega) = G_R(\omega)\delta_{ab}$ with

$$[G_R(\omega)]^{-1} = \omega - \frac{\tilde{J}g}{\Theta_R} - [\Sigma_R(\omega) - \Sigma_R(\omega = 0)] \quad (3.14)$$

where $\Sigma_R(\omega) = \tilde{\Sigma}(i\omega_k \rightarrow \omega + i0^+)$ and $\tilde{\Sigma}(i\omega_k) = \int_0^\beta d\tau e^{i\omega_k \tau} \tilde{\Sigma}(\tau)$. λ is fixed by the constraint $\tilde{G}(\tau = 0^-) = g - S$, g is calculated from the relation Eq. 3.9. The procedure for numerically calculating the retarded Green's

function $G_R(\omega)$ is discussed in [Appendix A](#). For a fixed S , the temperature T_{SG} , below which the spins freeze into a SG order is identified by $m(T_{SG}) = 1$, where the SG order parameter q_{EA} jumps discontinuously to zero in the PM phase⁴⁰. A similar procedure is followed to obtain S_{SG} for a given temperature T . Unlike earlier works^{40,69}, in this work, we mostly use the real-frequency saddle-point solutions to find the Lagrange multiplier λ , EA order parameter q_{EA} in the SG phase, the PM-SG phase boundary, as well as the retarded Green's function $G_R(\omega)$, and chaos diagnostics λ_L and v_B . The numerical methods employed for obtaining the real-frequency saddle-point solutions are discussed in [Appendix A 1 a](#). The imaginary-time saddle-point equations are only used for deriving the real-frequency saddle-point equations via analytical continuation, and occasionally, to check the consistency of the thermodynamic quantities like λ , q_{EA} and $T_{SG}(S)$ computed from the real-frequency solution. For the sake of completeness, we discuss the numerical method used for the imaginary-time solution in [Appendix A 1 b](#). The same procedure is followed for the p -spin glass model.

3. Phase transition and crossovers

The equilibrium phase diagram of the SY chain model is identical to the zero-dimensional case, which has been studied in detail in the $N, M \rightarrow \infty$ limit in both bosonic and fermionic representation of the $SU(M)$ spins for general S ³⁸⁻⁴⁰. The phase diagram has been also studied for finite M in the $N \rightarrow \infty$ limit, using $1/M$ expansion⁷⁰ and for small S , e.g., $S = 1/2$, through QMC⁶⁵ in the $N \rightarrow \infty$ limit, as well as via exact diagonalization for finite N ⁷¹. In [Fig. 3.1](#), we reproduce the schematic large N, M phase diagram obtained via bosonic representation in Ref. 40. This is consistent with QMC result⁶⁵ for $S = 1/2$ for $N \rightarrow \infty$. The system undergoes a PM to SG phase transition at a temperature $T_{SG} \sim (2/3\sqrt{3})\tilde{J}S^2$, where the transition temperature, T_{SG}^{eq} obtained from the equilibrium criterion is slightly smaller than the temperature calculated via the marginal stability criterion. We refer to this latter temperature as T_{SG} . This corresponds to a dynamical transition, similar to that in the p -spin glass model^{33,66}, where the spin relaxation time diverges and glassy aging behavior commences in the non-equilibrium dynamics⁶⁴, approaching from the PM side.

The point $S = 0, T = 0$ corresponds to a quantum critical point with a spin liquid ground state, akin to SYK non-Fermi liquid^{3,6}. The spin liquid state exhibits so-called 'marginal spectrum'³⁸⁻⁴⁰, i.e., $\chi''(\omega) \sim \text{sgn}(\omega)$ at $T = 0$, or $\chi''(\omega, T) \sim \tanh(\omega/2T)$ at finite temperature, and diverging spin susceptibility $\chi(T) \sim \ln(T/\tilde{J})$, whereas the spectral density of the bosons $\rho(\omega) = -(1/\pi)\text{Im} G_R(\omega) \sim -\text{sgn}(\omega)/\sqrt{|\omega|}$ has a characteristic power-law divergence at $T = 0$. At any finite S the ground state is a spin glass and the spin liquid state becomes metastable up to a small maximum $S = S_{max} \simeq 0.052$ ⁴⁰ at $T = 0$. However, as shown in

Fig. 3.1, a quantum critical regime with marginal spectrum persists at finite temperature, $T_{SG} < T \lesssim \tilde{J}$, up to $S \lesssim 2$. Apart from the spin liquid, another paramagnetic solution to the Eqs.(3.3), the so-called ‘local moment’ solution⁴⁰ coexists in the phase diagram. This leads to a high-temperature ($T \gg \tilde{J}$) Curie susceptibility $\chi(T) \simeq S(S+1)/T$ which gradually decreases to $\chi(T) \simeq S^2/T$ as $T \rightarrow 0$, i.e., below T_{SG} , due to partial screening of the spins due to spin-spin interaction. Of course, for $T < T_{SG}$, the local moment solution is metastable. In appendix Appendix A 2, we discuss the numerically obtained bosonic spectral function $\rho(\omega)$ across the PM-SG transition as a function of S for fixed T , and as a function of T for fixed S , in the regime of interest for our chaos calculations (Appendix A 1 b and 5).

Based on the large S expansions in Ref. 40, the SG phase in Fig. 3.1 can be divided into three regimes – *I*. a classical regime for $\tilde{J}S \lesssim T \lesssim \tilde{J}S^2$ where all non-zero Matsubara frequency components of the Green’s function in eq.(3.1) can be neglected and spins become commuting vectors of length S , *II*. a semiclassical regime for $\tilde{J}\sqrt{S} \lesssim T \lesssim \tilde{J}S$, where $\rho(\omega) \sim \omega$ for $\omega \rightarrow 0$ is obtained by $1/S$ expansion of the saddle-point equations in the SG phase (Sec. 3 A 2) after scaling ω and T by $\tilde{J}S$, and *III*. a quantum regime for $0 \leq T \lesssim \tilde{J}\sqrt{S}$, deduced from the $1/S$ expansion of the internal energy and linear in T specific heat. In this work, we do not study the chaos across these various quantum-classical crossovers in detail. As shown in Fig. 3.1, we focus on changes in the chaotic properties, like λ_L and v_B , from different regions of the PM phase to the SG phase across the SG transition.

Here, we only study the chaos in the SY chain model [Eq.(2.1)] using bosonic representation. The model can also be studied in the large N, M limit via fermionic representation^{38,39,70}. In this case, the ground state is a spin liquid for all $0 \leq S \leq 1$ accessible in the fermionic representation. Thus system is maximally chaotic with $\lambda_L = 2\pi T$ ($\hbar = 1$) for $T \rightarrow 0$. However, for finite M the SG order can be recovered below $T_{SG} \sim \tilde{J} \exp(-\sqrt{M\pi})$ ^{40,70}. In the SG ground state at $T = 0$, one obtains the marginal spectrum $\chi''(\omega) \sim \text{sgn}(\omega)$ above a characteristic frequency $\omega^* = \tilde{J}q_{EA}$, i.e., over a range $\omega^* < |\omega| \ll \tilde{J}$, and the marginal SG behavior for $\chi''(\omega)$ for smaller frequencies $0 < |\omega| < \omega^*$. The EA order parameter in the fermionic case is $q_{EA} \sim 1/M$.

B. p -spin glass chain

As in the case of SY model, the equilibrium dynamics of the p -spin glass chain [Eq.(2.3)] is described by the disorder averaged Green’s function $Q_{ab}(\tau, \tau') = (1/N) \sum_i \langle \overline{\mathcal{T}_\tau s_{i,x}^a(\tau) s_{i,x}^b(\tau')} \rangle$. This model is solvable in the large N limit and is described by the Dyson equation,

tion,

$$(Q^{-1})^{ab}(i\omega_k) = (\omega_k^2/\Gamma + z) \delta_{ab} - \Sigma^{ab}(i\omega_k) \quad (3.15a)$$

$$\Sigma^{ab}(\tau) = \frac{3\tilde{J}^2}{2} [Q_{ab}(\tau)]^2, \quad (3.15b)$$

where the \tilde{J}^2 takes the same definition as in Eq.(3.2). The derivation of the above saddle-point equations, which are identical to that of the zero-dimensional p -spin glass model⁶⁶, is discussed in Appendix B. The spherical constraint $Q_{aa}(\tau = 0) = 1$ is imposed by the Lagrange multiplier z . Similar to the case of SY model, in the limit $n \rightarrow 0$, we have the replica diagonal PM and 1RSB SG phases. In the PM phase, the saddle point equations, after analytical continuation, simplify to

$$[Q_R(\omega)]^{-1} = -\omega^2/\Gamma + z - \Sigma_R(\omega), \quad (3.16a)$$

$$\Sigma_R(\omega) = \Sigma_R(i\omega_k \rightarrow \omega + i0^+) \quad (3.16b)$$

In the SG phase, we consider the 1RSB solution, which is exact⁶⁶. Using this ansatz, we can write the Dyson equation as,

$$Q^{ab}(\tau) = (q_d(\tau) - q_{EA})\delta_{ab} + q_{EA}\epsilon_{ab} \quad (3.17)$$

which after Fourier transformation becomes,

$$Q^{ab}(i\omega_k) = (q_d(i\omega_k) - \tilde{q}_{EA})\delta_{ab} + \tilde{q}_{EA}\epsilon_{ab}, \quad (3.18)$$

where $\tilde{q}_{EA} = \beta q_{EA} \delta_{\omega_k, 0}$. Further, it is convenient to write $q_d(\tau) = \tilde{Q}(\tau) + q_{EA}$, i.e., in terms of a regular part, such that $\tilde{Q}(\tau \rightarrow \infty) \rightarrow 0$ at $T = 0$, and EA order parameter q_{EA} . This can be inverted in the replica space as,

$$[Q^{-1}]^{ab}(i\omega_k) = A(i\omega_k)\delta_{ab} + B(i\omega_k)\epsilon_{ab} \quad (3.19)$$

with

$$A(i\omega_k) = \frac{1}{q_d(i\omega_k) - \tilde{q}_{EA}}, \quad (3.20a)$$

$$B(i\omega_k) = \frac{-\tilde{q}_{EA}}{q_d(i\omega_k)^2 + (m-2)\tilde{q}_{EA}q_d(i\omega_k) - (m-1)\tilde{q}_{EA}^2} \quad (3.20b)$$

where q_{EA} is Edward-Anderson order parameter and $\epsilon_{ab} = 1$ for the diagonal blocks and zero otherwise.

This leads to the saddle point equations,

$$\omega_k^2/\Gamma + z = \frac{1}{\tilde{Q}(i\omega_k)} + \tilde{\Sigma}(i\omega_k), \quad (3.21)$$

and

$$\frac{3(\beta m)^2}{2} q_{EA}^3 = \frac{x_p^2}{1+x_p}, \quad (3.22a)$$

$$y = \beta q_{EA}/q_d(0) \quad \text{and} \quad x_p = my/(1-y). \quad (3.22b)$$

where $\tilde{\Sigma}(i\omega_k) = \frac{3\tilde{J}^2}{2} \int_0^\beta d\tau e^{i\omega_k \tau} (q_d^2(\tau) - q_{EA}^2)$. The marginality criterion of setting the eigenvalue of the

transverse fluctuation matrix around the saddle point to zero leads to $x_p = p - 2^{66}$, which determines the breaking point m in the SG phase. The saddle-point equations along with the constraint $\tilde{Q}(\tau = 0) = 1 - q_{EA}$, can be analytically continued to real frequency and solved numerically. The details are discussed in the [Appendix B](#). We show the phase diagram determined by the solutions of the saddle point equation in [Fig. 3.2](#).

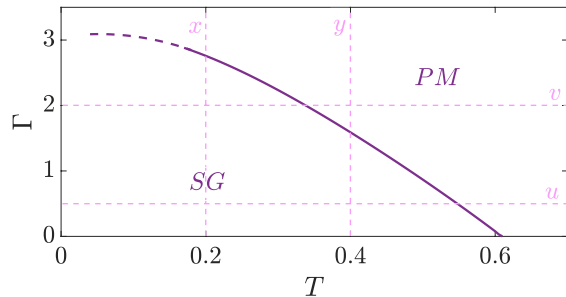


[FIG. 3.2](#). Mean-field phase diagram of quantum spherical p -spin glass model⁶⁶ as a function of temperature T and dimensionless quantum fluctuation parameter Γ (see main text). The solid line denotes second order phase transition between SG and PM phases. The second order line terminates at a tricritical point and the transition becomes first order for low temperature and larger Γ . Spin glass phase is determined by the marginality criterion. We calculate the Lyapunov exponent and butterfly velocity across the SG-PM transition for two values of T as a function of Γ (along vertical dashed lines x and y) and for two values of Γ as a function of T (along horizontal dashed lines u and v).

4. OUT-OF-TIME-ORDERED CORRELATOR (OTOC) AND LYAPUNOV EXPONENT

To characterize the many-body quantum chaos in the SY and p -pin glass chain models [Eqs.([2.1](#)),([2.3](#))], we first extract Lyapunov exponent from *on-site* OTOC. The calculation of Lyapunov exponent in the chain models is identical, with the effective coupling $\tilde{J} = \sqrt{J^2 + 2J'^2}$, to that in the corresponding zero-dimensional models, as has been done already for the p -spin glass in [Ref. 31](#). Thus, we focus on the effective zero-dimensional SY model, where the dot indices x in [Eq.\(2.1\)](#) drop out, and compare the results for $\lambda_L(T)$ across the SG transition with that in the zero-dimensional p -spin glass model³¹.

To diagnose the quantum chaos in the SY model, we consider two disorder-averaged four-point ‘regularized’ OTOCs^{3,6,12} for the bosonic operators on a Schwinger Keldysh (SK) contour [Fig. 4.1](#), with two forward and two backward branches, equally spaced in imaginary time

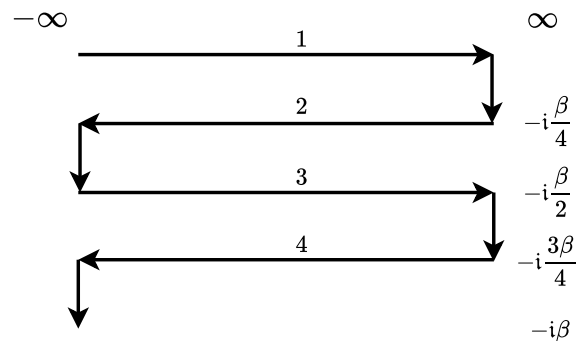


[FIG. 4.1](#). Schwinger-Keldysh contour with four real-time branches separated by $\beta/4$ in imaginary time, used for calculating OTOC.

with separation $\beta/4$, namely

$$F_1(t_1, t_2) = \frac{1}{N^2 M^2} \sum_{ij, \alpha\beta} \overline{\text{Tr}[y b_{i\alpha}^\dagger(t_1) y b_{j\beta}^\dagger(0) y b_{i\alpha}(t_2) y b_{j\beta}(0)]} \quad (4.1a)$$

$$F_2(t_1, t_2) = \frac{1}{N^2 M^2} \sum_{ij, \alpha\beta} \overline{\text{Tr}[y b_{i\alpha}(t_1) y b_{j\beta}^\dagger(0) y b_{i\alpha}^\dagger(t_2) y b_{j\beta}(0)]}, \quad (4.1b)$$

where $y^4 = \exp(-\beta\mathcal{H})/\text{Tr}[\exp(-\beta\mathcal{H})]$. In this work, we do not consider the OTOC of the physical spin operators $S_{i\alpha\beta x}$. Calculations of such an OTOC would involve 8-point bosonic correlation functions. We assume the maximum Lyapunov exponent in the large N, M SY model to be the same for OTOCs for bosonic and spin operators.

The calculation of the OTOCs in [Eq.\(4.1\)](#) on the SK contour ([Fig. 4.1](#)) can be done in the replica diagonal PM phase following a procedure very similar to SYK and related models^{2,3,8}. However below the dynamical transition temperature T_{SG} , in the SG phase, calculating any dynamic correlation function is more involved since the system always stays out of equilibrium^{64,72}. Alternatively, as discussed in [Ref. 31](#) for p -spin glass, the OTOCs can be calculated in the marginal SG phase by replicated generating function³¹ \mathcal{Z}^n on the four-branch contour [[Fig. 4.1](#)], i.e.,

$$\mathcal{Z}^n = \frac{1}{Z^n} \int \mathcal{D}(\bar{b}_{i\alpha}^a, b_{i\alpha}^a) \mathcal{D}\lambda_i^a \exp(iS) \quad (4.2)$$

where $a = 1, \dots, n$ are the replica indices and the action

$$iS = \left[i \int_{\mathcal{C}} dz \sum_{i\alpha a} \{ \bar{b}_{i\alpha}^a i \partial_z b_{i\alpha}^a - \lambda_i^a (\bar{b}_{i\alpha}^a(z) b_{i\alpha}^a(z) - SM) \} - \frac{1}{\sqrt{MN}} \frac{1}{2!} i \int_{\mathcal{C}} dz \sum_{ij, \alpha\beta, a} J_{ij} \bar{b}_{i\alpha}^a(z) b_{i\beta}^a(z) \bar{b}_{j\beta}^a(z) b_{j\alpha}^a(z) \right], \quad (4.3)$$

where z is the complex time variable along the SK contour \mathcal{C} [Fig. 4.1]. Here Z is the equilibrium partition function which appears due to the initial thermal density matrix³¹. The initial density matrix corresponds to the replica symmetric saddle point above T_{SG} , and 1RSB marginal SG saddle point below T_{SG} , as discussed in Sec. 3 A. After performing the disorder averaging, we can take the $n \rightarrow 0$ limit. The resulting time-translation invariant dynamical correlations and responses are identical to those obtained from the 1RSB saddle point solutions in the marginal SG phase. Using this replicated generating function, the OTOC can now be obtained as,

$$F_1^{aabb}(t_1, t_2) = \frac{1}{N^2 M^2} \sum_{ij, \alpha\beta} \langle yb_{i\alpha 4}^{\dagger a}(t_1) yb_{j\beta 3}^{\dagger a}(0) yb_{i\alpha 2}^b(t_2) yb_{j\beta 1}^b(0) \rangle \quad (4.4a)$$

$$F_2^{aabb}(t_1, t_2) = \frac{1}{N^2 M^2} \sum_{ij, \alpha\beta} \langle yb_{i\alpha 4}^a(t_1) yb_{j\beta 3}^{\dagger a}(0) yb_{i\alpha 2}^{\dagger b}(t_2) yb_{j\beta 1}^b(0) \rangle \quad (4.4b)$$

where the superscripts 1, 2, 3, 4 denote the branch on the SK contour and the average $\langle \dots \rangle$ is with respect to replicated generating function [Eq.(4.2)].

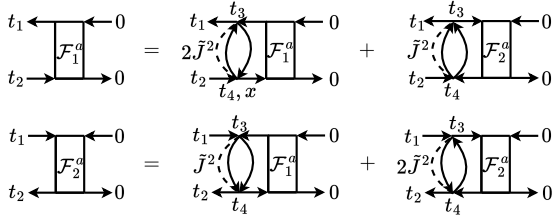


FIG. 4.2. Diagrammatic representation of the kernel equation in Eq.(4.6b) for $\mathcal{O}(1/(NM))$ term, ($\mathcal{F}_{1,2}^a$) in the OTOC $F_{1,2}^a(t_1, t_2)$. The solid horizontal lines denote dressed retarded and advanced propagators G_R , G_A , and the vertical rung denotes the Wightmann correlations G_{lr}^+ and G_{lr}^- . The dashed line represents disorder averaging. We suppress replica indices of the vertices in the ladder diagram to avoid cluttering.

The diagrams that contribute to the OTOC can be arranged in powers of $1/(NM)$. $\mathcal{O}(1)$ diagrams are disconnected and do not contribute to the growth of OTOC. The contribution, \mathcal{F}_μ^{aabb} at $\mathcal{O}(1/(NM))$ form the ladder diagrams (Fig. 4.2) that grow exponentially, i.e., for $F_\mu^{aabb}(t_1, t_2) = F_\mu^{0aabb}(t_1, t_2) + (1/(NM))\mathcal{F}_\mu^{aabb}(t_1, t_2) + \mathcal{O}(1/(N^2 M^2))$ ($\mu = 1, 2$), $\mathcal{F}_\mu \sim e^{\lambda_L t}$. The ladder diagrams can be written in the form of a Bethe-Salpeter-like

equation, similar to SYK-type models^{6,8,73},

$$\mathcal{F}_1^{aabb}(t_1, t_2) = \sum_c \int_{t_3, t_4} [K_{11}^{aacc}(t_1, t_2, t_3, t_4) \mathcal{F}_1^{ccbb}(t_3, t_4) + K_{12}^{aacc}(t_1, t_2, t_3, t_4) \mathcal{F}_2^{ccbb}(t_3, t_4)] \quad (4.5a)$$

$$\mathcal{F}_2^{aabb}(t_1, t_2) = \sum_c \int_{t_3, t_4} [K_{21}^{aacc}(t_1, t_2, t_3, t_4) \mathcal{F}_1^{ccbb}(t_3, t_4) + K_{22}^{aacc}(t_1, t_2, t_3, t_4) \mathcal{F}_2^{ccbb}(t_3, t_4)]. \quad (4.5b)$$

Here $\int_{t_3, t_4} = \int dt_3 dt_4$. In the chaotic growth regime, $\lambda_L^{-1} \lesssim t < \lambda_L^{-1} \ln N$, the propagators along the horizontal lines, from t_1 to t_3 and from t_2 to t_4 in Fig. 4.2 can be approximated by retarded and advanced propagators^{3,6,61}. Since the retarded and advanced propagators are replica-diagonal in both PM and SG phases, the kernel equations become,

$$\mathcal{F}_1^a(t_1, t_2) = \int dt_3 dt_4 K_{11}^a(t_1, t_2, t_3, t_4) \mathcal{F}_1^a(t_3, t_4) + \int dt_3 dt_4 K_{12}^a(t_1, t_2, t_3, t_4) \mathcal{F}_2^a(t_3, t_4) \quad (4.6a)$$

$$\mathcal{F}_2^a(t_1, t_2) = \int dt_3 dt_4 K_{21}^a(t_1, t_2, t_3, t_4) \mathcal{F}_1^a(t_3, t_4) + \int dt_3 dt_4 K_{22}^a(t_1, t_2, t_3, t_4) \mathcal{F}_2^a(t_3, t_4), \quad (4.6b)$$

where $\mathcal{F}_\mu^a(t_1, t_2) \equiv \mathcal{F}_\mu^{aaaa}(t_1, t_2)$ and the kernels are given by

$$\begin{aligned} K_{11}^a(t_1, t_2, t_3, t_4) &= 2\tilde{J}^2 G_A(t_{31}) G_R(t_{24}) G_{lr}^+(t_{43}) G_{lr}^-(t_{34}) \\ K_{12}^a(t_1, t_2, t_3, t_4) &= \tilde{J}^2 G_A(t_{31}) G_R(t_{24}) G_{lr}^+(t_{43}) G_{lr}^+(t_{43}) \\ K_{21}^a(t_1, t_2, t_3, t_4) &= \tilde{J}^2 G_R(t_{13}) G_A(t_{42}) G_{lr}^-(t_{34}) G_{lr}^-(t_{34}) \\ K_{22}^a(t_1, t_2, t_3, t_4) &= 2\tilde{J}^2 G_R(t_{13}) G_A(t_{42}) G_{lr}^-(t_{34}) G_{lr}^+(t_{43}). \end{aligned} \quad (4.7)$$

Here all Green's functions are replica diagonal and $G_{lr}^\pm(t)$ refers to Wightmann correlations functions (Appendix A 2).

Using the exponential ansatz in the growth regime, $\mathcal{F}_\mu^a(t_1, t_2) = e^{\lambda_L(t_1+t_2)/2} f_\mu^a(t_1 - t_2)$ and taking the Fourier transform of the kernel equations [Eq.(4.6)], leads to eigenvalue equations in the frequency space with eigenvalue, $\lambda_e = 1$. For the PM phase, these eigenvalue equations are

$$\tilde{J}^2 G_A \left(-\omega - i \frac{\lambda_L}{2} \right) G_R \left(-\omega + i \frac{\lambda_L}{2} \right) \left[2 \int d\omega' g_1(\omega - \omega') f_1^a(\omega') + \int d\omega' g_2(-(\omega - \omega')) f_2^a(\omega') \right] = f_1^a(\omega) \quad (4.8a)$$

$$\tilde{J}^2 G_R \left(\omega + i \frac{\lambda_L}{2} \right) G_A \left(\omega - i \frac{\lambda_L}{2} \right) \left[\int d\omega' g_2(\omega - \omega') f_1^a(\omega') + 2 \int d\omega' g_1(\omega - \omega') f_2^a(\omega') \right] = f_2^a(\omega) \quad (4.8b)$$

where

$$\begin{aligned} g_1(\omega) &= \frac{1}{4\pi^2} \int d\omega_1 G_{lr}^+(\omega_1) G_{lr}^-(\omega + \omega_1) \\ &= \frac{1}{4} \int d\omega_1 \frac{\rho(\omega_1)\rho(\omega + \omega_1)}{\sinh \frac{\beta\omega_1}{2} \sinh \frac{\beta(\omega + \omega_1)}{2}} \end{aligned} \quad (4.9a)$$

$$\begin{aligned} g_2(\omega) &= \frac{1}{4\pi^2} \int d\omega_1 G_{lr}^+(\omega_1) G_{lr}^+(\omega - \omega_1) \\ &= \frac{1}{4} \int d\omega_1 \frac{\rho(\omega_1)\rho(\omega - \omega_1)}{\sinh \frac{\beta\omega_1}{2} \sinh \frac{\beta(\omega - \omega_1)}{2}}. \end{aligned} \quad (4.9b)$$

Here $\rho(\omega) = -(1/\pi)\text{Im} G_R(\omega)$ is the bosonic spectral function (Appendix A). We discretize the kernel equations [Eqs.(4.8)] in frequency and diagonalize the resulting matrix kernel for different trial values of λ_L . Eventually, the Lyapunov exponent λ_L is obtained from the one for which the kernel has at least one eigenvalue $\lambda_e = 1$.

Similarly, for the 1RSB SG phase, the kernel equations are

$$\begin{aligned} \tilde{J}^2 G_A \left(-\omega - i\frac{\lambda_L}{2} \right) G_R \left(-\omega + i\frac{\lambda_L}{2} \right) &\left[2 \left(g^2 f_1^a(\omega) + g \int \frac{d\omega'}{2\pi} \tilde{g}_{lr}(\omega - \omega') f_1^a(\omega') + g \int \frac{d\omega'}{2\pi} \tilde{g}_{lr}(\omega' - \omega) f_1^a(\omega') \right. \right. \\ &\left. \left. + \int d\omega' \tilde{g}_1(\omega - \omega') f_1^a(\omega') \right) + g^2 f_2^a(\omega) + 2g \int \frac{d\omega'}{2\pi} \tilde{g}_{lr}(-\omega + \omega') f_2^a(\omega') + \int d\omega' \tilde{g}_2(-\omega + \omega') f_2^a(\omega') \right] = f_1^a(\omega) \end{aligned} \quad (4.10a)$$

$$\begin{aligned} \tilde{J}^2 G_A \left(\omega - i\frac{\lambda_L}{2} \right) G_R \left(\omega + i\frac{\lambda_L}{2} \right) &\left[2 \left(g^2 f_2^a(\omega) + g \int \frac{d\omega'}{2\pi} \tilde{g}_{lr}(\omega - \omega') f_2^a(\omega') + g \int \frac{d\omega'}{2\pi} \tilde{g}_{lr}(\omega' - \omega) f_2^a(\omega') \right. \right. \\ &\left. \left. + \int d\omega' \tilde{g}_1(\omega - \omega') f_2^a(\omega') \right) + g^2 f_1^a(\omega) + 2g \int \frac{d\omega'}{2\pi} \tilde{g}_{lr}(\omega - \omega') f_1^a(\omega') + \int d\omega' \tilde{g}_2(\omega - \omega') f_1^a(\omega') \right] = f_2^a(\omega) \end{aligned} \quad (4.10b)$$

In the above equations, $\tilde{g}_1(\omega)$ and $\tilde{g}_2(\omega)$ are the same as in Eqs.(4.9a),(4.9b) in terms of the SG spectral function $\rho(\omega)$. We obtain λ_L as a function of S and T by separately solving Eq.(4.8) for the PM phase, and Eq.(4.10) for the SG phase, with the retarded, advanced and Wightmann functions obtained from the large N saddle point equations (Appendix A).

The crucial difference between the PM and SG phases is encoded in the ladder kernel [Eq.(4.7)] through the Wightmann correlators. In the SG phase,

$$G_{lr}^+(\omega) = G_{lr}^-(\omega) = 2\pi g \delta(\omega) \epsilon_{ab} + \pi \rho(\omega) / (\sinh(\beta\omega/2)) \delta_{ab} \quad (4.11)$$

In contrast, the delta function term is absent in the PM phase, where $g = \sqrt{q_{EA}} = 0$.

We compare the results for $\lambda_L(S, T)$ obtained using the above formalism for the effective zero-dimensional SY model with the $\lambda_L(\Gamma, T)$ for the effective zero-dimensional p -spin glass model. The OTOC formalism for the latter is very similar to that of SY model, but somewhat simpler. To extract $\lambda_L(\Gamma, T)$, we compute the following regularized OTOC³¹ for the p -spin glass model,

$$F(t_1, t_2) = \frac{1}{N^2} \sum_{i,j} \overline{\text{Tr} \left[y_{s_i}(t_1) y_{s_j}(0) y_{s_i}(t_2) y_{s_j}(0) \right]}, \quad (4.12)$$

We skip the details of the formalism here since those have been already described in Ref. 31. We briefly discuss a

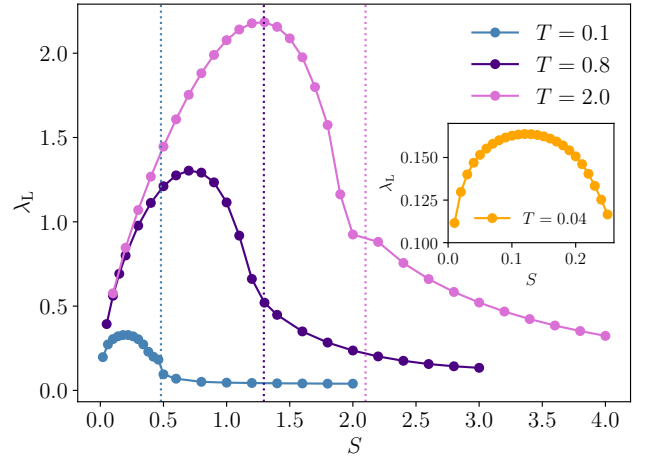


FIG. 4.3. **Variation of Lyapunov exponent with S in the SY model.** $\lambda_L(S)$ for $T = 0.1$, $T = 0.8$ and $T = 2.0$ (in units of \tilde{J}), across the PM-SG phase transition marked by the vertical lines at $S_{SG} \simeq 0.48, 1.29, 2.1$, respectively. λ_L has a maximum in the PM phase and changes non-monotonically. $\lambda_L \sim 1/S^{1.7}$ in the SG phase. The inset shows $\lambda_L(S)$ for $T = 0.04$ in the PM phase

few additional details for the non-local OTOC for p -spin glass chain model [Eq.(2.3)] in Sec. 5 along with those for the SY chain [Eq.(2.1)].

A. Lyapunov exponent across spin glass transition in the SY model

We obtain $\lambda_L(S, T)$ in the PM and SG phases by separately solving the corresponding large N kernel equations (Sec. 4) for the two phases. Specifically, as shown in Fig. 3.1, we take cuts along several S and T , namely, from small S (low- T) quantum critical region *a*. $S = 0.5$ (*d*. $T = 0.1$), from intermediate- S (intermediate- T) crossover region between quantum critical and local moment behavior *b*. $S = 1$ (*e*. $T = 0.8$), and from large S (high- T) local moment region *c*. $S = 2$ (*f*. $T = 2$), as a function of T (S). We set $\tilde{J} = 1$ as the unit of temperature (energy). The results for $\lambda_L(S, T)$ are qualitatively similar for all the cuts, as we discuss below.

S dependence of Lyapunov exponent.—We first show the Lyapunov exponent as a function of S in Fig. 4.3 from PM to spin glass phase for four temperatures, $T = 0.04, 0.1, 0.8, 2.0$. In all the cases, the Lyapunov exponent λ_L has a non-monotonic dependence on S within the PM phase; λ_L initially increases with S till a value $S_m(T)$ where λ_L has a broad peak, and then it decreases with further increase of S approaching the critical value of S , $S_{SG}(T)$ for the spin glass transition, which is obtained from the breakpoint criterion $m(T, S_{SG}) = 1$. The non-monotonic $\lambda_L(S)$ in the PM phase can be heuristically understood from the behavior of the spectral function. As discussed in Appendix A 2, in our numerical solution of the real-frequency saddle-point equation [Eq. (3.4)], e.g., at $T = 0.1, 0.8$, for small $S \simeq 0.05 - 0.2$, the spectral function has either a spin liquid or a local moment like form [see Figs. A.1(a), A.3(a)], with a peak at $\omega \propto T$, but still sufficiently larger than T , and very little spectral weight around $\omega = 0$. The peak moves closer to zero energy with increasing S and the spectral density increases around $\omega = 0$. As a result, λ_L is small at small S and increases with S till a maximum value in the PM phase. However, beyond the maximum, closer to the SG transition, there is a loss of spectral weight at intermediate energies or *pseudogap*⁶⁹ like feature, in between a narrower low-energy peak and a broad peak at high energies. This presumably leads to decreases of λ_L approaching the SG transition. Thus, λ_L exhibits a non-monotonic dependence on S in the PM region.

In the PM phase, especially in the quantum critical region IV in Fig. 3.1, for $S \rightarrow 0$, we expect dominantly spin liquid behavior and $\lambda_L(S \rightarrow 0, T) \rightarrow \lambda_L^{\text{SYK}}(T)$, i.e., λ_L should asymptotically approach the T -dependent Lyapunov exponent⁸, $\lambda_L^{\text{SYK}}(T)$, of the SYK spin liquid⁴⁰ at $S = 0$. Based on this expectation we fit our data with $\lambda_L(S, T) \simeq \lambda_L(0, T) + aS^{\alpha_\lambda}$ in the PM phase for small values of S , before reaching the peak [Fig. 4.3]. As shown in Fig. 4.4(a,b) for $T = 0.04, 0.8, 1.0$, we find reasonable fit with $\alpha_\lambda \simeq 0.2 - 0.6$. However, due to this S dependence, there is a rapid decrease of $\lambda_L(S)$ for $S \rightarrow 0$, as seen in Fig. 4.4(a). As a result, the extrapolated $\lambda_L(0, T)$ for $S \rightarrow 0$ from the fit consistently turns out to be very low, and much smaller than $\lambda_L^{\text{SYK}}(T)$ ⁸, even at low temper-

atures $T \simeq 0.04 - 0.1$. Nevertheless, our real frequency saddle-point solutions, e.g., the computed bosonic spectral function, for $S \leq 0.05 \approx S_{max}$ at low T are consistent with the conformal spin liquid solutions^{38,40,42} for $|\omega|, T \ll J$ as well as the numerical spin liquid solutions obtained in Ref. 69, as discussed in Appendix A 2. Thus, our results indicate strong S (and T) dependent corrections to the conformal limit of the spectral function, and, consequently, $\lambda_L \ll 2\pi T$, in the spin liquid region, even for small $S \lesssim 0.05$. We also note that our numerical saddle-point solutions at small S smoothly to the solutions at higher S , as evident from the smooth evolution of $\lambda_L(S)$ in Figs. 4.3, 4.4(a) for all T .

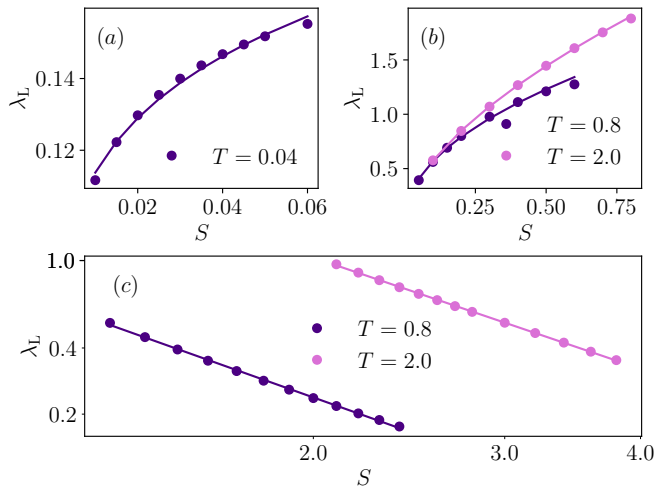


FIG. 4.4. S dependence of λ_L in PM and SG phases of SY model. λ_L is shown as a function of S . (a) In the PM phase, before reaching the maximum [Fig. 4.3], λ_L varies as, $\lambda_L(S, T) \simeq \lambda_L(0, T) + aS^{\alpha_\lambda}$, shown as line fit to the data (circles) for $T = 0.04$ with $\alpha_\lambda \approx 0.2$, and (b) for $T = 0.8, 2.0$ with $\alpha_\lambda \approx 0.5, 0.6$, respectively. (c) λ_L decays with S as a power law in the SG phase, shown as straight line fit to the data (circles) on log-log scale. $\lambda_L \sim 1/S^{1.7}$ for $T = 0.8, 2.0$.

The Lyapunov exponent appears to have weak signature of singularity in the form discontinuity/change of slope at S_{SG} for $T = 0.1, 2.0$. The Lyapunov exponent, like other usual observable, e.g., the free-energy or relaxation time, can have genuine singularity across a phase transition. However, in contrast, we find $\lambda_L(S)$ to be continuous for $T = 0.8$ across the SG transition. Moreover, we cannot rule out numerical artifact due to problem in obtaining a converged solution of the saddle-point equations very close to the transition, as well as, due to difficulty in matching the PM and 1RSB SG solutions approaching from two different sides of the SG transition. As a result, we refrain from making any strong statement about the singularity of λ_L across the SG transition. In the SG phase, $\lambda_L(S)$ decreases monotonically as $\sim 1/S^{1.7}$, as shown in Fig. 4.4(b). The reduction of λ_L with increasing S or its increase with decreasing S (increasing quantum fluctuations) can be understood qualitatively by drawing analogy with the similar depen-

dence of λ_L on Γ in the p -spin glass model. In the latter case, the kernel equations for λ_L can be mapped to a solvable one-dimensional Schrödinger equation³¹. As a result, it can be shown by that $\lambda_L \sim T^2/q_{\text{EA}}^{3/2}$. Thus λ_L increases with increasing quantum fluctuations in the SG phase due to the reduction of EA order parameter. Similar relation between λ_L and q_{EA} can be expected for the SY model, however, the kernel equations [Eq.(4.10)] are much more complicated in this case, compared to the p -spin glass model³¹, and we could not map them into a solvable quantum mechanical problem.

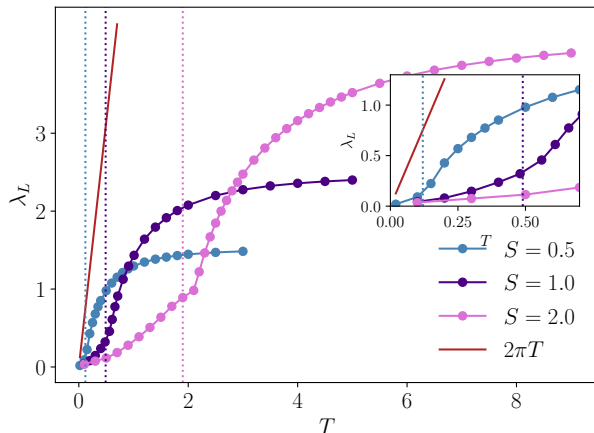


FIG. 4.5. **Temperature dependence of Lyapunov exponent in SY model.** λ_L as function of T for $S = 0.5$, $S = 1.0$ and $S = 2.0$ across the SG to PM phase transitions, marked by the vertical lines at $T_{SG} \simeq 0.12, 0.49, 1.9$, respectively. The inset shows zoomed in view near the transitions for smaller S values.

Temperature dependence of λ_L .— We show the temperature dependence of λ_L in Fig. 4.5 for three values of S , $S = 0.5, 1.0, 2.0$. In all these case, in contrast to non-monotonic dependence of λ_L on S , λ_L monotonically increases with temperature throughout SG and PM phases, with possibly a weak slope change at the transition [Fig. 4.5 (inset)]. The dependence of λ_L on temperature, in SG and PM phases is summarized below. Similar to the case of p -spin glass³¹, λ_L follows a power-law T dependence in the SG phase for SY model. For large S , $\lambda_L \sim T^{\beta_\lambda}$, where the exponent $\beta_\lambda \approx 1.5$ weakly depends on S , as shown in Fig. 4.6. For small S , $\lambda_L \sim T$, i.e., has a linear T dependence [Fig. 4.7(a)], albeit in a narrow range of temperature accessible for $T \lesssim T_{SG}$ for small S . The deviation from linearity could be due to numerical error since λ_L is very small at low temperatures in SG phase and it is difficult to obtain an accurate estimate numerically in this regime.

In the PM phase for $T > T_{SG}$, for all values of S , λ_L increases near the transition logarithmically in T as, $a \ln T + c$, with constants a and c that depend on S [Fig. 4.7(b)]. $\lambda_L(T)$ eventually tends to saturate at high temperature, as shown in Fig. 4.7. The logarithmic depen-

dence of $\lambda_L(T)$, albeit over a small temperature window near T_{SG} in the PM phase, even for relatively large $S = 2$, is somewhat surprising. For classical spin models^{55,56}, $\lambda_L \sim \sqrt{T}$ is found at high temperature, e.g., above thermal phase transitions. The \sqrt{T} behavior is expected for classical models from fairly general considerations⁷⁴. In our case, the initial increase of $\lambda_L(T)$ for $T \gtrsim T_{SG}$ cannot be fitted with a power law like \sqrt{T} . Nevertheless, qualitatively, the increase of λ_L is expected with increasing T due to gradual unfreezing of spins going away from T_{SG} . As discussed in Appendix A 2, near T_{SG} in the PM phase, the spectral function has a sharp peak close to $\omega = 0$ separated from high-frequency spectral weight with a pseudogap-like dip at intermediate frequencies. The sharp peak can be understood as a relic of the delta function peak $\sim \delta(\omega)$ that appears in correlation functions (see Appendix A 2) in the SG phase, e.g., in the Wightmann correlation function [Eq.(4.11)]. The delta function peak indicates static order and spin freezing. With increasing T , the low- and high-frequency peaks move closer filling up the pseudogap at intermediate frequencies due to unfreezing of spins. This spectral weight transfer correlates with increase of λ_L with T . Like in the SYK model⁸, λ_L is expected to saturate eventually at high temperature since the model has a bounded spectrum. This is unlike the p -spin glass model which has an unbounded spectrum due to unbounded kinetic energy. The latter renders interaction effect negligible³¹ at high temperature in the p -spin glass model leading to decrease of $\lambda_L \sim 1/T^2$ for $T \gg \tilde{J}$.

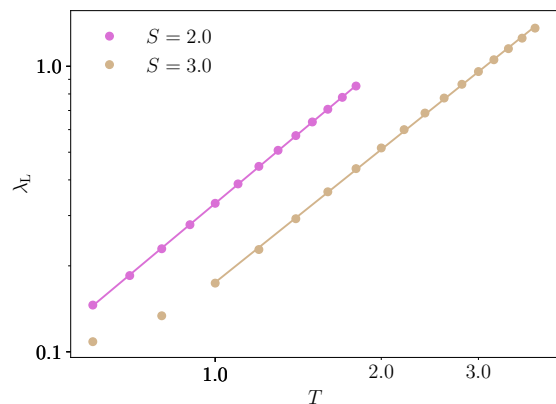


FIG. 4.6. **Power-law temperature dependence of λ_L in the SG phase for large S in SY model.** The straight lines show the power-law fit, $\lambda_L \sim T^{\beta_\lambda}$ to the data (circles), on log-log plot with $\beta_\lambda = 1.6, 1.5$ for $S = 2.0, 3.0$, respectively.

The non-monotonic behavior of $\lambda_L(S)$ [Fig. 4.3] in the PM phase of the SY model is similar to the non-monotonic behavior seen³¹ for $\lambda_L(\Gamma)$ or $\lambda_L(\hbar)$, i.e., as a function of quantum parameter, in the p -spin glass model [Eq.(2.3)] as shown in Fig. 4.8. However, in the latter model, in contrast to the $\lambda_L(T)$ [Fig. 4.5] in the SY model, λ_L also shows non-monotonic dependence on T

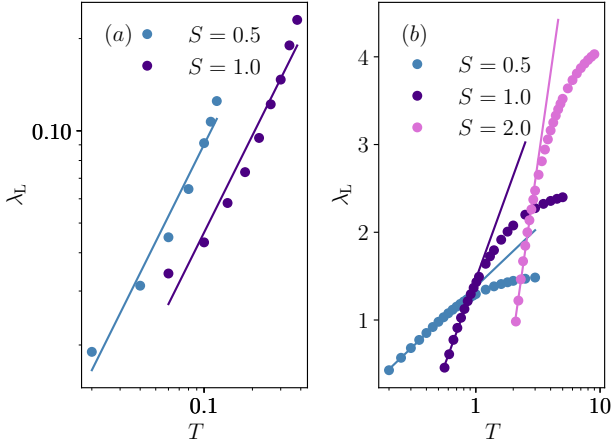


FIG. 4.7. **Temperature dependence of λ_L in PM and SG phases of SY model.** (a) λ_L increases linearly with temperature as $\lambda_L \sim T$ in the SG phase for small S , shown for $S = 0.5, 1.0$ as lines fitted to the data (circles) on log-log scale. (b) In the PM phase, λ_L shows logarithmic dependence on temperature, $a \ln T + c$ (line) initially before it saturates to a constant value for large T (Fig. 4.5), as shown for $S = 0.5, 1.0, 2.0$ in semi-log plot (λ_L vs. $\ln T$).

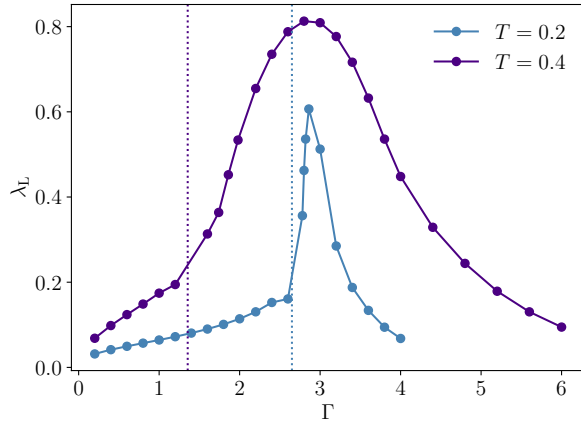


FIG. 4.8. **Variation of Lyapunov exponent with quantum parameter Γ in the p -spin glass model.** λ_L as function of Γ for $T = 0.2$ and $T = 0.4$ across the PM-SG phase transition marked by the vertical lines at $\Gamma_{SG} \simeq 2.65, 1.35$ respectively. λ_L changes non-monotonically and has a maximum above the glass transition in the PM phase³¹.

in the PM phase, as in Fig. 4.9. The broad peak related to the non-monotonic $\lambda_L(\Gamma, T)$ in the PM phase of the p -spin glass model correlates with the onset of complex glassy relaxation³¹, where the dynamics start getting dominated by saddle points of the glassy energy landscape³⁵. In the classical limit ($\Gamma \rightarrow 0$) of the p -spin glass model, the origin of the broad peak was shown to be related to the interplay of the rapid increase of relaxation time approaching the glass transition, and weaken-

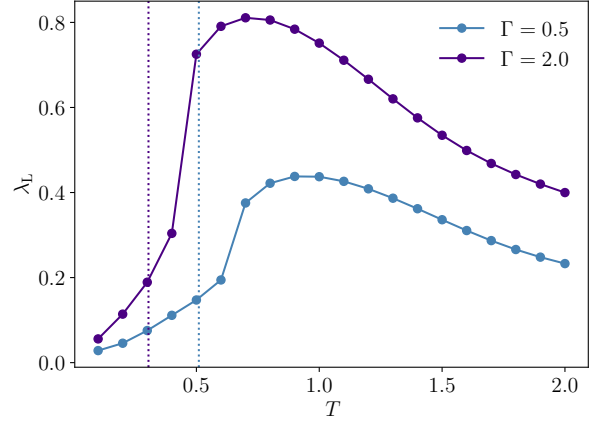


FIG. 4.9. **Temperature dependence of λ_L in the p -spin glass model.** λ_L as function of T for $\Gamma = 0.5$ and $\Gamma = 2.0$ across the PM-SG phase transition marked by the vertical lines at $T_{SG} \sim 0.3, 0.51$ respectively. λ_L changes non-monotonically and has a maximum above the glass transition in the PM phase³¹

ing of interaction effects due to unbounded kinetic energy growth with increasing temperature. The interplay leads to a crossover from strong to weak chaos with increasing T , manifested as a broad peak in λ_L coinciding with the onset of two-step glassy relaxation regime³¹. Due to its bounded spectrum, such crossover from strong to weak chaos with temperature is absent in the SY model, and the $\lambda_L(T)$ monotonically increases with T in the PM phase till it saturates at high temperature [Fig. 4.5]. However, as already discussed, a non-monotonic $\lambda_L(S)$ is still observed in the PM phase due to change of spectral properties as a function of S .

The two-step glassy relaxation, seen for the p -spin glass model³¹, can also be observed in the PM phase of the SY model above the glass transition. To this end, we calculate the correlation function using the Fluctuation dissipation theorem $C(t) = -(i/M) \sum_{\alpha} \langle \{b_{i\alpha,x}(t), b_{i\alpha,x}^{\dagger}(0)\} \rangle = 2 \int (d\omega/2\pi) e^{-i\omega t} \coth(\beta\omega/2) \text{Im} G_R(\omega)$. We show the correlation function for several S in Fig. 4.10 at $T = 0.8$, and for several T in Fig. 4.11 at $S = 1$, above the SG transition. The gradual onset of the two-step relaxation is evident. This suggests that the onset of two-step glassy relaxation is not a sufficient condition to realize a peak in the Lyapunov exponent.

5. BUTTERFLY VELOCITY IN QUANTUM SPIN GLASS CHAINS

In this section we study the spatial spreading of chaos, first in the SY model and then in the p -spin glass model.

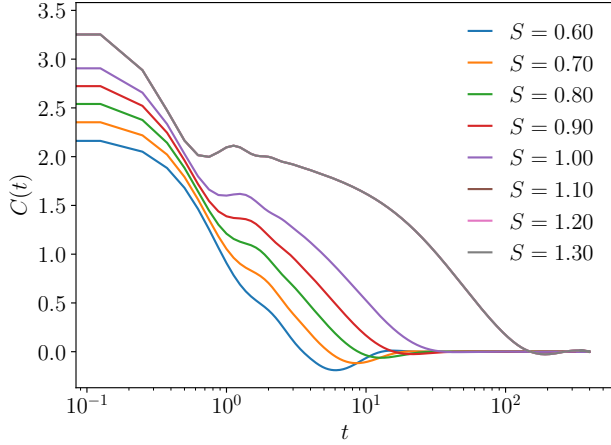


FIG. 4.10. **Onset of glassy relaxation with S in SY model.** Correlation function $C(t)$ in the PM phase near the PM-SG phase transition for a fixed value $T = 0.8$ and different values of S . As we approach the transition from the PM phase, near the transition at $S_{SG} \simeq 1.3$, the two step glassy relaxation is more pronounced.

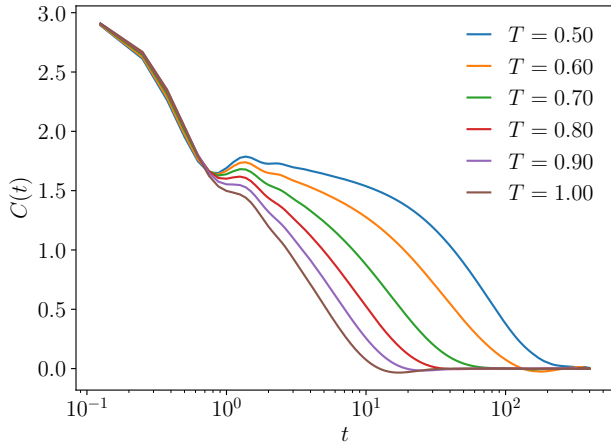


FIG. 4.11. **Onset of glassy relaxation with temperature in SY model.** Correlation function $C(t)$ in the PM phase near the PM-SG phase transition for a fixed value of $S = 1.0$ and different values of T . The two step glassy relaxation is more pronounced as we approach $T_{SG} = 0.5$ from the PM phase.

A. Butterfly velocity across spin glass transition in the SY chain

In the previous section, we calculated λ_L which determines the temporal growth of the four-point OTOC. Due to the spatial locality of our generalized 1D SY chain model [Eq.(2.1)], we can study the spatio-temporal dynamics of growth and spread of chaos. The quantity which measures the propensity of spatial spreading of chaos is the butterfly velocity, v_B . The operators that

form large commutators with an initial operator lie inside a region of space-time that forms a *light cone*^{41,75}, signifying a ballistic spread of chaos. The speed or velocity that forms the boundary of the light cone is defined as v_B . Like the Lyapunov exponent λ_L , the butterfly speed v_B provides a state-dependent measure of operator growth and spreading, and can be related⁷⁶ to the well-known Lieb-Robinson velocity bound⁷⁷, that gives state-independent measure in terms of operator norm. To this end, we calculate the following disorder-averaged regularized spatio-temporal OTOCs for the SY model,

$$\begin{aligned} F_{1,x}(t_1, t_2) &= \frac{1}{N^2 M^2} \sum_{ij\alpha\beta} \overline{\text{Tr}[yb_{i\alpha,x}^\dagger(t_1)yb_{j\beta,0}^\dagger(0)yb_{i\alpha,x}(t_2)yb_{j\beta,0}(0)]} \\ & \quad (5.1a) \end{aligned}$$

$$\begin{aligned} F_{2,x}(t_1, t_2) &= \frac{1}{N^2 M^2} \sum_{ij\alpha\beta} \overline{\text{Tr}[yb_{i\alpha,x}(t_1)yb_{j\beta,0}^\dagger(0)yb_{i\alpha,x}^\dagger(t_2)yb_{j\beta,0}(0)]} \\ & \quad (5.1b) \end{aligned}$$

As discussed in Sec. 4 for the case of the onsite OTOCs, which is equivalent to OTOCs in zero-dimensional SY model, the above non-local OTOCs are computed via a replicated Keldysh field theory, where the OTOCs become replica diagonal up to $\mathcal{O}(1/(NM))$ diagrams. The latter are arranged as ladder series that can be written in the form of Bethe-Salpeter-like equations, as shown in Fig. 5.1,

$$\begin{aligned} \mathcal{F}_{1,x}^a(t_1, t_2) &= \int dx' \int dt_3 dt_4 \left[K_{11,xx'}^a(t_1, t_2, t_3, t_4) \right. \\ & \quad \left. \mathcal{F}_{1,x'}^a(t_3, t_4) + K_{12,xx'}^a(t_1, t_2, t_3, t_4) \mathcal{F}_{2,x'}^a(t_3, t_4) \right], \end{aligned} \quad (5.2a)$$

$$\begin{aligned} \mathcal{F}_{2,x}^a(t_1, t_2) &= \int dx' \int dt_3 dt_4 \left[K_{21,xx'}^a(t_1, t_2, t_3, t_4) \right. \\ & \quad \left. \mathcal{F}_{1,x'}^a(t_3, t_4) + K_{22,xx'}^a(t_1, t_2, t_3, t_4) \mathcal{F}_{2,x'}^a(t_3, t_4) \right]. \end{aligned} \quad (5.2b)$$

In the above, the kernels, which are diagrammatically shown in Fig. 5.1, are given in Eqs.(5.3). Although we have not indicated explicitly, all the Green's functions appearing in the kernel elements are replica diagonal. Since the saddle-point Green's function (Sec. 3A) of the extended 1D SY chain model are local and independent of x , the kernel elements are translation invariant, as in Eqs.(5.3). Thus, after Fourier transforming Eqs.(5.2) to momentum space, we obtain equations for the Fourier transform of $\mathcal{F}_{\mu,x}^a(t_1, t_2)$ ($\mu = 1, 2$), $\mathcal{F}_{\mu,p}^a(t_1, t_2)$. The kernel elements for a given momentum p are obtained by replacing \tilde{J}^2 in the local kernel elements of Eqs.(4.7) by momentum dependent prefactors, as shown in Eqs.(5.4), where $\alpha = 2J'^2/\tilde{J}^2$. In this section, as discussed below, we calculate butterfly velocity v_B using two methods—(1)

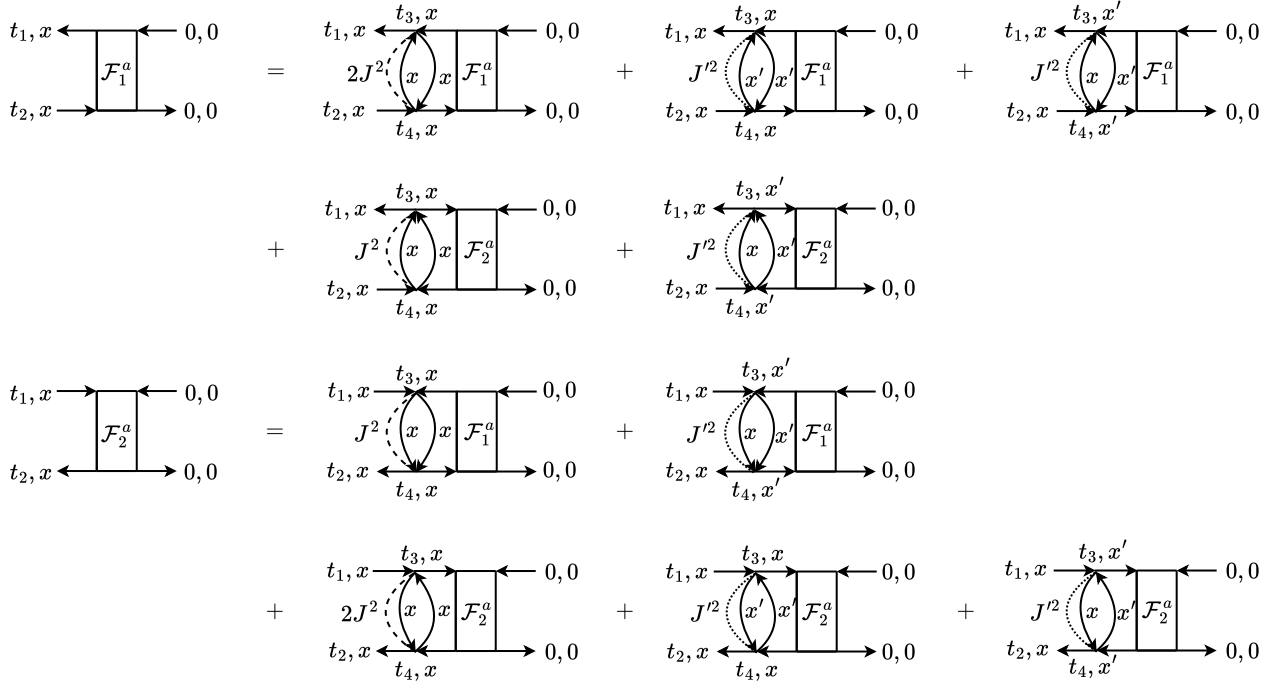


FIG. 5.1. Diagrammatic representation of the Kernel equation in Eq. 5.2 for $\mathcal{O}(1/(NM))$ term, $\mathcal{F}_{\mu,x}^a(t_1, t_2)$ in the OTOC $F_{\mu,x}^a(t_1, t_2)$ ($\mu = 1, 2$). The solid horizontal lines denote dressed retarded and advanced propagators G_R, G_A , and the vertical rung denotes the Wightmann correlations G_{lr}^+ and G_{lr}^- . The dashed and dotted lines denote disorder averaging over J and J' couplings, respectively in Eq.(2.1). Here $x' = x \pm 1$. We suppress replica indices for the vertices to avoid cluttering.

a fully numerical method, which uses a straightforward generalization of the exponential growth ansatz for the local OTOC (Sec. 4) for each momentum mode; we refer

to this as *real p method*, and (2) a semi-analytic method, called the *single mode ansatz*, following Ref. 41. Here we refer to this as *imaginary p method*.

$$K_{11,xx'}^a(t_1, t_2; t_3, t_4) = G_A(t_{31})G_R(t_{24})G_{lr}^+(t_{43})G_{lr}^-(t_{34})\left(2J^2\delta_{x,x'} + J'^2(\delta_{x,x'} + \delta_{x\pm 1,x'})\right) \quad (5.3a)$$

$$K_{12,xx'}^a(t_1, t_2; t_3, t_4) = G_A(t_{31})G_R(t_{24})G_{lr}^+(t_{43})G_{lr}^+(t_{43})\left(J^2\delta_{x,x'} + J'^2(\delta_{x\pm 1,x'})\right) \quad (5.3b)$$

$$K_{21,xx'}^a(t_1, t_2; t_3, t_4) = G_R(t_{13})G_A(t_{42})G_{lr}^-(t_{34})G_{lr}^-(t_{34})\left(J^2\delta_{x,x'} + J'^2(\delta_{x\pm 1,x'})\right) \quad (5.3c)$$

$$K_{22,xx'}^a(t_1, t_2; t_3, t_4) = G_R(t_{13})G_A(t_{42})G_{lr}^-(t_{34})G_{lr}^+(t_{43})\left(2J^2\delta_{x,x'} + J'^2(\delta_{x,x'} + \delta_{x\pm 1,x'})\right) \quad (5.3d)$$

$$K_{11,p}^a(t_1, t_2; t_3, t_4) = \tilde{J}^2\left(2 - \frac{\alpha}{2}(3 - 2\cos p)\right)G_A(t_{31})G_R(t_{24})G_{lr}^+(t_{43})G_{lr}^-(t_{34}) \quad (5.4a)$$

$$K_{12,p}^a(t_1, t_2; t_3, t_4) = \tilde{J}^2\left(1 - \alpha(1 - \cos p)\right)G_A(t_{31})G_R(t_{24})G_{lr}^+(t_{43})G_{lr}^+(t_{43}) \quad (5.4b)$$

$$K_{21,p}^a(t_1, t_2; t_3, t_4) = \tilde{J}^2\left(1 - \alpha(1 - \cos p)\right)G_R(t_{13})G_A(t_{42})G_{lr}^-(t_{34})G_{lr}^-(t_{34}) \quad (5.4c)$$

$$K_{22,p}^a(t_1, t_2; t_3, t_4) = \tilde{J}^2\left(2 - \frac{\alpha}{2}(3 - 2\cos p)\right)G_R(t_{13})G_A(t_{42})G_{lr}^-(t_{34})G_{lr}^+(t_{43}) \quad (5.4d)$$

Real p method.— As in Sec. 4, we take an exponen-

tial growth ansatz, $\mathcal{F}_{\mu,p}(t_1, t_2) = e^{\lambda_L(p)(t_1+t_2)/2} f_{\mu,p}^a(t_1 -$

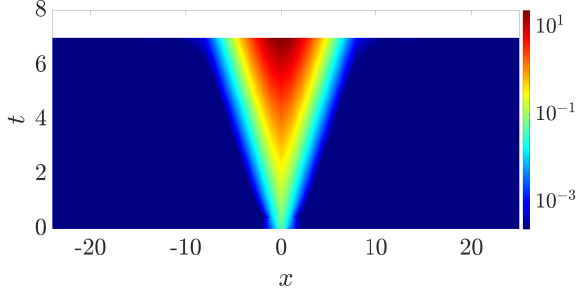


FIG. 5.2. The growing part of OTOC, $\mathcal{F}_{1,x}(t)$, is plotted on the $x-t$ plane in logarithmic scale, as indicated in the color bar at $T = 0.8$ and $S = 1.0$ using the real p method.

t_2), and extract the momentum-dependent Lyapunov exponent $\lambda_L(p)$ by demanding that the matrix kernel has at least one eigenvalue equal to 1 (typically non-degenerate). We compute the eigenvector corresponding to the eigenvalue 1 to obtain $f_{\mu,p}^a(\omega)$. To extract v_B , we calculate $\mathcal{F}_{\mu,p}^a(t,t) = e^{\lambda_L(p)t} f_{\mu,p}^a(0)$, where $f_{\mu,p}(0) = \int (d\omega/2\pi) f_{\mu,p}(\omega)$. We Fourier transform to the position space, $\mathcal{F}_{\mu,x}(t) \equiv \mathcal{F}_{\mu,x}^a(t,t) = (1/L) \sum_p e^{ixp} \mathcal{F}_{\mu,p}(t,t)$ where L is the number of sites or the number of discrete p values taken within the Brillouin zone $[-\pi, \pi]$ for unit lattice spacing. We show in Fig. 5.2 that $\mathcal{F}_{1,x}(t)$ exhibits quite distinctive light cone. The magnitude of $\mathcal{F}_{\mu,p}(t,t)$ cannot be fixed, i.e., the eigenvector can be multiplied by an arbitrary factor, for the kernel equations. Thus, we compute the light-cones using the locus of (x,t) points corresponding to $\mathcal{F}_{1,x}(t) = \mathcal{F}_{th}$, for various threshold values \mathcal{F}_{th} , for which $t \propto x$. We find that this ballistic feature is violated for too small or too large values of \mathcal{F}_{th} . We extract $v_B(\mathcal{F}_{th})$ from the resulting light cones and find that $v_B(\mathcal{F}_{th})$ converges approximately to the same value v_B over a wide range of \mathcal{F}_{th} , as shown in Fig. 5.3. We discuss the results for $v_B(S,T)$ obtained from the real p method below along with that from the imaginary p method.

Imaginary p method.— To calculate butterfly velocity through this method, we use the single-mode ansatz for OTOC and the results obtained by Gu and Kitaev⁶¹. Using the single mode ansatz⁷⁸ for early time OTOC, they proved a ladder identity which implies the existence of a pole and a saddle at two imaginary values of momentum that contribute to the growth of OTOC. We refer to Ref. 61 for the proof of the ladder identity and the details of the method. Using this ansatz we can write the solution of Eqs.(5.2) for the 1D SY chain model [Eq.(2.1)],

$$\mathcal{F}_{\mu,p}^a(t_1, t_2) \approx \frac{e^{\lambda_L(p)(t_1+t_2)/2}}{C(p)} \Upsilon_{\mu,p}^R(t_{12}) \Upsilon_{\mu,p}^A(0) \quad (5.5)$$

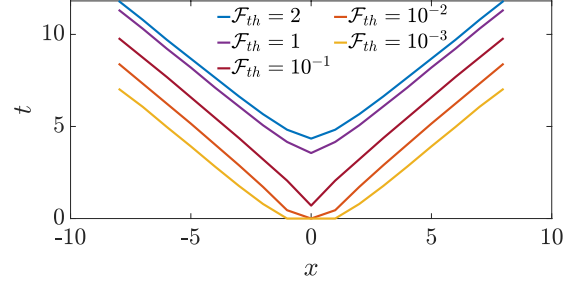


FIG. 5.3. Light cones at $T = 0.8$ and $S = 1.0$ for different values of \mathcal{F}_{th} obtained using the real p method. The same butterfly speed v_B is obtained for a wide range of \mathcal{F}_{th} .

where $\Upsilon_{\mu,p}^R(t)$ and $\Upsilon_{\mu,p}^A(t)$ are the retarded and advanced vertex functions⁶¹ which modify the OTOC by an overall magnitude. The dominant p dependence of the above comes from a pole $\lambda_L = 2\pi T$ ($k_B = 1$, $\hbar = 1$) in $C(p)$, since $C(p) \propto \cos[\lambda_L(p)/4T]$ ⁶¹. This pole leads to the maximal chaos for non-Fermi liquids in SYK and related models^{41,51,61}. The asymptotic form of Eq.(5.5) ignores the initial correlations and any non-linear effects^{61,78} and is valid only at the butterfly or chaos front, i.e., $1/N \ll \mathcal{F}_{\mu,p}(t_1, t_2)/N \ll 1$. Fourier transforming Eq.(5.5) back to real space, we obtain

$$\mathcal{F}_{\mu,x}(t) \equiv \mathcal{F}_{\mu,x}^a(t,t) \approx \int_{-\infty}^{\infty} \frac{dp}{2\pi} \frac{e^{\lambda_L(p)t+ipx}}{\cos(\lambda_L(p)/4T)} f(p), \quad (5.6)$$

where $f(p)$, which depends on the kernel [Eqs.(5.4)] and vertex functions in Eq.(5.5), is assumed to be analytical function of p and non vanishing in the momentum regime of interest⁶¹.

As in the real p method discussed above, we choose a fixed, albeit arbitrary, value of $\mathcal{F}_{\mu,x}(t,t) \approx 1$, which is at the lower end of the butterfly front⁶¹, to obtain the light cone from the resulting locus of (x,t) points and extract v_B . For large x and t , the integral in Eq.(5.6) can be estimated by saddle-point method. The saddle-point p_s for the integrand is obtained from $\lambda_L'(p_s)t + ix = 0$, where $\lambda_L'(p)$ is the derivative. This together with the condition $\mathcal{F}_{\mu,x}(t,t) \approx 1$, implying $\lambda_L(p)t + ipx = 0$, leads to the following equation for p_s

$$\lambda_L'(p_s) = \frac{\lambda_L(p_s)}{p_s}, \quad (5.7)$$

and a corresponding velocity

$$v_s = \left(\frac{x}{t} \right)_s = i\lambda_L'(p_s). \quad (5.8)$$

The saddle point leads to a contribution $\mathcal{F}_{\mu,x}^s(t) \sim \exp[\lambda_L(p_s)t + ip_s x]$. Similarly, the pole p_1 of the integrand in Eq.(5.6), such that $\lambda_L(p_1) = 2\pi T$, gives a contribution $\mathcal{F}_{\mu,x}^p(t) \sim \exp[2\pi T t + ip_1 x]$ with an associated velocity

$$v_m = i \frac{2\pi T}{p_1}. \quad (5.9)$$

To give rise to a well defined light cone, $\mathcal{F}_{\mu,x}^s(t)$ ($\mathcal{F}_{\mu,x}^p(t)$) should be non-oscillatory in space and time, implying that p_s (p_1) is purely imaginary, i.e., $p_s = i|p_s|$ ($p_1 = i|p_1|$), and $\lambda_L(i|p_s|)$ is purely real. In Appendix C, we show that this is indeed the case by solving for $\lambda_L(p)$ for purely imaginary $p = i|p|$ from Eqs.(5.2) using the exponential growth ansatz, as discussed earlier for the real p method. $\lambda_L(i|p|)$ is found to be a convex function of $|p|$ as expected⁶¹. The light cone and the associated v_B are determined by either the saddle-point or the pole contribution to $\mathcal{F}_{\mu,x}(t)$ depending on whether $|p_s| < |p_1|$ or $|p_s| > |p_1|$, respectively. The conditions also translate to $v_s (\equiv v(p_s)) < v_1 (\equiv v(p_1))$ or $v_s > v_1$, respectively, where the velocity $v(p) = i\lambda_L'(p)$, since $\lambda_L(i|p|)$ is a convex (up) function of p (Appendix C).

For the condition $|p_s| < |p_1|$, the deformed contour, that goes through the saddle point $i|p_s|$ on the imaginary axis in the evaluation of the integral in Eq.(5.6), does not enclose the pole and hence the latter does not contribute. As discussed in refs.51 and 61, this condition is realized when $\lambda_L(0) \ll 2\pi T$, i.e., when the chaos is far away from maximal. In this case $\mathcal{F}_{\mu,x}(t) \approx \mathcal{F}_{\mu,x}^s(t)$ and $v_B = v_s$. By making a small p approximation, $\lambda_L(p) \simeq \lambda_L(0) - \tilde{D}p^2$ (with $\tilde{D} > 0$), we obtain $v_B = v_s = [4\tilde{D}\lambda_L(0)]^{1/2}$ and

$$\mathcal{F}_{\mu,x}(t) \sim e^{\lambda_L(0)t(1-x^2/v_B^2 t^2)} \quad (5.10)$$

Here the quantity $\tilde{D} = v_B^2/4\lambda_L(0)$ has the dimension of diffusion constant. For certain holographic theories⁵⁸ and strongly interacting diffusive metals built from SYK-type quantum dots^{41,51}, $4\tilde{D}$ has been found to be exactly equal to energy diffusion constant at low temperature. \tilde{D} has also been found to be same as spin diffusion constant at high temperature in a classical spin liquid⁵⁵, and even for classical XY model⁵⁶. Assuming that such relation between \tilde{D} and actual diffusion constant hold, at least, over a limited range of (S, T) in the phased diagram of SY chain, we use \tilde{D} as a proxy for diffusion constant and plot it as a function of S and T below.

For the other condition $|p_s| > |p_1|$, realized for $\lambda_L(0) \approx 2\pi T$, the pole contributes and dominates over the saddle-point contribution, such that

$$\mathcal{F}_{\mu,x}(t) \approx \mathcal{F}_{\mu,x}^p(t) \sim e^{2\pi T t(1-|x|/v_B t)} \quad (5.11)$$

and $v_B = v_m$, as can be deduced from $\mathcal{F}_{\mu,x}(t) \approx 1$. The above corresponds to maximal chaos, realized for SYK-type non-Fermi liquids^{41,51,61}.

For most part of the phase diagram [Fig. 3.1] we have studied, we see that saddle point, $|p_s|$ remains well below the pole, $|p_1|$ and so the OTOC receives dominant

contribution from the saddle point. See Appendix C for more details. Therefore the chaos front travels with a speed $v_B = i\lambda_L'(i|p_s|)$ and the Lyapunov exponent λ_L is non-maximal, as was verified through direct calculation of $\lambda_L(S, T)$ in Sec. 4. The SY chain can be analytically shown to be maximally chaotic in the limit $S \rightarrow 0$, $T \rightarrow 0$ following the same methods^{3,6,8} used for calculating $\lambda_L(T)$ in the SYK model.

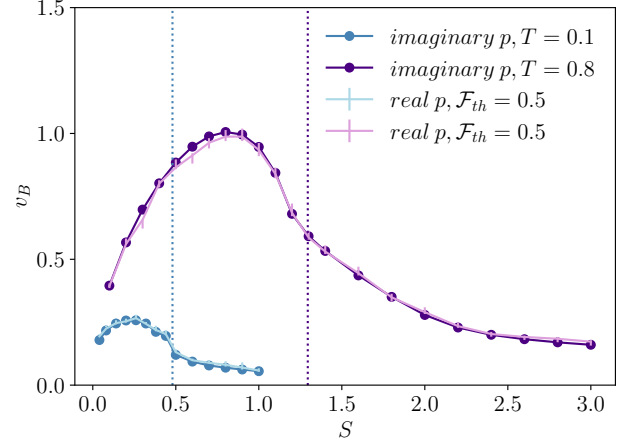


FIG. 5.4. **Variation of butterfly velocity with S in the SY model.** v_B across the SG phase transition (S_{SG} , vertical dashed lines) as a function of S at $T = 0.1, 0.8$ (in units of $\tilde{J} = 1$) and $\alpha = 0.25$, calculated using both real and imaginary p methods, as indicated in the legends. For the real p method, we have used $\mathcal{F}_{th} = 0.5$ with range (error bars) $\mathcal{F}_{th} = 0.1 - 1.0$, for a lattice of $L = 50$ sites.

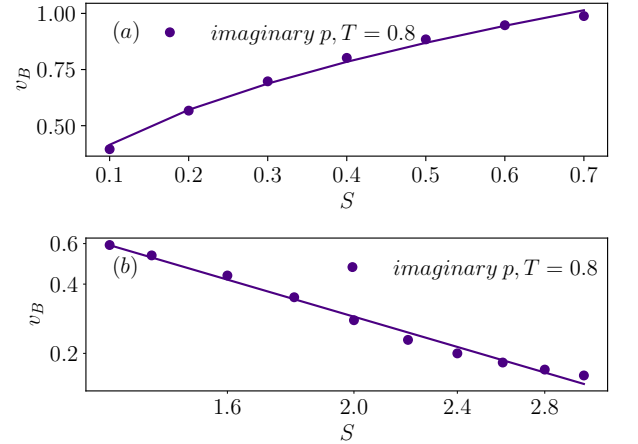


FIG. 5.5. **S dependence of v_B in the PM and SG phases of SY model.** (a) The data (circles) for $v_B(S, T)$ in the PM phase, before it reaches the maximum [Fig. 5.4], is fitted with $v_B(0, T) + aS^{\alpha_v}$ (line) for $T = 0.8$ with $\alpha_v \approx 0.46$. (b) Power law dependence of v_B on S in the SG phase is shown as straight line on a log-log plot. $v_B \sim 1/S^{1.7}$ for $T = 0.8$.

We calculate v_B as a function of T and S , across the SG-PM phase transition, for $S = 0.5, 1.0$ and $T = 0.1, 0.8$ along the a, b and d, e cuts, respectively, shown in Fig. 3.1, using both real and imaginary p methods. As discussed below, we find that the results from the two methods match closely, validating the particular form of single-mode ansatz in Eq.(5.5) even in the replica-symmetry broken spin glass phase.

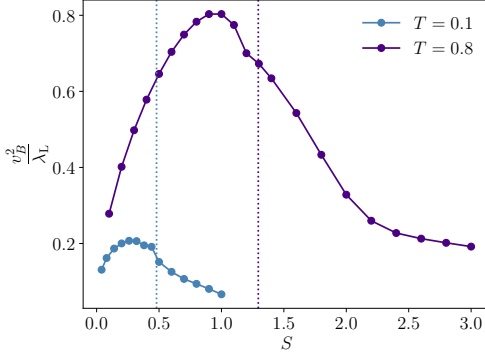


FIG. 5.6. $\tilde{D} \sim v_B^2/\lambda_L$ across the phase transition (S_{SG} , vertical dashed lines) as a function of S calculated for $T = 0.1$ and $T = 0.8$.

S dependence of butterfly velocity.— Fig. 5.4 shows v_B as a function of S for $T = 0.1$ and $T = 0.8$, going from spin liquid and spin liquid-local moment crossover region to the SG phase. As in the case of $\lambda_L(S)$ [Fig. 4.3], $v_B(S)$ exhibits a broad maximum in the PM phase.

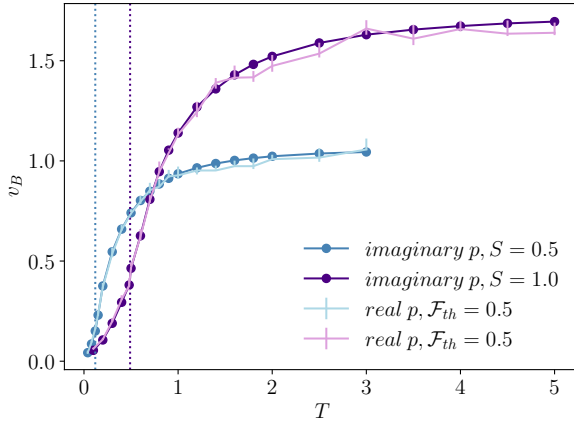


FIG. 5.7. **Temperature dependence of butterfly velocity in SY model.** v_B across the phase transition (T_{SG} , vertical dashed lines) as a function of temperature at $S = 0.5, 1.0$, $\alpha = 0.25$, using both real and imaginary p methods (see main text). The parameters and the conventions are same as those described in the caption of Fig. 5.4 .

We find v_B to have power-law dependence, $v_B(S, T) - v_B(0, T) \sim \sqrt{S}$ for small S , similar to λ_L [Fig. 4.4(a)] with $v_B(0, T) \approx 0$ in the limit $S \rightarrow 0$, as shown in Fig.

5.5(a) for $T = 0.8$. In the SG phase, v_B shows a power-law decay $v_B(S) \sim 1/S^{1.7}$, as shown in Fig. 5.5(b), reminiscent of power-law decay of $\lambda_L(S)$ [Fig. 4.4(b)]. We also plot the proxy for the diffusion constant $\tilde{D} \sim v_B^2/\lambda_L$ as a function of S in Fig. 5.6. Similar to λ_L and v_B , \tilde{D} exhibits a broad maximum in within the PM phase and decays with S in SG phase. From the knowledge of the behavior of $\lambda_L(S)$ and $v_B(S)$ we expect a similar power-law behavior of $\tilde{D}(S)$ in the PM and SG phase.

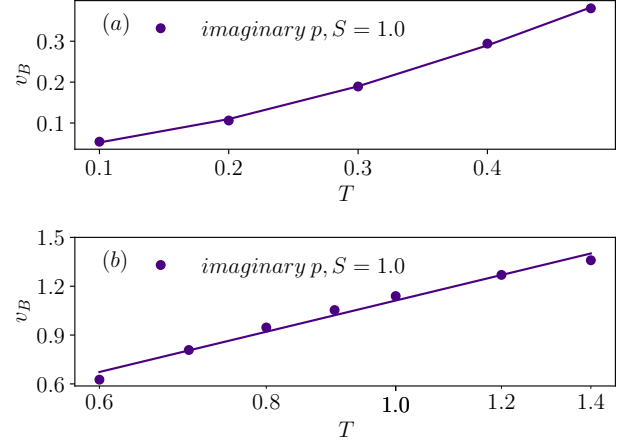


FIG. 5.8. **Temperature dependence of v_B in the SG and PM phases of SY model.** (a) $v_B(S, T)$ (circles) in the SG phase is fitted with $v_B(S, T) \simeq v_B(S, 0) + aT^{\beta_v}$ (line) for $S = 1.0$ where $v_B(S, 0) \simeq 0.03$ and $\beta_v \simeq 1.65$. (b) Logarithmic fit (line) to $v_B(T)$ in the PM phase, $v_B \sim a \ln T + c$ is shown on a semi-log plot (v_B vs. $\ln T$) for $S = 1.0$.

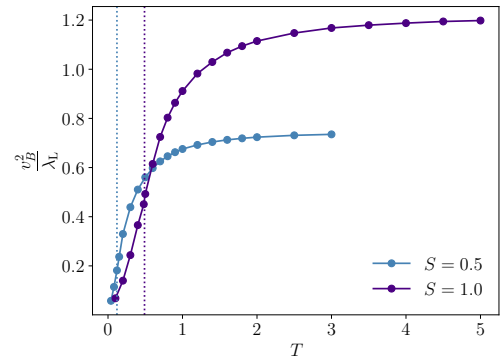


FIG. 5.9. $\tilde{D} \sim v_B^2/\lambda_L$ as a function of temperature for $S = 0.5$ and $S = 1.0$ in SY model. The SG transition temperatures are shown by vertical dashed lines.

Temperature dependence of butterfly velocity.— v_B is shown as a function of T for $S = 0.5, 1.0$ across the PM-SG transition. The butterfly velocity monotonically increases with temperature through T_{SG} , saturating at high temperature, similar to $\lambda_L(T)$ [Fig. 4.5]. As seen in Fig. 5.7, v_B approaches a value for $T \rightarrow 0$ in the SG

phase. As shown in Fig. 5.8(a), $v_B(T) - v_B(S, 0) \sim T^{1.65}$, i.e., v_B increases with temperature as a power law from the $T = 0$ value. Like the $\lambda_L(T)$ [Fig. 5.8(b)], the T dependence of v_B is logarithmic, $\sim a \ln T + c$, for $T \gtrsim T_{SG}$ in the PM phase [Fig. 5.8(b)]. The proxy diffusion constant $\tilde{D} \sim v_B^2/\lambda_L$ is plotted in Fig. 5.9. The behavior of $\tilde{D}(T)$ is similar to that of $\lambda_L(T)$ and $v_B(T)$, where it starts from small values, as one would expect, the slower transport in the SG phase and then grows monotonically across the phase transition and saturates to an S dependent value. The proxy diffusion constant $\tilde{D}(T)$ decreases with decreasing temperature as expected in a SG phase.

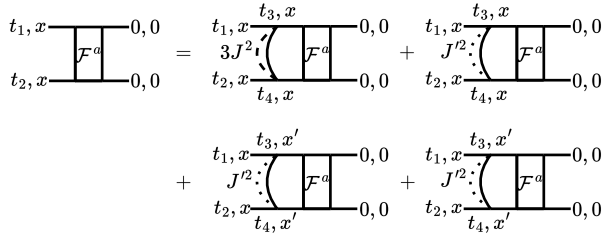


FIG. 5.10. Diagrammatic representation of the Kernel equation in Eq. 5.13 for $\mathcal{O}(1/N)$ term, \mathcal{F}_x^a in the OTOC $F_x^a(t_1, t_2)$. The solid horizontal lines denote dressed retarded and advanced propagators G_R, G_A and the vertical rung denotes the Wightmann correlation G_{lr} (Appendix B). The dashed and dotted lines denote disorder averaging over J and J^\pm couplings in Eq. (2.3). Here $x' = x \pm 1$.

B. Butterfly velocity across spin glass transition in the p -spin glass chain

To compute the $v_B(\Gamma, T)$ in the p -spin glass chain [Eq. (2.3)], we use methods similar to that for the SY chain discussed above. We calculate the following regularized OTOC defined as,

$$F_x(t_1, t_2) = \frac{1}{N^2} \sum_{i,j} \overline{\text{Tr} \left[y s_{i,x}(t_1) y s_{j,0}(0) y s_{i,x}(t_2) y s_{j,0}(0) \right]} \quad (5.12)$$

Following the calculations discussed earlier for the SY chain, the diagrams that contribute to the OTOC can be grouped in powers of $1/N$. The leading order $\mathcal{O}(1)$ diagrams are disconnected and do not contribute to the growth. At the next leading order $\mathcal{O}(1/N)$ we have “ladder” diagrams which contribute to the growth of OTOC in the scrambling regime, $\lambda_L^{-1} \lesssim t \lesssim \lambda_L^{-1} \ln N$. As earlier, these ladder diagrams can be written in the form of a Bethe-Salpeter equation shown in Fig. 5.10, i.e.

$$\mathcal{F}_x^a(t_1, t_2) = \int dx' \int dt_3 dt_4 K_{xx'}^a(t_1, t_2, t_3, t_4) \mathcal{F}_{x'}^a(t_3, t_4), \quad (5.13)$$

where the kernel is given by

$$K_{xx'}^a(t_1, t_2, t_3, t_4) = \left[(3J^2 + J'^2) \delta_{x',x} + 2J'^2 \delta_{x',x \pm 1} \right] G_R(t_{13}) G_R(t_{24}) G_W(t_{34}) \quad (5.14)$$

After Fourier transforming $\mathcal{F}_x^a(t_1, t_2)$ to momentum space, we obtain $\mathcal{F}_p^a(t_1, t_2)$ and the Kernel

$$K_p^a(t_1, t_2, t_3, t_4) = \tilde{J}^2 \left[3 - \frac{\alpha}{2} (5 - 4 \cos p) \right] \quad (5.15)$$

where we have used, $J^2 + 2J'^2 = \tilde{J}^2$ and $\alpha = 2J'^2/\tilde{J}^2$.

To calculate the butterfly velocity we again use the real and imaginary p methods discussed for the SY chain above [Sec. 5A]. In the imaginary p method, we employ the single mode ansatz

$$F_p^a(t_1, t_2) \approx \frac{e^{\lambda_L(p)(t_1+t_2)/2}}{C(p)} \Upsilon_p^R(t_{12}) \Upsilon_p^A(0) \quad (5.16)$$

We skip the details of the implementations of the two methods here, since they are similar to those for the SY chain. v_B is calculated across the spin glass phase transition line as a function of T and Γ .

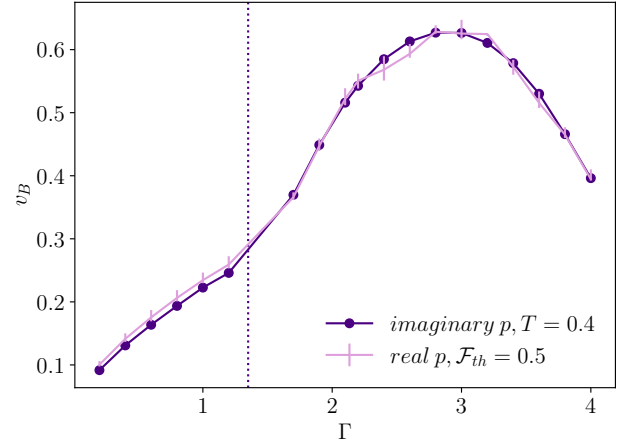


FIG. 5.11. Variation of butterfly velocity with quantum parameter Γ in the p -spin glass model. v_B across the p -spin glass phase transition as a function of Γ at $T = 0.4$, $\alpha = 0.25$. In the real p calculation v_B is calculated from the slope of light cone for $\mathcal{F}_{th} = 0.5$, for a lattice of $L = 50$ sites (see Sec. 5A). The error bars in the real p results indicate variation of v_B over a range of threshold values $\mathcal{F}_{th} = 0.1 - 1.0$.

Γ dependence of butterfly velocity.— Fig. 5.11 shows the butterfly velocity as a function of the quantum fluctuation parameter Γ for $T = 0.4$ (in units of $\tilde{J} = 1$) (y cut in Fig. 3.2). In the PM phase, v_B exhibits non-monotonic dependence on Γ with the broad maximum above the glass transition at $\Gamma = \Gamma_{SG}$, as in the case of $\lambda_L(\Gamma)$ [Fig. 4.8]. The butterfly velocity follows a power law, $v_B(\Gamma, T) - v_B(0, T) \sim \Gamma^{0.7}$, with the quantum fluctuation parameter Γ for small $\Gamma < \Gamma_{SG}$ with extrapolated

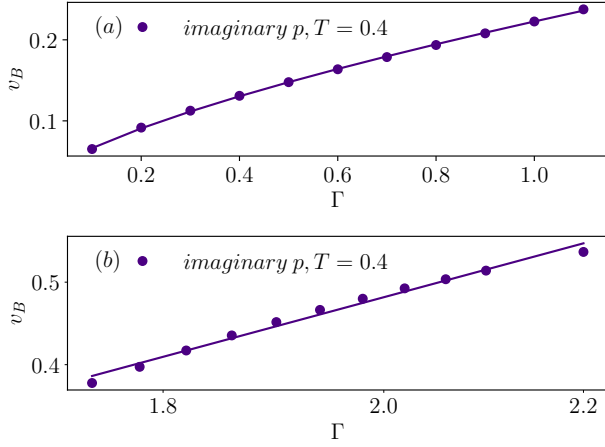


FIG. 5.12. Γ dependence of butterfly velocity in the SG and PM phases of p -spin glass model. $v_B(\Gamma, T)$ (circles) is fitted (a) in the SG phase with $v_B \simeq v_B(0, T) + a\Gamma^{\alpha_v}$ (line), where $\alpha_v \simeq 0.7$ and $v_B(0, T) \simeq 0.027$ for $T = 0.4$, and (b) in the PM phase with $v_B \sim \Gamma^{1.5}$ (line), shown on a log-log plot for $T = 0.4$.

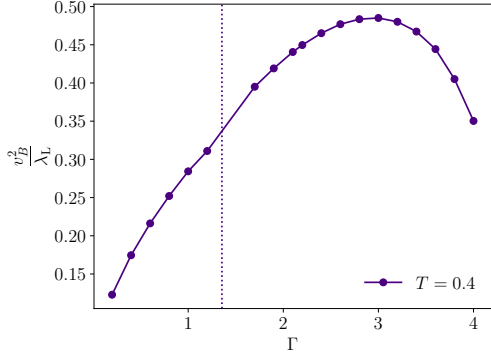


FIG. 5.13. $\tilde{D} \sim v_B^2/\lambda_L$ across the SG phase transition as a function of Γ calculated for $T = 0.4$

$v_B(0, T) \approx 0$ in the $\Gamma \rightarrow 0$ limit, deep in the SG phase [Fig. 5.12(a)]. v_B varies as $v_B \sim \Gamma^{1.5}$ with increasing Γ [Fig. 5.12(b)] in the PM phase close to the transition ($\Gamma \gtrsim \Gamma_{SG}$) before reaching the maximum, as shown in Fig. 5.11. We also plot the proxy for diffusion constant $\tilde{D} \sim v_B^2/\lambda_L$ in Fig. 5.13 for $T = 0.4$. In the SG phase, \tilde{D} is very small for small Γ , then increases monotonically across the phase transition and exhibits a peak above the transition Γ_{SG} in the PM phase.

Temperature dependence of butterfly velocity.— We demonstrate the overall temperature dependence of the butterfly velocity going from the SG to the PM phase through the transition at T_{SG} for $\Gamma = 2.0$ in Fig. 5.14. $v_B(T)$ exhibits a broad peak in the PM phase, just like $\lambda_L(T)$ in Fig. 4.9. Figs. 5.15(a),(b) show that the butterfly velocity follows $v_B(\Gamma, T) - v_B(\Gamma, 0) \sim T^{1.7}$, with a small extrapolated zero-temperature value $v_B(\Gamma, 0)$ in

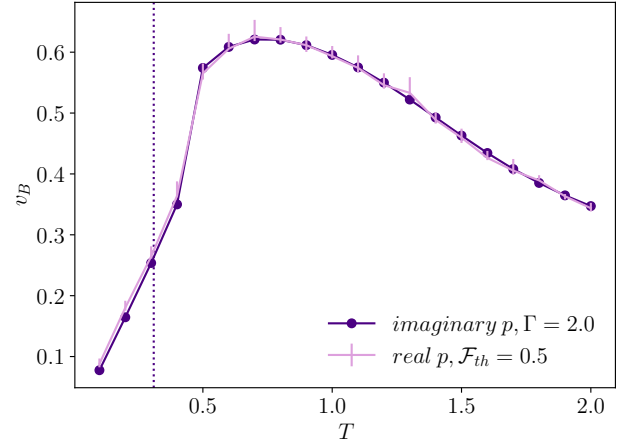


FIG. 5.14. Temperature dependence of butterfly velocity in p -spin model. v_B across the phase transition as a function of temperature at $\Gamma = 2.0$, $\alpha = 0.25$. The imaginary momentum calculation uses the single mode ansatz. In the real momentum calculation v_B is calculated from the edge of the light cone for values of $\mathcal{F}_{th} = 0.5$, in a lattice of $L = 50$ sites. Variation in v_B from nearby values of $\mathcal{F}_{th} = 0.1$ and $\mathcal{F}_{th} = 1.0$ is shown as error bar.

the SG phase, and logarithmic T dependence in the PM phase for $T \gtrsim T_{SG}$, as in the SY model [Fig. 5.8]. The variation of resultant $\tilde{D} \sim v_B^2/\lambda_L$ with temperature [Fig. 5.16] is also very similar to that of λ_L and v_B where it exhibits a broad peak in the PM phase.

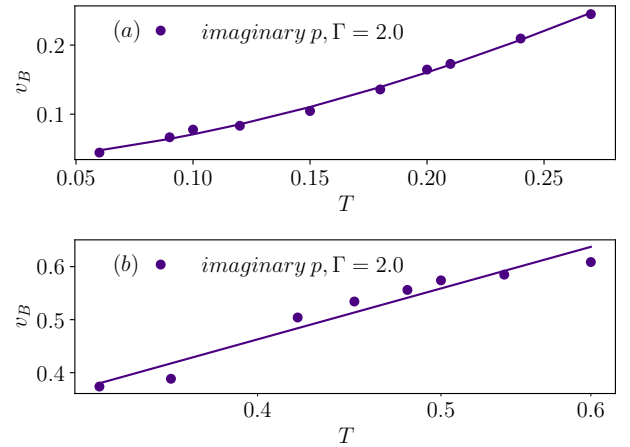


FIG. 5.15. Temperature dependence of v_B in PM and SG phases of p -spin glass model. (a) v_B vs. T (circles) in SG phase is fitted as $v_B \simeq v_B(\Gamma, 0) + aT^{\beta_v}$ (line) for $\Gamma = 2.0$, where $\beta_v \simeq 1.7$ and $v_B(\Gamma, 0) \simeq 0.03$. (b) Logarithmic dependence of v_B on T (circles) in PM phase, shown as a straight line fit on a semi-log plot for $\Gamma = 2.0$.

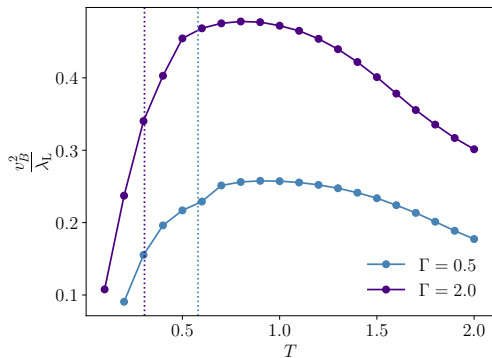


FIG. 5.16. $\tilde{D} \sim v_B^2/\lambda_L$ across the phase transition as a function of T calculated for $\Gamma = 2.0$. in p -spin glass model

6. DISCUSSION

In this work, we have studied how quantum and thermal fluctuations influence propagation of quantum information, as diagnosed by butterfly velocity, along with chaotic growth rate characterized by a Lyapunov exponent, through one-dimensional generalizations of two paradigmatic zero-dimensional quantum spin glass models, Sachdev-Ye and p -spin glass models. These lattice models allow us to map out variations of λ_L and v_B with temperature and quantum parameter deep inside the phases and near the non-trivial replica symmetry breaking spin glass transitions, as well as through crossovers between competing paramagnetic phases, e.g., spin liquid and local moment behaviors, and across the SG transition. We find distinct evolution of glassy complexity, indicated by maximum, or lack thereof, in the Lyapunov exponent and butterfly velocity in the PM phase, as a function of quantum and thermal fluctuations in the SY model. The maximum is seen only as a function of quantum parameter S , around the onset of two-step glassy relaxation, away from the glass transition from the PM side. The maximum is absent when the glass transition is approached by decreasing T . In contrast, the maximum occurs as function of both T and the quantum parameter Γ in the PM phase of p -spin glass. The maximum corresponds to intensified chaos due to maximal complexity arising from the sampling of exponentially large number of saddle points of the underlying glassy landscape. In the semiclassical limit, the maximal number of saddle points leads to extreme sensitivity to the initial condi-

tion³⁵ or chaos.

The spin glass models discussed here and other related models can be realized in cavity quantum electrodynamics (QED) platforms^{79–83}, and even scrambling dynamics can be probed in this setup^{84,85}. Our work needs to be extended in future in several directions. To better understand connection between glassy complexity^{35,37} and quantum many-body chaos, it will be worthwhile to compute the complexity for the SY model using both semiclassical methods³⁵ and quantum Thouless-Anderson-Palmer (TAP) equations⁸⁶, as have been done for quantum p -spin glass. As $\tilde{D} \sim v_B^2/\lambda_L$ often acts as a proxy to diffusion constant, it will be interesting to compare our predictions of \tilde{D} , from the asymptotic behavior of λ_L and v_B from chaos calculations with actual transport calculations in a chain of spin glass quantum dots.

Our real-frequency saddle-point calculations of λ_L and v_B , and corresponding bosonic spectral functions, in the SY model indicate subtle competition between spin liquid and local moment solutions, as well as strong S and T dependent corrections to the conformal solution for the SYK-like spin liquid maximal chaotic behavior, even at small values of $S \lesssim 0.05$ and low temperature $T \sim 0.1$. This implies intriguing crossover in the small S region towards the expected maximally chaotic SYK spin liquid for $S \rightarrow 0$. We have not studied this crossover and the relative stability and intricate competition between spin liquid and local moment solutions in the small S region in much detail in this work. It will be important to study the chaos and spectral properties in the small- S regime in future work. Finally, it will be an exciting research direction to compute entanglement properties in various crossover regions and across the replica symmetry breaking spin glass transition in these large N models following methods^{62,87} similar to those applied for calculating entanglement entropy in lattice of SYK dots and in Hubbard model within dynamical mean-field theory.

ACKNOWLEDGEMENTS

VL acknowledges support from CSIR, India and is grateful to the workstation provided by CHEP on which most of calculations in this work are done. SB acknowledges support from SERB (Grant No. CRG/2022/001062), DST, India, and QuST project of the DST, Govt. of India.

* venkatakumar@iisc.ac.in; surajit@iisc.ac.in; sumilan@iisc.ac.in

¹ Yasuhiro Sekino and L. Susskind, “Fast scramblers,” *Journal of High Energy Physics* **2008**, 065 (2008), [arXiv:0808.2096](https://arxiv.org/abs/0808.2096) [hep-th].

² Juan Maldacena, Stephen H. Shenker, and Douglas Stanford, “A bound on chaos,” *Journal of High Energy Physics* **2016**, 1–17 (2016).

³ A. Kitaev, “A simple model of quantum holography,” *Talks at KITP*, April 7, 2015 and May 27, 2015 .

- ⁴ Subhayan Sahu, Shenglong Xu, and Brian Swingle, “Scrambling dynamics across a thermalization-localization quantum phase transition,” *Phys. Rev. Lett.* **123**, 165902 (2019).
- ⁵ Kristan Jensen, “Chaos in ads_2 holography,” *Phys. Rev. Lett.* **117**, 111601 (2016).
- ⁶ Juan Maldacena and Douglas Stanford, “Remarks on the sachdev-ye-kitaev model,” *Phys. Rev. D* **94**, 106002 (2016).
- ⁷ Aavishkar A. Patel and Subir Sachdev, “Quantum chaos on a critical fermi surface,” *Proceedings of the National Academy of Sciences* **114**, 1844–1849 (2017), <https://www.pnas.org/doi/pdf/10.1073/pnas.1618185114>.
- ⁸ Sumilan Banerjee and Ehud Altman, “Solvable model for a dynamical quantum phase transition from fast to slow scrambling,” *Phys. Rev. B* **95**, 134302 (2017).
- ⁹ Debanjan Chowdhury, Antoine Georges, Olivier Parcollet, and Subir Sachdev, “Sachdev-ye-kitaev models and beyond: Window into non-fermi liquids,” *Rev. Mod. Phys.* **94**, 035004 (2022).
- ¹⁰ Mark Srednicki, “Chaos and quantum thermalization,” *Phys. Rev. E* **50**, 888–901 (1994).
- ¹¹ Chaitanya Murthy and Mark Srednicki, “Bounds on chaos from the eigenstate thermalization hypothesis,” *Phys. Rev. Lett.* **123**, 230606 (2019).
- ¹² Igor L. Aleiner, Lara Faoro, and Lev B. Ioffe, “Microscopic model of quantum butterfly effect: Out-of-time-order correlators and traveling combustion waves,” *Annals of Physics* **375**, 378–406 (2016).
- ¹³ Douglas Stanford, “Many-body chaos at weak coupling,” *Journal of High Energy Physics* **2016**, 9 (2016).
- ¹⁴ Efim B. Rozenbaum, Sriram Ganeshan, and Victor Galitski, “Lyapunov exponent and out-of-time-ordered correlator’s growth rate in a chaotic system,” *Phys. Rev. Lett.* **118**, 086801 (2017).
- ¹⁵ Thomas Scaffidi and Ehud Altman, “Chaos in a classical limit of the Sachdev-ye-Kitaev model,” *Phys. Rev. B* **100**, 155128 (2019).
- ¹⁶ Tianrui Xu, Thomas Scaffidi, and Xiangyu Cao, “Does scrambling equal chaos?” *Phys. Rev. Lett.* **124**, 140602 (2020).
- ¹⁷ W. Kob, “The Mode-Coupling Theory of the Glass Transition,” arXiv e-prints, cond-mat/9702073 (1997), [arXiv:cond-mat/9702073 \[cond-mat.stat-mech\]](https://arxiv.org/abs/cond-mat/9702073).
- ¹⁸ Pablo G. Debenedetti and Frank H. Stillinger, “Supercooled liquids and the glass transition,” *Nature* **410**, 259–267 (2001).
- ¹⁹ Ludovic Berthier and Giulio Biroli, “Theoretical perspective on the glass transition and amorphous materials,” *Rev. Mod. Phys.* **83**, 587–645 (2011).
- ²⁰ Stephan Büchner and Andreas Heuer, “Potential energy landscape of a model glass former: Thermodynamics, anharmonicity, and finite size effects,” *Phys. Rev. E* **60**, 6507–6518 (1999).
- ²¹ Srikanth Sastry, “The relationship between fragility, configurational entropy and the potential energy landscape of glass-forming liquids,” *Nature (London)* **409**, 164–167 (2001), [arXiv:cond-mat/0011317 \[cond-mat.stat-mech\]](https://arxiv.org/abs/cond-mat/0011317).
- ²² Francesco Sciortino, “Potential energy landscape description of supercooled liquids and glasses,” *Journal of Statistical Mechanics: Theory and Experiment* **2005**, P05015 (2005).
- ²³ K. Binder and A. P. Young, “Spin glasses: Experimental facts, theoretical concepts, and open questions,” *Rev. Mod. Phys.* **58**, 801–976 (1986).
- ²⁴ E. Vincent, “Ageing, rejuvenation and memory: The example of spin-glasses,” in *Ageing and the Glass Transition*, edited by Malte Henkel, Michel Pleimling, and Roland Sanctuary (Springer Berlin Heidelberg, Berlin, Heidelberg, 2007) pp. 7–60.
- ²⁵ Jennifer A. Hodgdon and Frank H. Stillinger, “Stokes-einstein violation in glass-forming liquids,” *Phys. Rev. E* **48**, 207–213 (1993).
- ²⁶ Smarajit Karmakar, Chandan Dasgupta, and Srikanth Sastry, “Analysis of dynamic heterogeneity in a glass former from the spatial correlations of mobility,” *Phys. Rev. Lett.* **105**, 015701 (2010).
- ²⁷ S. F. Edwards and P. W. Anderson, “Theory of spin glasses,” *Journal of Physics F Metal Physics* **5**, 965–974 (1975).
- ²⁸ Marc Mezard, Giorgio Parisi, and Miguel Angel Virasoro, *Spin Glass Theory and Beyond: AN Introduction to the Replica Method and its Applications* (1987).
- ²⁹ G. Parisi, “Infinite number of order parameters for spin-glasses,” *Phys. Rev. Lett.* **43**, 1754–1756 (1979).
- ³⁰ Tommaso Castellani and Andrea Cavagna, “Spin-glass theory for pedestrians,” *Journal of Statistical Mechanics: Theory and Experiment* **2005**, P05012 (2005).
- ³¹ Surajit Bera, K. Y. Venkata Lokesh, and Sumilan Banerjee, “Quantum-to-classical crossover in many-body chaos and scrambling from relaxation in a glass,” *Phys. Rev. Lett.* **128**, 115302 (2022).
- ³² Th. M. Nieuwenhuizen, “Exactly solvable model of a quantum spin glass,” *Phys. Rev. Lett.* **74**, 4289–4292 (1995).
- ³³ Theo M. Nieuwenhuizen and Felix Ritort, “Quantum phase transition in spin glasses with multi-spin interactions,” *Physica A Statistical Mechanics and its Applications* **250**, 8–45 (1998), [arXiv:cond-mat/9706244 \[cond-mat.dis-nn\]](https://arxiv.org/abs/cond-mat/9706244).
- ³⁴ Leticia F. Cugliandolo, Daniel R. Grempel, and Constantino A. da Silva Santos, “From second to first order transitions in a disordered quantum magnet,” *Phys. Rev. Lett.* **85**, 2589–2592 (2000).
- ³⁵ Lorenzo Correale, Anatoli Polkovnikov, Marco Schirò, and Alessandro Silva, “Probing chaos in the spherical p-spin glass model,” arXiv e-prints, [arXiv:2303.15393 \(2023\)](https://arxiv.org/abs/2303.15393), [arXiv:2303.15393 \[cond-mat.dis-nn\]](https://arxiv.org/abs/2303.15393).
- ³⁶ Antonio Auffinger and Gerard Ben Arous, “Complexity of random smooth functions on the high-dimensional sphere,” arXiv e-prints, [arXiv:1110.5872 \(2011\)](https://arxiv.org/abs/1110.5872), [arXiv:1110.5872 \[math.PR\]](https://arxiv.org/abs/1110.5872).
- ³⁷ Tarek Anous and Felix M Haehl, “The quantum p-spin glass model: a user manual for holographers,” *Journal of Statistical Mechanics: Theory and Experiment* **2021**, 113101 (2021).
- ³⁸ Subir Sachdev and Jinwu Ye, “Gapless spin-fluid ground state in a random quantum heisenberg magnet,” *Phys. Rev. Lett.* **70**, 3339–3342 (1993).
- ³⁹ Antoine Georges, Olivier Parcollet, and Subir Sachdev, “Mean field theory of a quantum heisenberg spin glass,” *Phys. Rev. Lett.* **85**, 840–843 (2000).
- ⁴⁰ A. Georges, O. Parcollet, and S. Sachdev, “Quantum fluctuations of a nearly critical heisenberg spin glass,” *Phys. Rev. B* **63**, 134406 (2001).
- ⁴¹ Yingfei Gu, Xiao-Liang Qi, and Douglas Stanford, “Local criticality, diffusion and chaos in generalized sachdev-ye-kitaev models,” *Journal of High Energy Physics* **2017**, 125 (2017).
- ⁴² Subir Sachdev, “Bekenstein-hawking entropy and strange metals,” *Phys. Rev. X* **5**, 041025 (2015).

- ⁴³ Xue-Yang Song, Chao-Ming Jian, and Leon Balents, “Strongly correlated metal built from sachdev-ye-kitaev models,” *Phys. Rev. Lett.* **119**, 216601 (2017).
- ⁴⁴ Richard A. Davison, Wenbo Fu, Antoine Georges, Yingfei Gu, Kristan Jensen, and Subir Sachdev, “Thermoelectric transport in disordered metals without quasiparticles: The sachdev-ye-kitaev models and holography,” *Phys. Rev. B* **95**, 155131 (2017).
- ⁴⁵ Chao-Ming Jian, Zhen Bi, and Cenke Xu, “Model for continuous thermal metal to insulator transition,” *Phys. Rev. B* **96**, 115122 (2017).
- ⁴⁶ Shao-Kai Jian and Hong Yao, “Solvable sachdev-ye-kitaev models in higher dimensions: From diffusion to many-body localization,” *Phys. Rev. Lett.* **119**, 206602 (2017).
- ⁴⁷ Micha Berkooz, Prithvi Narayan, Moshe Rozali, and Joan Simón, “Higher dimensional generalizations of the SYK model,” *Journal of High Energy Physics* **2017**, 138 (2017), [arXiv:1610.02422 \[hep-th\]](https://arxiv.org/abs/1610.02422).
- ⁴⁸ Pengfei Zhang, “Dispersive sachdev-ye-kitaev model: Band structure and quantum chaos,” *Phys. Rev. B* **96**, 205138 (2017).
- ⁴⁹ Debanjan Chowdhury, Yochai Werman, Erez Berg, and T. Senthil, “Translationally invariant non-fermi-liquid metals with critical fermi surfaces: Solvable models,” *Phys. Rev. X* **8**, 031024 (2018).
- ⁵⁰ Arijit Haldar, Sumilan Banerjee, and Vijay B. Shenoy, “Higher-dimensional sachdev-ye-kitaev non-fermi liquids at lifshitz transitions,” *Phys. Rev. B* **97**, 241106 (2018).
- ⁵¹ Haoyu Guo, Yingfei Gu, and Subir Sachdev, “Transport and chaos in lattice sachdev-ye-kitaev models,” *Phys. Rev. B* **100**, 045140 (2019).
- ⁵² Debanjan Chowdhury and Brian Swingle, “Onset of many-body chaos in the $o(n)$ model,” *Phys. Rev. D* **96**, 065005 (2017).
- ⁵³ Subhayan Sahu and Brian Swingle, “Information scrambling at finite temperature in local quantum systems,” *Phys. Rev. B* **102**, 184303 (2020).
- ⁵⁴ Aavishkar A. Patel, Debanjan Chowdhury, Subir Sachdev, and Brian Swingle, “Quantum butterfly effect in weakly interacting diffusive metals,” *Phys. Rev. X* **7**, 031047 (2017).
- ⁵⁵ Thomas Bilitewski, Subhro Bhattacharjee, and Roderich Moessner, “Temperature dependence of the butterfly effect in a classical many-body system,” *Phys. Rev. Lett.* **121**, 250602 (2018).
- ⁵⁶ Sibaram Ruidas and Sumilan Banerjee, “Many-body chaos and anomalous diffusion across thermal phase transitions in two dimensions,” *SciPost Physics* **11**, 087 (2021), [arXiv:2007.12708 \[cond-mat.stat-mech\]](https://arxiv.org/abs/2007.12708).
- ⁵⁷ Thomas Bilitewski, Subhro Bhattacharjee, and Roderich Moessner, “Classical many-body chaos with and without quasiparticles,” *Phys. Rev. B* **103**, 174302 (2021).
- ⁵⁸ Mike Blake, “Universal diffusion in incoherent black holes,” *Phys. Rev. D* **94**, 086014 (2016).
- ⁵⁹ Brian Swingle and Debanjan Chowdhury, “Slow scrambling in disordered quantum systems,” *Phys. Rev. B* **95**, 060201 (2017).
- ⁶⁰ Bo-Bo Wei, Gaoyong Sun, and Myung-Joong Hwang, “Dynamical scaling laws of out-of-time-ordered correlators,” *Phys. Rev. B* **100**, 195107 (2019).
- ⁶¹ Yingfei Gu and Alexei Kitaev, “On the relation between the magnitude and exponent of OTOCs,” *JHEP* **02**, 075 (2019), [arXiv:1812.00120 \[hep-th\]](https://arxiv.org/abs/1812.00120).
- ⁶² Surajit Bera, Arijit Haldar, and Sumilan Banerjee, “Dynamical mean-field theory for Rényi entanglement entropy and mutual Information in Hubbard Model,” [arXiv e-prints](https://arxiv.org/abs/2302.10940), [arXiv:2302.10940 \(2023\)](https://arxiv.org/abs/2302.10940), [arXiv:2302.10940 \[cond-mat.str-el\]](https://arxiv.org/abs/2302.10940).
- ⁶³ Jaewon Kim, Xiangyu Cao, and Ehud Altman, “Scrambling versus relaxation in fermi and non-fermi liquids,” *Phys. Rev. B* **102**, 085134 (2020).
- ⁶⁴ Giulio Biroli and Olivier Parcollet, “Out-of-equilibrium dynamics of a quantum heisenberg spin glass,” *Phys. Rev. B* **65**, 094414 (2002).
- ⁶⁵ D. R. Grempel and M. J. Rozenberg, “Fluctuations in a quantum random heisenberg paramagnet,” *Phys. Rev. Lett.* **80**, 389–392 (1998).
- ⁶⁶ Leticia F. Cugliandolo, D. R. Grempel, and Constantino A. da Silva Santos, “Imaginary-time replica formalism study of a quantum spherical p-spin-glass model,” *Phys. Rev. B* **64**, 014403 (2001).
- ⁶⁷ W. Götze, *Complex Dynamics of Glass-Forming Liquids* (Oxford University Press, Oxford, 2008).
- ⁶⁸ David R. Reichman and Patrick Charbonneau, “Mode-coupling theory,” *Journal of Statistical Mechanics: Theory and Experiment* **2005**, 05013 (2005), [arXiv:cond-mat/0511407 \[cond-mat.soft\]](https://arxiv.org/abs/cond-mat/0511407).
- ⁶⁹ Alberto Camjayi and Marcelo J. Rozenberg, “Quantum and thermal fluctuations in the $su(n)$ heisenberg spin-glass model near the quantum critical point,” *Phys. Rev. Lett.* **90**, 217202 (2003).
- ⁷⁰ Maine Christos, Felix M. Haehl, and Subir Sachdev, “Spin liquid to spin glass crossover in the random quantum heisenberg magnet,” *Phys. Rev. B* **105**, 085120 (2022).
- ⁷¹ Liliana Arrachea and Marcelo J. Rozenberg, “Infinite-range quantum random heisenberg magnet,” *Phys. Rev. B* **65**, 224430 (2002).
- ⁷² Leticia F. Cugliandolo and Gustavo Lozano, “Real-time nonequilibrium dynamics of quantum glassy systems,” *Phys. Rev. B* **59**, 915–942 (1999).
- ⁷³ Yingfei Gu, Alexei Kitaev, Subir Sachdev, and Grigory Tarnopolsky, “Notes on the complex Sachdev-Ye-Kitaev model,” *JHEP* **02**, 157 (2020), [arXiv:1910.14099 \[hep-th\]](https://arxiv.org/abs/1910.14099).
- ⁷⁴ Jorge Kurchan, “Quantum bound to chaos and the semiclassical limit,” *Journal of Statistical Physics* **171**, 965–979 (2018).
- ⁷⁵ Vedika Khemani, David A. Huse, and Adam Nahum, “Velocity-dependent lyapunov exponents in many-body quantum, semiclassical, and classical chaos,” *Phys. Rev. B* **98**, 144304 (2018).
- ⁷⁶ Daniel A. Roberts and Brian Swingle, “Lieb-robinson bound and the butterfly effect in quantum field theories,” *Phys. Rev. Lett.* **117**, 091602 (2016).
- ⁷⁷ Elliott H. Lieb and Derek W. Robinson, “The finite group velocity of quantum spin systems,” *Communications in Mathematical Physics* **28**, 251–257 (1972).
- ⁷⁸ Alexei Kitaev and S. Josephine Suh, “The soft mode in the Sachdev-Ye-Kitaev model and its gravity dual,” *JHEP* **05**, 183 (2018), [arXiv:1711.08467 \[hep-th\]](https://arxiv.org/abs/1711.08467).
- ⁷⁹ Sarang Gopalakrishnan, Benjamin L. Lev, and Paul M. Goldbart, “Frustration and glassiness in spin models with cavity-mediated interactions,” *Phys. Rev. Lett.* **107**, 277201 (2011).
- ⁸⁰ Philipp Strack and Subir Sachdev, “Dicke quantum spin glass of atoms and photons,” *Phys. Rev. Lett.* **107**, 277202 (2011).
- ⁸¹ Yudan Guo, Ronen M. Kroeze, Varun D. Vaidya, Jonathan Keeling, and Benjamin L. Lev, “Sign-changing photon-mediated atom interactions in multimode cavity quantum

- electrodynamics,” *Phys. Rev. Lett.* **122**, 193601 (2019).
- ⁸² Hossein Hosseinabadi, Darrick E. Chang, and Jamir Marino, “Dynamics of spin glass formation under tunable fluctuations in frustrated cavity QED experiments,” *arXiv e-prints*, arXiv:2311.05682 (2023), arXiv:2311.05682 [cond-mat.dis-nn].
- ⁸³ Hossein Hosseinabadi, Darrick E. Chang, and Jamir Marino, “Nonequilibrium Dyson equations for strongly coupled light and matter: spin glass formation in multi-mode cavity QED,” *arXiv e-prints*, arXiv:2312.11624 (2023), arXiv:2312.11624 [cond-mat.dis-nn].
- ⁸⁴ Brian Swingle, Gregory Bentsen, Monika Schleier-Smith, and Patrick Hayden, “Measuring the scrambling of quantum information,” *Phys. Rev. A* **94**, 040302 (2016).
- ⁸⁵ J. Marino and A. M. Rey, “Cavity-qed simulator of slow and fast scrambling,” *Phys. Rev. A* **99**, 051803 (2019).
- ⁸⁶ Giulio Biroli and Leticia F. Cugliandolo, “Quantum thoulless-anderson-palmer equations for glassy systems,” *Phys. Rev. B* **64**, 014206 (2001).
- ⁸⁷ Arijit Haldar, Surajit Bera, and Sumilan Banerjee, “Rényi entanglement entropy of fermi and non-fermi liquids: Sachdev-ye-kitaev model and dynamical mean field theories,” *Phys. Rev. Res.* **2**, 033505 (2020).
- ⁸⁸ Olivier Parcollet, Antoine Georges, Gabriel Kotliar, and Anirvan Sengupta, “Overscreened multichannel SU(n) kondo model: Large- n solution and conformal field theory,” *Phys. Rev. B* **58**, 3794–3813 (1998).

Appendix A: Imaginary-time path integral and saddle-point equations for SY chain

We write the partition function $\mathcal{Z}(\{J_{ij,x}, J'_{ij,x}\}) = \text{Tr}[\exp(-\beta\mathcal{H})]$ ($\beta = 1/T$) of the disordered model of Eq.(2.1) as an imaginary-time path integral using the bosonic representation $S_{i\alpha\beta,x} = b_{i\alpha,x}^\dagger b_{i\beta,x} - S\delta_{\alpha\beta}$ with the constraint $\sum_{\alpha} b_{i\alpha,x}^\dagger b_{i\alpha,x} = SM$ ($S \geq 0$) on the number of bosons at each i, x , to fix the spin of the bosonic representation to S . Here the (real) random couplings $\{J_{ij,x}, J'_{ij,x}\}$ are drawn from Gaussian distributions with zero mean and variances J^2 and J'^2 , respectively. We calculate disorder-averaged quantities by introducing replicas $a = 1, \dots, n$ to obtain $\overline{\mathcal{Z}^n} = \int \mathcal{D}(\bar{b}, b) \mathcal{D}\lambda \exp[-S_{\text{eff}}]$, where

$$\begin{aligned}
S_{\text{eff}} = & \int_0^\beta d\tau \sum_{ix} [\bar{b}_{i\alpha,x}^a \partial_\tau b_{i\alpha,x}^a - \lambda_{i,x}^a(\tau) (\bar{b}_{i\alpha,x}^a b_{i\alpha,x}^a - SM)] \\
& - \frac{1}{2MN} \int_0^\beta d\tau d\tau' \left[\frac{J^2}{2} \sum_{i<j,x} S_{i\alpha\beta,x}^a(\tau) S_{i\gamma\delta,x}^b(\tau') S_{j\beta\alpha,x}^a(\tau) \right. \\
& S_{j\delta\gamma,x}^b(\tau') + J'^2 \sum_{i,j,x} S_{i\alpha\beta,x}^a(\tau) S_{i\gamma\delta,x}^b(\tau') S_{j\beta\alpha,x+1}^a(\tau) \\
& \left. S_{j\delta\gamma,x+1}^b(\tau') \right] \quad (\text{A.1})
\end{aligned}$$

Here the field $\lambda_{i,x}^a(\tau)$ imposes the constraint on boson number and sum over repeated α, β, \dots and a, b indices are assumed. In the $N \rightarrow \infty$ limit, introducing the Hubbard-Stratonovich field $Q_{\alpha\beta\gamma\delta,x}^{ab}(\tau, \tau')$, and its conjugate $\Pi_{\alpha\beta\gamma\delta,x}^{ab}(\tau, \tau')$ to impose $Q_{\alpha\beta\gamma\delta,x}^{ab}(\tau, \tau') = (1/N) \sum_i \langle S_{i\alpha\beta,x}^a(\tau) S_{i\gamma\delta,x}^b(\tau') \rangle$, we decouple the quartic terms above. Moreover, assuming SU(M) symmetry, i.e., $Q_{\alpha\beta\gamma\delta,x}^{ab}(\tau, \tau') = Q_x^{ab}(\tau, \tau') \delta_{\alpha\gamma} \delta_{\beta\delta}$, and similarly for Π , we obtain $\overline{\mathcal{Z}^n} = \int \mathcal{D}Q \mathcal{D}\Pi \mathcal{D}(\bar{b}, b) \mathcal{D}\lambda \exp[-S_{\text{eff}}]$ and the action

$$\begin{aligned}
S_{\text{eff}} = & \int_0^\beta d\tau \sum_x \left[\sum_i [\bar{b}_{i\alpha,x}^a \partial_\tau b_{i\alpha,x}^a - \lambda_{i,x}^a(\tau) (\bar{b}_{i\alpha,x}^a b_{i\alpha,x}^a - SM)] \right. \\
& + MN \int_0^\beta d\tau d\tau' \Pi_x^{ab}(\tau', \tau) [Q_x^{ab}(\tau, \tau') \\
& - \frac{1}{NM^2} \sum_i \bar{b}_{i\alpha,x}^a(\tau) b_{i\alpha,x}^b(\tau') b_{i\beta,x}^a(\tau) \bar{b}_{i\beta,x}^b(\tau')] \\
& - MN \int_0^\beta d\tau d\tau' Q_x^{ab}(\tau, \tau') \left(\frac{J^2}{4} Q_x^{ab}(\tau, \tau') \right. \\
& \left. + \frac{J'^2}{2} Q_{x+1}^{ab}(\tau, \tau') \right) \left. \right] \quad (\text{A.2})
\end{aligned}$$

Introducing $G_x^{ab}(\tau, \tau') = -(1/M) \sum_{\alpha} \langle b_{i\alpha,x}^a(\tau) \bar{b}_{i\alpha,x}^b(\tau') \rangle$ and the conjugate field $\Sigma_x^{ab}(\tau, \tau')$ we get $\overline{\mathcal{Z}^n} = \int \mathcal{D}(Q, \Pi, G, \Sigma, \lambda) \exp[-MN S_{\text{eff}}]$ with

$$\begin{aligned}
S_{\text{eff}} = & \sum_x \left[\text{Tr} \ln [(\partial_\tau - \lambda_x^a(\tau))\delta_{ab}\delta(\tau - \tau') + \Sigma_x^{ab}(\tau, \tau')] \right. \\
& - \int_0^\beta d\tau d\tau' Q_x^{ab}(\tau, \tau') \left(\frac{J^2}{4} Q_x^{ab}(\tau, \tau') + \frac{J'^2}{2} Q_{x+1}^{ab}(\tau, \tau') \right) \\
& + \int_0^\beta d\tau d\tau' \Pi_x^{ab}(\tau', \tau) (Q_x^{ab}(\tau, \tau') - G_x^{ab}(\tau, \tau') G_x^{ba}(\tau', \tau)) \\
& \left. + \int_0^\beta d\tau d\tau' \Sigma_x^{ab}(\tau, \tau') G_x^{ba}(\tau', \tau) + S \sum_a \int_0^\beta d\tau \lambda_x^a(\tau) \right] \quad (\text{A.3})
\end{aligned}$$

where we have imposed $\lambda_{ix}^a(\tau) = \lambda_x^a(\tau)$. In the large N, M limit, minimization of the above action with respect to Q, Π, G, Σ and λ , with the assumption of a time-translation invariant (equilibrium) saddle point, e.g., $Q_x^{ab}(\tau, \tau') = Q_x^{ab}(\tau - \tau')$ and $\lambda_x^a(\tau) = \lambda_x^a$, leads to the following self-consistency equations for the bosonic Green's function

$$\begin{aligned}
[G_x^{-1}]^{ab}(i\omega_k) &= (i\omega_k + \lambda_x^a)\delta^{ab} - \Sigma_x^{ab}(i\omega_k) \\
\Sigma_x^{ab}(\tau) &= J^2 G_x^{ab}(\tau) G_x^{ab}(\tau) G_x^{ab}(-\tau) \\
&+ J'^2 G_x^{ab}(\tau) (G_{x+1}^{ab}(\tau) G_{x+1}^{ab}(-\tau) \\
&+ G_{x-1}^{ab}(\tau) G_{x-1}^{ab}(-\tau)) \\
G_x^{aa}(\tau = 0^-) &= -S. \quad (\text{A.4})
\end{aligned}$$

Here $\omega_k = 2k\pi\beta$ is the bosonic Matsubara frequency with integer k . Assuming lattice translation invariance, $G_x^{ab}(\tau) = G^{ab}(\tau)$ and $\lambda_x^a = \lambda^a$, the above saddle point is the same as that [Eq.(3.1)] for the zero-dimensional model^{38,39} with the renormalized coupling $\tilde{J}^2 = J^2 + 2J'^2$.

Saddle point equation in PM phase— In the PM phase the Green's function is replica diagonal and symmetric. Thus, the saddle point equations in Eq.(3.1), after analytic continuation to real frequency, i.e., $i\omega_k \rightarrow \omega + i0^+$, becomes

$$[G_R(\omega)]^{-1} = \omega - \lambda - \Sigma_R(\omega) \quad (\text{A.5a})$$

$$\begin{aligned}
\Sigma(i\omega_k) &= \int_0^\beta d\tau e^{i\omega_k t} \Sigma(\tau) = \frac{\tilde{J}^2}{\beta^2} \sum_{k_1, k_2} G(i\omega_{k_1}) G(i\omega_{k_2}) \\
&G(i\omega_{k_1} + i\omega_{k_2} - i\omega_k) \quad (\text{A.5b})
\end{aligned}$$

Using the spectral representation $G(i\omega_k) = \int d\omega \rho(\omega)/(i\omega_k - \omega)$ with $\rho(\omega) = -(1/\pi)\text{Im} G_R(\omega)$ in Eq.A.5b gives,

$$\begin{aligned}
\Sigma(i\omega_k) &= \tilde{J}^2 \int d\omega_1 d\omega_2 d\omega_3 \frac{\rho(\omega_1)\rho(\omega_2)\rho(\omega_3)}{i\omega_k - \omega_1 - \omega_2 + \omega_3} \\
&[n_B(\omega_1)n_B(\omega_2)n_B(-\omega_3) + n_B(-\omega_1)n_B(-\omega_2)n_B(\omega_3)], \quad (\text{A.6})
\end{aligned}$$

where $\lambda^a = \lambda$ and $n_B(\omega) = 1/(e^{\beta\omega} - 1)$.

Using the identity $1/(\omega - \omega_1 - \omega_2 + \omega_3 + i0^+) = -i \int_0^\infty dt e^{i(\omega - \omega_1 - \omega_2 + \omega_3 + i0^+)t}$ and analytic continuation gives the retarded self-energy

$$\begin{aligned}
\Sigma_R(\omega) &= -i\tilde{J}^2 \int_0^\infty dt e^{i\omega t} [n_1(t)n_1(t)n_2(t) \\
&+ n_3(t)n_3(t)n_4(t)] \quad (\text{A.7})
\end{aligned}$$

where $n_1(t) = \int d\omega e^{-i\omega t} \rho(\omega) n_B(-\omega)$, $n_2(t) = \int d\omega e^{i\omega t} \rho(\omega) n_B(\omega)$, $n_3(t) = \int d\omega e^{-i\omega t} \rho(\omega) n_B(\omega)$, and $n_4(t) = \int d\omega e^{i\omega t} \rho(\omega) n_B(-\omega)$.

Saddle point equation in SG phase— Using the 1-RSB ansatz in Eq. 3.5, the analytically continued saddle point equation for the regular part of the green's function is given by

$$\begin{aligned}
[G_R(\omega)]^{-1} &= \omega - \frac{\tilde{J}g}{\Theta_R} - [\Sigma_R(\omega) - \Sigma_R(\omega = 0)], \\
m\beta &= \frac{1}{\tilde{J}g^2} \left(\frac{1}{\Theta_R} - \Theta_R \right) \quad (\text{A.8})
\end{aligned}$$

Using the similar steps for analytic continuation as in the PM phase, we get the retarded self-energy from Eq.(3.8b),

$$\begin{aligned}
\Sigma_R(\omega) &= -i\tilde{J}^2 \int_0^\infty dt e^{i\omega t} \left[(n_1^2(t)n_2(t) + n_3^2(t)n_4(t)) \right. \\
&- 2g(n_1(t)n_2(t) - n_3(t)n_4(t)) - g(n_3^2(t) - n_1^2(t)) \left. \right] \\
&+ 2g^2 \tilde{J}^2 G_R(\omega) + g^2 \tilde{J}^2 G_R^*(-\omega) \quad (\text{A.9})
\end{aligned}$$

where n_i , $i = 1, 2, 3, 4$ are same as those defined in the PM phase. The two equations above can be solved numerically similar to PM phase calculation, to obtain the retarded Green's function, $G_R(\omega)$.

1. Numerical solution of the saddle point equations

Here we provide the details of the numerical implementation of the self-consistent equations in imaginary as well as in real frequency.

a. Real-frequency solution

PM phase – The retarded Green function in PM phase can be obtained in the frequency domain by self-consistently solving Eq. 3.4. We write the self-energy $\Sigma_R(\omega)$ in a form convenient for numerical calculation using FFT, as in Eq.A.7. We start with an initial ansatz for $G_R(\omega)$ on a discrete range $\omega \in [-\omega_{max}, \omega_{max}]$ and an initial value of λ and calculate $\Sigma_R(\omega)$ from it. At each iteration, $[G_R(\omega)]^{-1}$ is updated as,

$$G_{R,j+1}^{-1}(\omega) = (1 - y) \left(\omega - \lambda - \Sigma_{R,j}(\omega) \right) + y G_{R,j}^{-1}(\omega) \quad (\text{A.10})$$

where $y \in (0,1)$ is used to ensure smooth convergence, which we choose typically between 0.2 and 0.3. At each iteration, we monitor the error $|[G_{R,j+1}(\omega)]^{-1} - [G_{R,j}(\omega)]^{-1}|$ and repeat the iteration with the updated $[G_{R,j+1}(\omega)]^{-1}$ until it converges. We then check the constraint, $G(\tau = 0^-) = -\int_{-\infty}^{\infty} d\omega \rho(\omega)/(e^{\beta\omega} - 1) = -S$. If it's not met, we repeat the procedure with a different λ . The procedure is repeated until the constraint is met.

SG phase – The retarded Green function, $G_R(\omega)$ in the SG phase can be obtained by solving Eq. 3A2. Similar to PM phase, the retarded self-energy $\Sigma_R(\omega)$ is written in a form suitable for implementation using FFT, as in Eq. (A.9). Starting with an initial ansatz and an initial value of m , we calculate $\Sigma_R(\omega)$. $G_R(\omega)$ is updated at each iteration as

$$G_{R,j+1}^{-1}(\omega) = (1-y) \left(\omega - \frac{\tilde{J}g}{\Theta_R} - [\Sigma_{R,j}(\omega) - \Sigma_{R,j}(\omega = 0)] \right) + y G_{R,j}^{-1}(\omega) \quad (\text{A.11})$$

We repeat the iteration with the updated $[G_{R,j+1}(\omega)]^{-1}$ until it converges and check the constraint $-\int_{-\infty}^{\infty} d\omega \rho(\omega)/(e^{\beta\omega} - 1) - g = -S$. m is varied to satisfy the constraint.

b. Imaginary-time solution

PM phase – We solve the saddle point Eq. 3.3 iteratively to obtain $G(i\omega_k)$ for $k \in [0, k_{max}]$. We start with an initial guess solution which could be the non-interacting part of the Green function and an initial guess value of the Lagrange multiplier λ and calculate $\Sigma(\tau)$ using Eq. 3.3b. We then Fourier transform $G(\tau)$ using fast-Fourier transform (FFT) and obtain $G(i\omega_k)$ and $\Sigma(i\omega_k)$. After j th iteration, $G_i(i\omega_k)$ is updated as,

$$G_{j+1}(i\omega_k) = \frac{1-y}{i\omega_k - \lambda - \Sigma_j(i\omega_k)} + y G_j(i\omega_k) \quad (\text{A.12})$$

After each iteration we monitor the error $e(i\omega_k) = |G_{i+1}(i\omega_k) - G_i(i\omega_k)|$ for each k by comparing with $\epsilon = 10^{-9}$, the tolerance. The procedure is repeated with updated $G_{i+1}(i\omega_k)$ after Fourier transforming back to time domain until $e(i\omega_k) < \epsilon$ for each k . After convergence, we check if the constraint $G(\tau = 0^-) = -S$ is met for the current value of λ . If not we repeat the procedure again after varying λ . The iterations stop only after the constraint is met within a tolerance.

SG phase – In the SG phase we solve for the regular part of the Green function, $\tilde{G}(i\omega_k)$ in Eq. 3.8a using the modified self-energy $\tilde{\Sigma}(\tau)$ in Eq. 3.8b. The procedure to solve the saddle point equation in SG phase is similar to PM phase with the modified constraint, $\tilde{G}(\tau = 0^-) = g - S$.

Starting with an initial ansatz and an initial value of the breaking point, m we calculate the $\tilde{\Sigma}(\tau)$ and g from

Eq. 3.9. We then Fourier transform $\tilde{G}(\tau)$ using FFT and obtain $\tilde{G}(i\omega_k)$ and $\tilde{\Sigma}(i\omega_k)$. At each iteration, $\tilde{G}_i(i\omega_k)$ is updated as

$$\tilde{G}_{j+1}(i\omega_k) = \frac{1-y}{i\omega_k - \tilde{J}g/\Theta - [\tilde{\Sigma}_j(i\omega_k) - \tilde{\Sigma}(i\omega_k = 0)]} + y \tilde{G}_j(i\omega_k) \quad (\text{A.13})$$

The procedure is repeated until convergence and then we check if the constraint is met with current value of m . If not, we vary the value of m , within the range $(0,1]$ and repeat the iteration procedure until the constraint is met.

2. Spectral and correlation function in the SY model

In the SY model, we look at the nature of spectrum as a function of thermal and quantum fluctuations. As summarized in Sec. 3A3, following earlier works^{40,69}, there are three types of solutions of the saddle point equations of Sec. 3A, (1) spin liquid, (2) local moment, and (3) marginal spin glass. These solutions can be distinguished via the bosonic spectral function $\rho(\omega) = -(1/\pi)\text{Im}G_R(\omega)$. In the PM phase, the spin liquid solution resides in the quantum critical region IV, as shown in Fig. 3.1, extending all the way down to $T = 0$ for $S = 0$. For small $S < S_{max} \approx 0.052$, the zero-temperature bosonic Green's function for complex frequency z is given by $G(z) \sim e^{-i(\theta+\pi/4)}/\sqrt{z}$, with $\text{Im}z > 0$ and $\pi/4 < \theta < 3\pi/4$, where the spectral asymmetry θ is related to spin S via $\theta/4 + \sin(2\theta)/4 = 1/2 + S$ ^{38,40}. This leads to a $T = 0$ spectral function, $\rho(\omega) \sim -\text{sgn}(\omega)/\sqrt{|\omega|}$, with characteristic square root divergence at $\omega \rightarrow 0$, and a finite- T conformal spectral function⁸⁸ in region IV of Fig. 3.1,

$$\rho(\omega) \sim \frac{\sinh(\omega/2T)}{\sqrt{T}} \Gamma\left(\frac{1}{4} + i\frac{\omega - \alpha T}{2\pi T}\right) \Gamma\left(\frac{1}{4} - i\frac{\omega - \alpha T}{2\pi T}\right), \quad (\text{A.14})$$

where $\sin(\pi/4 + \theta) = 1/\sqrt{1 + e^{-2\alpha}}$. At finite temperature, the above spectral function, $\rho(\omega) \sim \omega$ for $|\omega| \lesssim T$, has a peak at $|\omega| \sim \mathcal{O}(T)$, and thereafter decays as $1/\sqrt{|\omega|}$ for $\mathcal{O}(T) \lesssim |\omega| \lesssim J$.

The other PM solution, the local moment solution co-exist, and has intricate competition⁴⁰ with the spin liquid solution in the quantum critical region IV (Fig. 3.1). As a result, it is not always easy to distinguish the spin liquid solution and the local moment solution for general (S, T) in the quantum critical region. Ref. 69 has shown the existence of spin liquid solution for small $S < 0.5$ using analytical continuation of the numerical solution of the imaginary-time saddle-point equations [Eqs.(3.3)]. Our results are consistent with that of Ref. 69. This local moment becomes the dominant solution above the

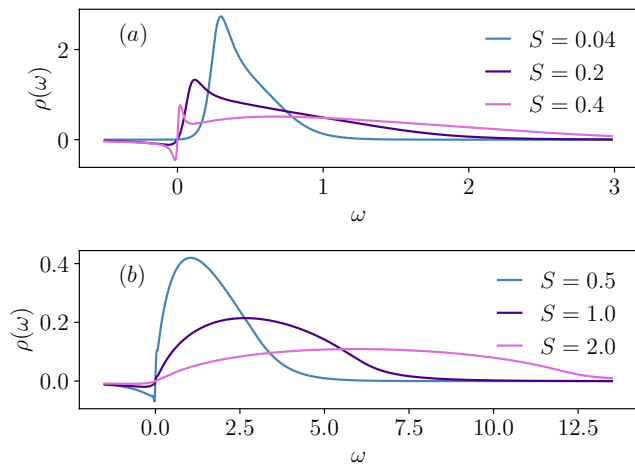


FIG. A.1. Spectral function as a function of S at $T = 0.1$ in (a) PM phase and (b) SG phase.

quantum critical region $T \gtrsim J$, in the PM phase. At high temperature, the local moment solution has a characteristic peak at $\omega \sim \omega_0 \sim T \ln[(S+1)/S]$ ⁴⁰. At very low temperature, below T_{SG} (Fig. 3.1), where the local moment solution is metastable, its spectral function has two peaks at $\sim \pm 1/T$ and a delta function peak with $\rho(\omega) \sim S\omega\delta(\omega)$ ⁴⁰. This low-temperature local moment solution is not relevant for us.

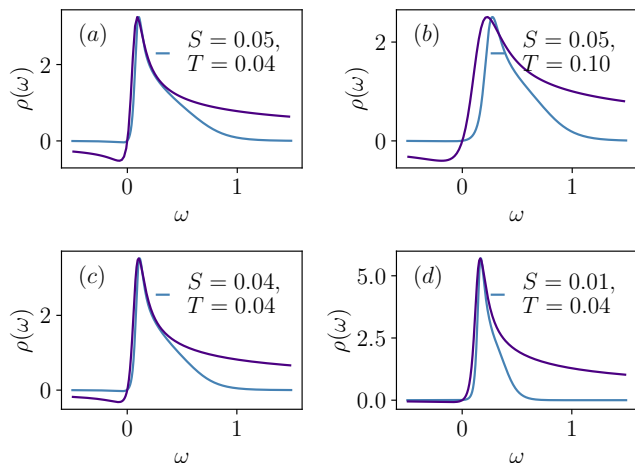


FIG. A.2. Comparison of numerically obtained spectral function (blue) for small $S < S_{max}$ with finite-temperature conformal spectral function (purple) of Eq.(A.14) for the spin liquid. The conformal spectral function is scaled as necessary so that its maximum becomes equal to that of numerical results for the spectral function.

For the marginal spin glass solution, on the other hand, one again obtains a linear-in- ω behavior of the spectral function, termed as pseudogap⁶⁹, where $\rho(\omega) \sim \omega/S$ for

low frequency and low temperature $T \ll T_{SG}$, with a high-frequency broad peak. As T increases towards glass transition, a narrow low-frequency peak around $|\omega| \sim T$ appears on top of the linear- ω pseudogap background. The latter fills up with increasing temperature. The narrow peak around $\sim T$ appears from the loss of spectral weight from the δ -function part in the correlation function, e.g., the Wightmann function of Eq.(4.11), in the SG phase. The $\delta(\omega)$ part in the correlation functions corresponds to static order and its weight is transferred to excitations in the narrow peak of the spectral function $\rho(\omega)$ due to the gradual unfreezing of spins approaching the SG transition. The broad high-frequency peak at $\omega \sim \mathcal{O}(JS)$ originates from precession of frozen spin around their local fields⁶⁹.

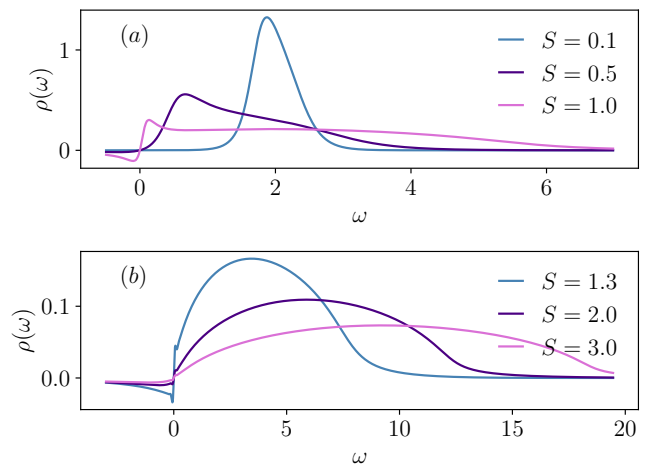


FIG. A.3. Spectral function as a function of S at $T = 0.8$ in (a) PM phase and (b) SG phase.

We have studied the evolution of the spectral function along the fixed- T and fixed- S cuts (Fig. 3.1) employed for our chaos calculations in Secs. 4, 5. We find crossover between the PM solutions and transition from the PM to SG solution. Figs.A.1(a) and (b) show the evolution of $\rho(\omega)$ at low temperature $T = 0.1$ with S (d cut, Fig. 3.1) for the PM and SG phases, respectively. The result for $S = 0.04 < S_{max}$ in Fig.A.1(a) is qualitatively consistent with a spin liquid solution of Eq.(A.14). In Fig.A.2, we make detailed comparison of numerically obtained $\rho(\omega)$ with conformal spectral function of Eq.(A.14) for $S < S_{max}$ at low temperature. The match is reasonable for $T \lesssim 0.05$ at low energies [Fig.A.2(a,c,d)]. However, there are large deviations from the conformal form at high energies. The comparison becomes worse for $S = 0.05, T = 0.1$ [Fig.A.2(b)]. The spectral function $\rho(\omega)$ for $S = 0.2 > S_{max}$ [Fig.A.2(a)] also qualitatively resembles a spin liquid solution, though no analytical form is known in this case. The spectral function acquires low-energy and high-energy peaks, with a dip in spectral weight in between, with further increase of S towards $S_{SG} \simeq 0.48$, as shown in Fig.A.1(a). In the SG

phase [Fig.A.1(b)], $\rho(\omega)$ follows the expected marginal SG behavior discussed above. Qualitatively similar progression of $\rho(\omega)$ with S is seen in Fig.A.3 for the higher $T = 0.8$ (e cut in Fig. 3.1) with $S_{SG} \simeq 1.29$. However, at this higher temperature, $\rho(\omega)$ may be consistent with a local moment like solution with a peak at $\omega_0 \sim T \ln [(S+1)/S]$.

Similarly, for fixed- S cuts a ($S = 0.5$) and b ($S = 1.0$) in Fig. 3.1, the spectral function evolves from that of the SG solutions for $T < T_{SG} \simeq 0.12, 0.49$ in Figs.A.4(a),A.5(a) to the spin liquid or local moment spectral functions in Figs.A.4(b),A.5(b). The narrow peak close to the transition $T \gtrsim T_{SG}$ at $\omega \sim \mathcal{O}(T)$ results from the melting of static order in the SG phase, as discussed earlier.

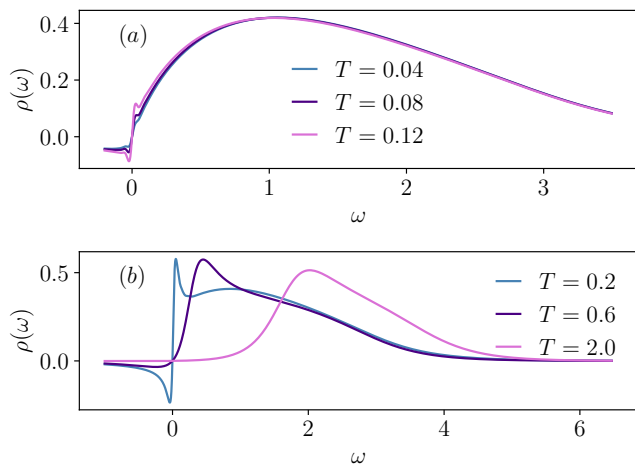


FIG. A.4. Spectral function as a function of T at $S = 0.5$ in (a) SG phase and (b) PM phase.

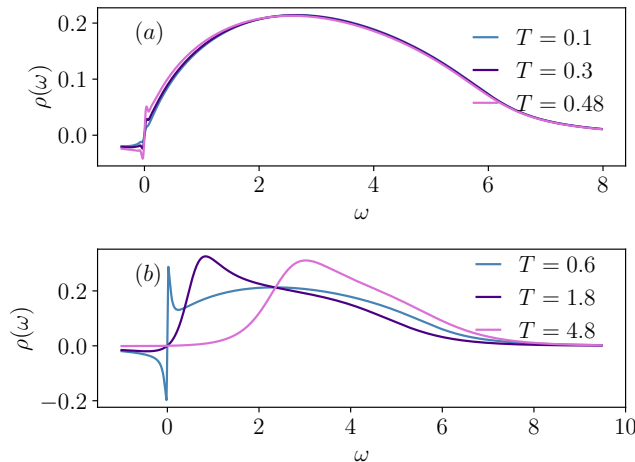


FIG. A.5. Spectral function as a function of T at $S = 1.0$ in (a) SG phase and (b) PM phase.

Spin Susceptibility.— To probe the spin liquid regime for small S further, we compute the local spin susceptibility $\chi(\tau) = \langle S(\tau)S(0) \rangle$. In the large N limit, $\chi(\tau) = G^{aa}(\tau)G^{aa}(-\tau)$. From this, we calculate imaginary part of ω -dependent local spin susceptibility $\chi''(\omega) = (1/\pi)\text{Im}\chi(\omega)$, as

$$\chi''(\omega) = \left[-\frac{\tilde{J}^2}{\pi} \text{Im} \left(i \int_0^\infty dt e^{i\omega t} (n_1(t)n_2(t) - n_3(t)n_4(t)) \right) + g\rho(\omega) - g\rho(-\omega) \right] \quad (\text{A.15})$$

where $n_i(t)$ ($i = 1, 2, 3, 4$) is defined below Eq.(A.7) and g is non-zero only in SG phase. Here $\chi''(\omega)$ satisfies the constraint, $\int d\omega \chi''(\omega)n_B(\omega) = S(S+1)$ in PM phase and $\int d\omega \chi''(\omega)n_B(\omega) = S(S+1) - g^2$ in SG phase. In Figs.A.6 and A.7 we plot $\chi''(\omega)$ across the PM-SG transition at a fixed $T = 0.04$ and at a fixed $S = 0.5$, respectively. We find that these results are in agreement with those (Figures 1 and 2) of Ref. 69 that are obtained using analytical continuation of imaginary solutions of large N saddle point equations using Padé approximation.

Thus, overall, our results for spectral function and local susceptibility, discussed in this section, are consistent with the spin liquid solutions for small S . Nevertheless, as show in Sec. 4, e.g., in Fig. 4.3, the Lyapunov exponent for these spin liquid solutions extrapolates to a value much smaller than maximal $2\pi T$ for $S \rightarrow 0$, unlike in the SYK-type models⁸. This could be due to large non-conformal⁶ T and S dependent corrections to the conformal solution [Eq.(A.14)], seen in Figs.A.2.

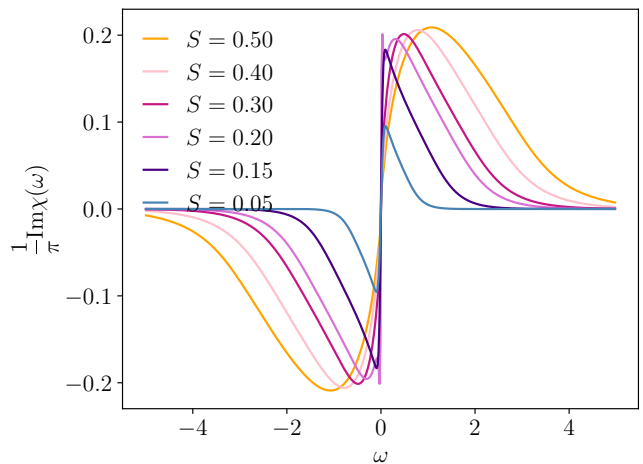


FIG. A.6. Susceptibility $\chi''(\omega)$ across the PM-SG transition at $T = 0.04$. The transition happens at critical value of $S \approx 0.28$.

Wightmann correlation functions— The correlation functions needed in the calculation of chaos can be obtained from the knowledge of the retarded Green's func-

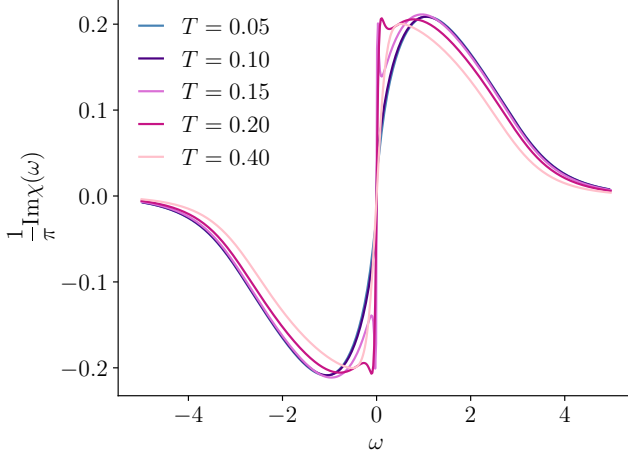


FIG. A.7. Susceptibility $\chi''(\omega)$ across the PM-SG transition at $S = 0.5$. The transition temperature is $T \approx 0.12$

tion or the spectral function discussed above. We calculate $G(\tau)$ using the spectral function from

$$G(\tau) = \begin{cases} \int_{-\infty}^{\infty} d\omega \frac{e^{-\omega\tau} \rho(\omega)}{e^{-\beta\omega} - 1} & (\tau > 0) \\ -\int_{-\infty}^{\infty} d\omega \frac{e^{-\omega\tau} \rho(\omega)}{e^{\beta\omega} - 1} & (\tau < 0) \end{cases} \quad (\text{A.16})$$

Analytically continuing $G(\tau)$ to real time gives Wightmann correlation functions, in the PM phase,

$$G_{lr}^+(t) = -G(it + \beta/2) = \int_{-\infty}^{\infty} \frac{d\omega}{2\pi} e^{-i\omega t} \frac{\pi\rho(\omega)}{\sinh \frac{\beta\omega}{2}} \quad (\text{A.17})$$

$$G_{lr}^-(t) = -G(it - \beta/2) = \int_{-\infty}^{\infty} \frac{d\omega}{2\pi} e^{-i\omega t} \frac{\pi\rho(\omega)}{\sinh \frac{\beta\omega}{2}} \quad (\text{A.18})$$

We notice that $G_{lr}^+(t) = G_{lr}^-(t)$ and hence $G_{lr}^+(\omega) = G_{lr}^-(\omega) = \pi\rho(\omega)/\sinh(\beta\omega/2)$. Similarly, in the SG phase,

$$G_{lr}^{+,ab}(t) = G_{lr}^{-,ab}(t) = g\epsilon_{ab} + \int_{-\infty}^{\infty} \frac{d\omega}{2\pi} e^{-i\omega t} \frac{\pi\rho(\omega)}{\sinh \frac{\beta\omega}{2}} \delta_{ab}, \quad (\text{A.19})$$

that allows to define $G_{lr}^{+,ab}(\omega) = G_{lr}^{-,ab}(\omega) = 2\pi g\delta(\omega)\epsilon_{ab} + \pi\rho(\omega)/(\sinh(\beta\omega/2))\delta_{ab}$. The delta function term proportional to the EA order parameter g at $\omega = 0$ in the Wightmann correlation function indicates the presence of static spin glass order. Similar delta function term appears in the Fourier transform of other correlation functions, e.g., $G_{>}^{aa}(t) = -(i/M)\sum_{\alpha} \langle b_{i\alpha,x}^a \bar{b}_{i\alpha,x}^a \rangle$, and similarly $G_{<}^{aa}(t)$. We note that, since retarded Green's function, $G_R^{aa}(t) = \theta(t)[G_{>}^{aa}(t) - G_{<}^{aa}(t)]$ [$\theta(t)$ is the Heaviside function] and $G_R^{aa}(\omega)$ is obtained by analytically continuing $i\omega_k \rightarrow \omega + i0^+$ in Eq.(3.5), $G_R^{aa}(t)$ is free of any static part even in the SG phase.

Appendix B: Imaginary-time path integral and saddle point equations in p -spin glass chain

As in the case of SY chain [Appendix A], we write the partition function $\mathcal{Z}(\{J_{ijk,x}, J_{ijk,x}^{\pm}\}) = \text{Tr}[\exp(-\beta\mathcal{H})]$ ($\beta = 1/T$) of the disordered model of Eq.(2.3), where $J_{ijk,x}$ and $J_{ijk,x}^{\pm}$ are Gaussian random number with zero mean and variances $3J^2/(2N^2)$ and $3J'^2/2N^2$, as an imaginary-time path integral. We calculate disorder-averaged quantities by introducing replicas $a = 1, \dots, n$, and a Lagrangian multiplier $z(\tau)$ to impose the spherical constraint, to obtain $\overline{\mathcal{Z}^n} = \int \mathcal{D}s \text{exp}[-S_{\text{eff}}]$, where

$$S_{\text{eff}} = \sum_x \left\{ \int_{\tau} \left[\frac{1}{2\Gamma} \left(\frac{\partial s_{i,x}^a}{\partial \tau} \right)^2 + \frac{z^a(\tau)}{2} ((s_{i,x}^a)^2 - N) \right] - \frac{1}{4} \int_{\tau, \tau'} \sum_{ab} \left[\frac{J^2}{N^2} \left(\sum_i s_{i,x}^a(\tau) s_{i,x}^b(\tau') \right)^3 + \frac{J'^2}{N^2} \left(\sum_i s_{i,x}^a(\tau) s_{i,x}^b(\tau') \right) \left(\sum_i s_{i,x+1}^a(\tau) s_{i,x+1}^b(\tau') \right)^2 + \frac{J'^2}{N^2} \left(\sum_i s_{i,x}^a(\tau) s_{i,x}^b(\tau') \right)^2 \left(\sum_i s_{i,x+1}^a(\tau) s_{i,x+1}^b(\tau') \right) \right] \right\} \quad (\text{B.1})$$

Here $\int_{\tau} = \int_0^{\beta} d\tau$. We now introduce the large N field Q and its conjugate Σ , where $Q_x^{ab}(\tau, \tau') = \frac{1}{N} \sum_i \langle s_{i,x}^a(\tau) s_{i,x}^b(\tau') \rangle$, through the identity

$$1 = \int DQ_x^{ab}(\tau, \tau') \delta \left(NQ_x^{ab}(\tau, \tau') - \sum_i s_{i,x}^a(\tau) s_{i,x}^b(\tau') \right) = \int DQ_x^{ab}(\tau, \tau') D\Sigma_x^{ab}(\tau, \tau') \exp \left\{ -\frac{1}{2} \int_{\tau, \tau'} \Sigma_x^{ab}(\tau, \tau') \left(NQ_x^{ab}(\tau, \tau') - \sum_i s_{i,x}^a(\tau) s_{i,x}^b(\tau') \right) \right\} \quad (\text{B.2})$$

Inserting the identity and integrating over $s_{i,x}(\tau)$ in $\overline{\mathcal{Z}^n}$ leads to the effective action

$$S_{\text{eff}} = \sum_x \left\{ \frac{N}{2} \text{Tr} \ln \left[\left(-\frac{1}{\Gamma} \partial_{\tau}^2 + z^a(\tau) \right) \delta(\tau - \tau') \delta_{ab} - \Sigma_x^{ab}(\tau, \tau') \right] - \frac{N}{2} \sum_a \int_{\tau} z^a(\tau) + \frac{N}{2} \sum_{ab} \int_{\tau, \tau'} \left[\Sigma_x^{ab}(\tau, \tau') Q_x^{ab}(\tau, \tau') - \frac{J^2}{4} Q_x^{ab}(\tau, \tau')^3 - \frac{J'^2}{4} \left(Q_x^{ab}(\tau, \tau') Q_{x+1}^{ab}(\tau, \tau')^2 + Q_x^{ab}(\tau, \tau')^2 Q_{x+1}^{ab}(\tau, \tau') \right) \right] \right\} \quad (\text{B.3})$$

In the limit $N \rightarrow \infty$, we can take the saddle point with respect to $\Sigma_x^{ab}(\tau, \tau')$. This gives $\mathbf{Q}_x^{-1} = \mathbf{Q}_0^{-1} - \mathbf{\Sigma}$, where the matrix \mathbf{Q}_0^{-1} is given by $(\mathbf{Q}_0^{-1})^{ab}(\tau, \tau') = \left(-\frac{1}{\Gamma} \partial_{\tau}^2 + \right.$

$z^a(\tau))\delta(\tau - \tau')\delta_{ab}$. Using this we eliminate $\Sigma_x^{ab}(\tau, \tau')$ from the action and obtain effective action in terms of Q ,

$$\begin{aligned} S_{\text{eff}} = & - \sum_x \left\{ \frac{N}{2} \text{Tr} \ln \mathbf{Q}_x - \frac{N}{2} \sum_a \int_\tau z^a(\tau) (Q_x^{aa}(\tau, \tau) - 1) \right. \\ & + N \sum_{a,b} \int_0^\beta d\tau d\tau' \left(\frac{1}{2\Gamma} \partial_\tau^2 Q_x^{ab}(\tau, \tau') \delta(\tau - \tau') \delta_{ab} \right. \\ & + \frac{J^2}{4} Q_x^{ab}(\tau, \tau')^3 + \frac{J'^2}{4} Q_x^{ab}(\tau, \tau') Q_{x+1}^{ab}(\tau, \tau')^2 \\ & \left. \left. + \frac{J'^2}{4} Q_x^{ab}(\tau, \tau')^2 Q_{x+1}^{ab}(\tau, \tau') \right) \right\} \quad (\text{B.4}) \end{aligned}$$

Taking the saddle point with respect to \mathbf{Q} gives the Dyson equation,

$$\begin{aligned} (Q_x^{-1})^{ab}(\tau, \tau') = & \left(-\frac{1}{\Gamma} \partial_\tau^2 + z_a(\tau) \right) \delta(\tau - \tau') \delta_{ab} \\ & - \frac{3J^2}{2} Q_x^{ab}(\tau, \tau')^2 - \frac{J'^2}{2} \left(Q_{x+1}^{ab}(\tau, \tau')^2 + Q_{x-1}^{ab}(\tau, \tau')^2 \right) \\ & - J'^2 Q_x^{ab}(\tau, \tau') \left(Q_{x+1}^{ab}(\tau, \tau') + Q_{x-1}^{ab}(\tau, \tau') \right) \quad (\text{B.5}) \end{aligned}$$

Considering space and time translation invariant solutions for the Dyson equation, of the form $Q_x^{ab}(\tau, \tau') = Q^{ab}(\tau - \tau')$ and $z^a(\tau) = z^a$, the above equation reduces to,

$$(Q^{-1})^{ab}(i\omega_k) = \left(\frac{1}{\Gamma} \omega_k^2 + z^a \right) \delta_{ab} - \Sigma_{ab}(\omega_k) \quad (\text{B.6a})$$

$$\Sigma^{ab}(\tau) = \frac{3\tilde{J}^2}{2} Q^{ab}(\tau)^2 \quad (\text{B.6b})$$

where $\tilde{J}^2 = J^2 + 2J'^2$. The above large N saddle-point equations are the same as that of the zero-dimensional model⁶⁶.

Saddle point equation in PM phase— Using the replica diagonal ansatz and analytically continuing to real frequency, we obtain the saddle-point equation for the retarded Green's function,

$$[Q_R(\omega)]^{-1} = -\frac{1}{\Gamma} \omega^2 + z - \Sigma_R(\omega) \quad (\text{B.7a})$$

$$\Sigma_R(\omega) = \Sigma(i\omega_k \rightarrow \omega + i0^+) \quad (\text{B.7b})$$

Following a procedure similar to that in the case of SY model (Appendix A), the self-energy can be written as,

$$\begin{aligned} \Sigma_R(\omega) = & i \frac{3\tilde{J}^2}{2} \int_0^\infty e^{i\omega t} \left(n_1^2(t) - n_2^2(t) \right), \quad (\text{B.8a}) \\ n_1(t) = & \int d\omega e^{-i\omega t} \rho(\omega) n_B(-\omega), \\ n_2(t) = & \int d\omega e^{-i\omega t} \rho(\omega) n_B(\omega) \end{aligned}$$

where $\rho(\omega) = -(1/\pi) \text{Im} Q_R(\omega)$. The saddle-point equations can be solved numerically, following steps similar to that discussed in the case of SY model.

Saddle point equation in SG phase— Using 1RSB ansatz, after analytical continuation to real frequency $i\omega_k \rightarrow \omega + i0^+$ only the regular part (see Sec. 3B) contributes to the retarded Green's function $Q_R^{ab}(\omega) = Q_R(\omega) \delta_{ab} = \tilde{Q}(i\omega_k \rightarrow \omega + i0^+) \delta_{ab}$ such that

$$[Q_R(\omega)]^{-1} = -\frac{1}{\Gamma} \omega^2 + z - \Sigma_R(\omega), \quad (\text{B.9a})$$

$$\begin{aligned} \Sigma_R(\omega) = & \frac{3J^2}{2} \int_0^\beta d\tau e^{i\omega_k \tau} [\tilde{Q}(\tau)]^2 + 3\tilde{J}^2 q_{\text{EA}} Q_R(\omega) \\ = & i \frac{3\tilde{J}^2}{2} \int_0^\infty e^{i\omega t} \left(n_1^2(t) - n_2^2(t) \right) + 3\tilde{J}^2 q_{\text{EA}} Q_R(\omega), \quad (\text{B.9b}) \end{aligned}$$

where

$$n_1(t) = \int d\omega e^{-i\omega t} \rho(\omega) n_B(-\omega), \quad (\text{B.9c})$$

$$n_2(t) = \int d\omega e^{-i\omega t} \rho(\omega) n_B(\omega) \quad (\text{B.9d})$$

The spherical constraint now takes the form,

$$- \int_{-\infty}^{\infty} d\omega \rho(\omega) n_B(\omega) = 1 - q_{\text{EA}} \quad (\text{B.10})$$

Wightmann correlation functions— The Wightmann functions in the PM phase are given by,

$$Q_{lr}(t) = Q(it + \beta/2) = - \int \frac{d\omega}{2\pi} e^{-i\omega t} \frac{\pi \rho(\omega)}{\sinh \frac{\beta\omega}{2}}, \quad (\text{B.11})$$

and

$$Q_{lr}^{ab}(t) = \epsilon_{ab} q_{\text{EA}} - \delta_{ab} \int \frac{d\omega}{2\pi} e^{-i\omega t} \frac{\pi \rho(\omega)}{\sinh \frac{\beta\omega}{2}} \quad (\text{B.12})$$

in the SG phase.

Appendix C: Calculation of butterfly velocity from the single mode ansatz

Here we briefly discuss the computation of v_B in SY model using the imaginary p method or the single mode ansatz, as described in the main text (Sec. 5A). By calculating $\lambda_L(p)$ for imaginary values of momentum, $p = i|p|$, using the exponential growth ansatz $\mathcal{F}_{\mu,p}(t_1, t_2) = e^{\lambda_L(p)(t_1+t_2)/2} f_{\mu,p}^a(t_1-t_2)$ in Eq. (5.2), we find p_1 and p_s , as discussed in Sec. 5A. At $T = 0.8$ and $S = 0.8$, for example, we have $p_1 \simeq 3.62$ and $p_s \simeq 2.04$, as shown in Fig. C.1. Also, in Fig. C.2, we show that p_s is always less than p_1 , e.g., at $S = 1.0$.

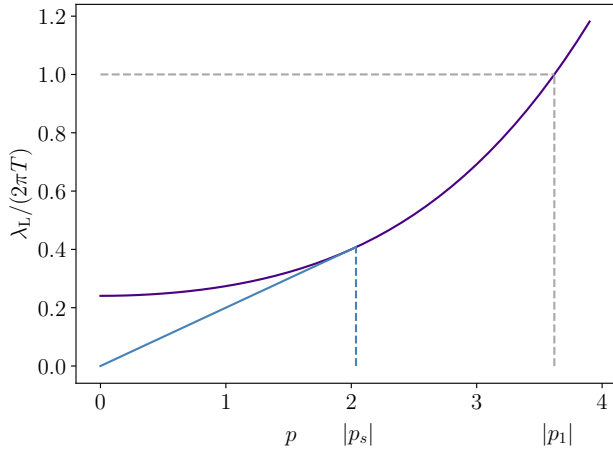


FIG. C.1. $\lambda_L(p = i|p|)$ for $T = 0.8$ and $S = 0.8$ where p_1 and p_s are marked.

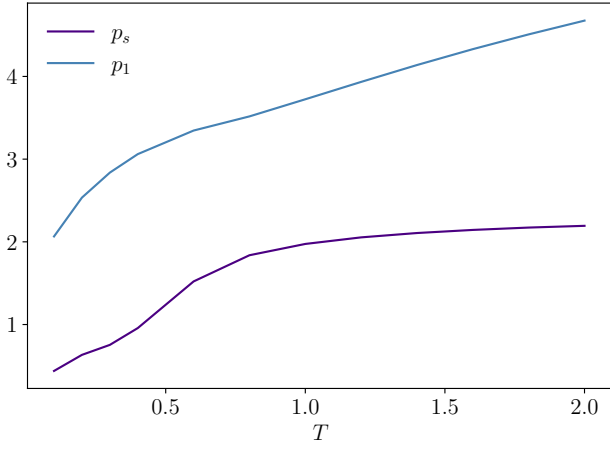


FIG. C.2. p_1, p_s for a range of temperatures at $S = 1.0$